



# Measuring the Thermophysical Properties of Fe-Co alloys using Containerless Electrostatic Levitation Techniques

Submitted By  
Paul Choufani

IN PARTIAL FULFILLMENT OF THE REQUIREMENTS FOR THE DEGREE OF  
**MASTER OF SCIENCE IN MECHANICAL ENGINEERING**

School of Engineering  
Tufts University  
Medford, Massachusetts

August 2012

---

Signature of Author:  
Paul Choufani

---

Certified By:  
Associate Professor Douglas M. Matson  
Department of Mechanical Engineering  
Tufts University

---

Committee:  
Professor Luisa Chiesa  
Department of Mechanical  
Engineering  
Tufts University

---

Committee:  
Dr. Rich Bradshaw  
Ph.D. in Mechanical Engineering  
University of Massachusetts - Amherst

## **Abstract**

Molten FeCo alloys were processed using electrostatic levitation at the NASA Marshall Space Flight Center in order to evaluate thermophysical properties of the melt in support of industrial fluid flow modeling efforts for the casting industry. Digital image analysis of the spherical sample profile is used to track volume as a function of temperature for density measurements. The oscillating drop technique is used for measuring viscosity and surface tension. The goal of this work is to evaluate error associated with conducting measurements during cooling as compared to conducting the measurements at constant temperature. Density measurements were found to be significantly influenced by mass evaporation during the test and a new method of tracking composition changes is proposed. Surface tension measurements were independent of temperature and differences in processing mode with values between 1.70 and 1.79 N/m. In contrast, isothermal viscosities exhibited the expected Arrhenius relationship with temperature while the thermotransient viscosities varied significantly from these values and did not follow anticipated trends.

## Acknowledgements

I would to thank all who supported me during the completion of my work. I am warmly thankful to my research and academic advisors, Professor Matson and Professor Chiesa, who gave me the chance to do my research at Tufts. I would also like to thank Professor Matson for his support, advice, guidance, experience and supervision, without which I could not have done my work. I would also like to express my appreciation for Professor Matson and NASA for the funding offered to do the research project under grants NNX08AL21G and NNX10AV27G. I would also like to thank NASA for the use of the electrostatic levitator at the MSFC Electrostatic Levitation Facility to perform the tests on our samples. I would like to thank Dr. Richard Bradshaw for his priceless efforts in designing the software used for my data analysis, as well as his valuable time in explaining the technical processes of data analysis and clarifying issues which invariably arose during the work itself. I'd also like to thank Paul Sander and Jong Lee for the invaluable help and feedback they have given me for my work, as well as John Work for his software design for temperature filtering. I'd like to extend my thanks to Dr. Jan Rogers, Trudy Allen, and Glen Fountain for their legal and technical support for our work. In addition, many thanks to Professor Matson and the research groups I was involved in during the course of my thesis. I would also like to thank my family and friends for their support during the course of my research.

# Table of Contents

1	Introduction	1
2	Background	6
2.1	A brief history of thermophysical property measurement	6
2.2	Explanation of the containerless processes	8
2.3	Previous experiments and their results	17
3	Methodology	32
3.1	Cases of the thermal profile	34
3.2	Composition Analysis	37
4	Experimental Results	40
5	Discussion	59
5.1	Data analysis and relation to theory	59
5.2	Error analysis	76
6	Conclusions	91
7	Future Work	95
8	References	96
9	Appendices	100

## List of Tables

Table 1: Coefficients of the vapor pressure equation for the given elements	30
Table 2: Values of evaporation coefficients of samples analyzed at Luvak Inc.	40
Table 3: Values of initial and final masses and weight compositions of samples	41
Table 4: Mass and composition information for MAT-376	43
Table 5: Mass and composition information for MAT-378	44
Table 6: Mass and composition information for MAT-391	45
Table 7: Mass and composition information for MAT-392	46
Table 8: Mass and composition information for MAT-393	47
Table 9: Mass and composition information for MAT-396	48
Table 10: Density information for the Fe(45%)-Co(55%) alloy sample	50
Table 11: Density information for the Fe(50%)-Co(50%) alloy sample	55
Table 12: Density information for the Fe(45%)-Co(55%) alloy sample	60
Table 13: Density information for the Fe(50%)-Co(50%) alloy sample	62
Table 14: Watanabe's Fe-Co melting temperature density values and errors	64
Table 15: Our values and error bars for A and Q	74
Table 16: T-test setup to analyze evaporation coefficient-temperature relation	76
Table 17: T-test on evaporation coefficient deviations from linear fit & average	77
Table 18: T-test critical values for confidence probability levels	77
Table 19: Densities of both alloy compositions in liquid state	81
Table 20: Fe(45%)-Co(55%) isothermal viscosities' upper and lower limits	81
Table 21: Average of $(1+(\text{fit deviation}/\text{fit}))$ values in Table 20 & relevant data	82
Table 22: Fe(50%)-Co(50%) isothermal viscosities' upper and lower limits	82
Table 23: Average of $(1+(\text{fit deviation}/\text{fit}))$ values in Table 22 & relevant data	83
Table 24: Isothermal viscosity information for Fe(45%)-Co(55%)	83
Table 25: Thermotransient viscosity information for Fe(45%)-Co(55%)	84
Table 26: Fitted viscosities and t-test information for Fe(45%)-Co(55%)	85
Table 27: Isothermal viscosity information for Fe(50%)-Co(50%)	87
Table 28: Thermotransient viscosity information for Fe(50%)-Co(50%)	87
Table 29: Fitted viscosities and t-test information for Fe(50%)-Co(50%)	89

## List of Figures

Figure 1: Snapshot showing pixel coordinates on sample, edge and background	12
Figure 2: Pixel Intensity vs. Pixel Distance plot through edge detection	13
Figure 3: Figure showing a coarsely detected edge ring	14
Figure 4: Pixel Intensity vs. Pixel Distance plot showing cubic interpolation	15
Figure 5: Viscosity vs. 1/Temperature graph for $Ti_{37}Zr_{42}Ni_{21}$	17
Figure 6: Surface Tension vs. Temperature graph for $Ti_{37}Zr_{42}Ni_{21}$	18
Figure 7: Density vs. Temperature plot for Ni-based superalloy CMSX-4	19
Figure 8: Ln(Viscosity) vs. 1/Temperature plot for CMSX-4	20
Figure 9: Surface Tension vs. Temperature plot for CMSX-4	20
Figure 10: Density vs. Temperature plots for pure Cu and Si-Cu alloy	21
Figure 11: Density vs. Temperature plots for pure Au, Cu and Au-Cu alloy	22
Figure 12: Brillo's Density vs. Temperature plots for Fe-Co alloy	23
Figure 13: Watanabe's Density vs. Temperature plots for Fe-Co alloy	24
Figure 14: Watanabe's Viscosity vs. Temperature plots for Fe-Co alloy	25
Figure 15: Egry and Eichel Fe-Co surface tension-Fe atomic concentration plot	26
Figure 16: Viscosity vs. Temperature plots for Ni-Zr and Ni-Zr <sub>2</sub>	28
Figure 17: Key apparatus of the electrostatic levitator at MSFC, NASA	33
Figure 18: Photo of Electrostatic Levitator at MSFC, NASA	33
Figure 19: Thermal Profile for viscosity tests at 30 °C greater than melt temp	34
Figure 20: Thermal Profile for viscosity tests at 30 °C less than melt temp	35
Figure 21: Thermal Profile for viscosity tests down a temp range of 50 °C	36
Figure 22: Thermal Profile for viscosity tests at melting temperature	37
Figure 23: Viscosity test section of thermal cycle of MAT-376	43
Figure 24: Viscosity test section of thermal cycle of MAT-378	44
Figure 25: Viscosity test section of thermal cycle of MAT-391	45
Figure 26: Viscosity test section of thermal cycle of MAT-392	46
Figure 27: Viscosity test section of thermal cycle of MAT-393	47
Figure 28: Viscosity test section of thermal cycle of MAT-396	48
Figure 29: Density vs. Temperature plot for Fe(45%)-Co(55%) liquid alloy	49
Figure 30: Fe(45%)-Co(55%) isothermal viscosity-temperature plot	50
Figure 31: Fe(45%)-Co(55%) isothermal viscosity-1/temperature plot	51
Figure 32: Fe(45%)-Co(55%) isothermal surface tension-temperature plot	51
Figure 33: Fe(45%)-Co(55%) thermotransient viscosity-temperature plot	52
Figure 34: Fe(45%)-Co(55%) thermotransient viscosity-1/temperature plot	53
Figure 35: Fe(50%)-Co(50%) solid & liquid density-temperature plots	54
Figure 36: Fe(50%)-Co(50%) isothermal viscosity-temperature plot	55
Figure 37: Fe(50%)-Co(50%) isothermal viscosity-1/temperature plot	56
Figure 38: Fe(50%)-Co(50%) isothermal surface tension-temperature plot	57
Figure 39: Fe(50%)-Co(50%) thermotransient viscosity-temperature plot	58
Figure 40: Fe(50%)-Co(50%) thermotransient viscosity-1/temperature plot	58
Figure 41: Density vs. Temperature plot for Fe(45%)-Co(55%) alloy liquid	60
Figure 42: Fe(50%)-Co(50%) solid & liquid density-temperature plots	61

Figure 43: Fe(45%)-Co(55%) isothermal surface tension-temperature plot	66
Figure 44: Fe(50%)-Co(50%) isothermal surface tension-temperature plot	67
Figure 45: Fe(45%)-Co(55%) isothermal & thermotransient visc.-temp plot	70
Figure 46: Fe(50%)-Co(50%) isothermal & thermotransient visc.-temp plot	71
Figure 47: Fe(45%)-Co(55%) isothermal viscosity-temp Arrhenius relation	72
Figure 48: Fe(50%)-Co(50%) isothermal viscosity-temp Arrhenius relation	73
Figure 49: Fe(45%)-Co(55%) $\ln(\text{viscosity})-1/\text{temperature}$ plots	84
Figure 50: Fe(50%)-Co(50%) $\ln(\text{viscosity})-1/\text{temperature}$ plots	88
Figure A.1: Fe(45%)-Co(55%) isothermal viscosity-temperature plot	101
Figure A.2: Fe(45%)-Co(55%) isothermal viscosity-1/temperature plot	101
Figure A.3: Fe(45%)-Co(55%) thermotransient viscosity-temperature plot	102
Figure A.4: Fe(45%)-Co(55%) thermotransient viscosity-1/temperature plot	102
Figure A.5: Fe(50%)-Co(50%) isothermal viscosity-temperature plot	103
Figure A.6: Fe(50%)-Co(50%) isothermal viscosity-1/temperature plot	103
Figure A.7: Fe(50%)-Co(50%) thermotransient viscosity-temperature plot	104
Figure A.8: Fe(50%)-Co(50%) thermotransient viscosity-1/temperature plot	104
Figure B.1: Snapshot showing combined .vol file	106
Figure B.2: Snapshot of sample video file	110
Figure B.3: Snapshot of sample video file being saved as a .histofile	111
Figure B.4: Snapshot of ESL Area Processor in choosing .histofile to process	112
Figure B.5: Snapshot of ESL Set Threshold Levels.vi N-I plot	113
Figure B.6: Snapshot of ESL Area Processor showing the raw Area-Time plot	114
Figure B.7: Snapshot of ESL Area Processor showing Area-Time FFT plot	115
Figure B.8: Snapshot of ESL Area Processor showing filtered Area-Time plot	116
Figure B.9: Snapshot of the entire filtered Area-Time plot undergoing fitting	117
Figure B.10: Snapshot of the section containing the controls and operations	118
Figure B.11: Snapshot of zoomed-in view of filtered Area-Time plot	118
Figure B.12: Snapshot of a poor attempt at an Area-Time plot fit	119
Figure D.1: Snapshot of highly zoomed-in view of filtered Area-Time plot	124
Figure D.2: Snapshot of the vertical deviation of the sample	125
Figure D.3: Snapshot of the horizontal deviation of sample	126
Figure E.1: Diagram showing the density tests on the cooling sample	127
Figure E.2: Diagram showing the isothermal viscosity tests on the sample	128
Figure E.3: Diagram showing the thermotransient viscosity test on the sample	129

# Introduction

The study of thermophysical properties can be difficult with conventional processing methods, due to the risk of contamination [2]. Hence, we use containerless processing, by means of electrostatic levitation, which allows us to study metastable undercooled phases, since it delays solidification by reducing nucleation sites [10]. Combining newly-developed optical-based methods (through the use of optical pyrometers and a high-speed camera based system) to measure properties such as surface tension, viscosity and density with the electrostatic levitator located at Marshall Space Flight Center allows several containerless material studies to be performed for microgravity-affiliated projects. The tests in the levitator are performed in high vacuum [1] – an environment that prevents highly reactive alloys from oxidizing.

At the moment, studies of specific alloys at elevated temperatures are being undertaken to support flight experiments at the International Space Station. Our experimental work is also significant from an industrial and material science perspective. Based on the Materials Genome Initiative for Global Competitiveness (MGI), a materials-research program announced by the US government in June 2011, the experimental work focuses on some strategically important alloys. The MGI is geared towards making the US more competitive globally while dealing with challenges pertaining to national and economic security, clean energy and human welfare. The aim of the MGI is to increase the



speed and decrease the cost of developing and manufacturing technologically advanced materials and further the understanding of the arrangement and performance of a wide array of materials in the US. Such high-tech materials will be used to enhance American manufacturing and boost domestic materials-based industries. For instance, they can be used in making vehicles lighter as well as producing packaging that maintains food's freshness and nutrition level. Of the specific alloys being studied and characterized, Fe-Co is examined because its cobalt proportion induces desirable material properties in manufactured products. However, due to cobalt's relatively high cost with respect to iron, and the dependency on its supply abroad because of the dearth of Co resources in the US, it would be desirable to reduce the Co percentage used in industry through understanding the solidification process to be able to model and control it. In doing so, we aim to alter the solidification process of Fe-Co alloys with relatively low cobalt composition, e.g. Fe(70%)-Co(30%), so that we obtain more adequate material properties nearer to those exhibited by Fe-Co alloys with higher cobalt composition, such as Fe(50%)-Co(50%) and Fe(45%)-Co(55%) (alloys we are studying).

Experimental results and patterns from previous experiments will be used to compare the results for the Fe(50%)-Co(50%) and Fe(45%)-Co(55%) alloy samples whose thermophysical properties are to be analyzed after collecting the necessary data at MSFC. More importantly, the objective is to obtain ground-based ESL measurements of data of undercooled, superheated and melting temperature melts in order determine the thermophysical properties of density,

viscosity and surface tension to establish a reference for future microgravity measurements (through containerless processing) of thermophysical properties which will be performed in space by NASA, at the International Space Station (ISS). The aforementioned material properties are under study for applications in industry and material science. Undercooled and melting temperatures and superheated data of high-temperature melts are used to research fundamental behaviours of fluids; the nature of the fluid flow allows us to determine the effect of convection on the liquid alloys, and hence establish a technically important understanding of the solidification phases and transformation from the metastable (body-centered cubic) to the stable (face-centered cubic) phases. The flow within liquid metal droplets (due to convection) during the formation of dendrites could either be laminar or turbulent, and we use the Reynolds number ( $Re = \text{density} \times \text{velocity} \times \text{characteristic length} / \text{viscosity}$ ) to determine its nature (based on our calculations of density and viscosity).

Containerless processing itself is significant in the studies of fluid flow dynamics, glass formation, undercooling, pure substance preparation and solidification. Studies of thermophysical properties' variation with temperature were performed on earth based on data collected on different alloys, and the expectation is that tests which would be performed on our alloy compositions of study, namely Fe(50%)-Co(50%) and Fe(45%)-Co(55%), would yield similar trends for the thermophysical property data, in order to serve as a platform for future tests for thermophysical property data to be run in microgravity. Our motivation for performing the experiments at MSFC lies in whether we can obtain reasonable

values for viscosity without applying a thermal hold, since doing so at the International Space Station will result in substantial composition changes in the alloy samples and as well as damages to the facility in space. Therefore, we hope to be able to conclude that running experiments based on thermo-transient viscosity testing will suffice in our quest to obtain the viscosity values for our Fe-Co samples in space, as opposed to having to rely on isothermal viscosity testing, where a thermal hold on the sample is required. There is no thermal hold involved in the thermo-transient viscosity testing, since the deformation which is triggered in the superheated sample (to obtain the viscosity) occurs down a temperature gradient. Therefore, the elemental composition changes in the sample will be less than in the case of the thermal hold being present in the isothermal viscosity tests, and there will be no damages to the testing facility at the ISS due to this (thermo-transient) form of testing. If, however, the viscosity values obtained through thermo-transient testing at MSFC are not within a reasonable range specified by the viscosity values obtained through isothermal testing there, then we would conclude that we need to perform both forms of testing at the ISS, which is inconvenient for the reasons mentioned, yet necessary.

On the other hand, not only does containerless processing under vacuum conditions avoid the impurities in a gas atmosphere, but the vacuum itself will cause evaporation of the surface layers of the sample, therefore leading to purification of the sample surface. Additionally, the vacuum simplifies thermal calculations since radiation is the only means of heat transfer, notwithstanding a slight level of convection caused by heating one side of the sample with the laser,

thus causing that sample part to be hotter than another part of it, in the presence of few air molecules around the sample itself. Due to the evaporation of the surface layers of the sample, we have a reduction in mass as well as a change in the atomic composition of each of the iron and cobalt components in the Fe-Co alloy sample. This evaporation occurs mainly at high temperatures, especially in the superheated, melting temperature and undercooled phases during the sample's thermal cycle.

# Background

## **A brief history of thermophysical property measurement**

Means of measuring thermophysical properties have changed and evolved over time. It was always of major interest to study the thermophysical properties of surface tension, density and viscosity of undercooled or superheated materials in order to understand their uses in material science and industry. Currently, studies on liquid alloys at high temperatures are in process to support flight experiments at NASA.

It was only in recent decades that the measurement of thermophysical properties through the use of containerless processing began. Before then, the traditional methods which prevailed in measuring these properties were contact processes. In the case of surface tension, methods such as the sessile-drop method and the maximum bubble pressure method were used. The capillary method and the oscillating plate rheometer were used to measure viscosity [10, 18].

Traditional methods to measure the surface tension include the sessile-drop method. Here, the surface tension measured is personified by the tension force due to intermolecular forces between the solid surface and probe liquid. The drop of liquid does not wet the surface; the depth and mass of the drop are measured. Hence, the shape of the drop is determined and the surface tension can be estimated. The maximum bubble pressure method is another means to measure the surface tension. Here, a bubble pressure tensiometer produces gas bubbles

being blown through capillary tubes which are submerged in a liquid. The radius of the capillary is known, and it is equal to the final (minimum) radius of the bubble as it reaches its hemispherical shape with a pressure increasing to a maximum.

The surface tension of the bubble can be found from the following equation:

$$\sigma = \frac{\Delta P_{\max} \times R_{\text{cap}}}{2},$$

where  $\sigma$  is the surface tension,  $\Delta P_{\max}$  is the maximum pressure drop from the hemispherical mode of the bubble to its complete release from the capillary tube, and  $R_{\text{cap}}$  is the radius of the capillary.

Conventional methods of measuring viscosity include the capillary method, where the viscometer measures the viscosity of a liquid with known density. The flow rate of the liquid flowing through the capillary tube is measured, as well as the pressure difference between both ends of the capillary tube itself. The oscillating plate rheometer is another means of measuring viscosity. The rheometer has two parallel plates, one which is fixed and another which oscillates at predetermined speeds. The plates are heated to enable viscosity measurement at a particular temperature, while the rheometer itself measures torque.

These aforementioned techniques are proper for non-reactive liquids; they cannot be used for potentially-reactive high temperature materials. If they are, then the surface tension data obtained for these materials will be over a wide range due to

differing surface conditions as a result of chemical reactions that can take place.

Hence, we turn our attention to other techniques.

### **Explanation of the containerless processes**

Levitation techniques, which include electrostatic, electromagnetic, acoustic and aerodynamic levitation have the advantage over these techniques in the sense that they are used for containerless processing, and hence does not adversely affect the sample under study through contamination [10, 12].

The first containerless measurements for density were performed by R. G. Ward and his co-workers in the 1960s. They used electromagnetic levitation to perform these measurements; it involved the use of an optical prism and a levitation coil and tube, and employed high-speed photographic observation in order to determine the radius (and hence volume) of the spherical drop. Since the mass can be weighed before and after the levitation process, the density can be determined by dividing the mass by the drop volume [2, 33].

For our experiment, we will use the electrostatic levitation technique to measure the properties of density, viscosity and surface tension for our Fe-Co alloy melts.

Electrostatic levitation involves levitation of the sample through Coulomb (electrostatic) forces generated by charged electrodes; the forces themselves must be generated in an upward direction in order to balance the sample's weight. The coulomb forces which support the electrically charged sample (at a specific voltage application) are due to the electrostatic field generated by the charges

triggered in the electrostatic levitator. The sample's position is made to be stable through a feedback control system which uses a charged couple device (CCD) camera to collect the sample's image and relay the sample's position and velocity data to a microcomputer, which in turn controls the sample's position through electrostatic forces produced by the charged electrodes. In order to heat and melt the levitated sample inside the high-vacuum chamber, a laser (whose intensity we can control) is used [33].

In measuring surface tension and viscosity, the oscillating drop method is used as a containerless process [7, 8, 9, 10, 19]. The idea here is that liquid droplets undergo oscillations about their equilibrium shape; the surface tension can be found through the oscillating frequency and the viscosity can be determined through the damping time constant [7, 8, 9, 10].

The oscillating drop technique involves liquid samples performing oscillations about the equilibrium shape, which is spherical. The surface tension can be evaluated from the natural frequency of the droplet's surface oscillations. Digital image processing is used to analyze the frequency spectrum of the oscillations; a high-speed camera collects consecutive sample images of varying profile area and provides the oscillation frequencies. Image analysis of the oscillations results in an area signal vs. time graph. Fourier transformation (software) analysis on the area signal, reflecting the radius of the sample droplet, removes the sample's low-frequency oscillations and determines the natural frequency of the sample's oscillations. The signal then undergoes filtering in order to obtain the damped



oscillations. The damping time constant is then obtained by fitting a damped sine wave to the signal, and therefore the viscosity can be determined [1, 4, 10].

The mathematical form of the damped sine wave is as follows [10]:

$$x(t) = c \cos(\omega t + \phi) \exp\left(-\frac{t}{\tau}\right),$$

where  $\omega$  is the natural frequency,  $t$  is the time,  $\phi$  is the offset angle and  $\tau$  is the damping time constant [10].

The damping time constant is given by the following formula [1, 3, 4, 10, 21]:

$$\tau_l = \frac{\rho R_0^2}{(l-1)(2l+1)\mu},$$

from which the viscosity can be obtained:

$$\mu = \frac{\rho R_0^2}{(l-1)(2l+1)\tau_l},$$

where  $\rho$  is the density,  $R_0$  is the radius of the undeformed sphere,  $l$  is the mode of oscillations (equal to 2) and  $\mu$  is the viscosity [21, 22].

The natural frequency of surface oscillations of the spherical liquid droplet is given by the following formula, Rayleigh's equation [1, 3, 4, 10, 21]:

$$f_l = \sqrt{\frac{l(l-1)(l+2)\gamma}{3\pi m}},$$

from which the surface tension can be obtained:

$$\gamma = \frac{3\pi m f_l^2}{l(l-1)(l+2)},$$

where  $m$  is the droplet mass,  $l$  is the mode of oscillations (equal to 2) and  $\gamma$  is the surface tension [4].

As for the density measurement of the melted sample, we use digitally processed images which relay the melted sample's cross-section from 2D profiles in order to measure volume [4]. Dividing the measured mass of the sample by the volume will yield the density.

The image analysis involves three steps:

- 1- Edge detection of a sample profile
- 2- Polynomial fitting to the detected edge points
- 3- Integrating the polynomial describing edge points

During edge detection, the edge seen by the eye is translated into a varying profile of pixel intensities. Pixel intensity values in the liquid sample image shown below range from 0 (black) to 255 (white). The sample image itself is a 512 x 512 pixel image. Using the MiDAS Player software to open the video file (Figure 1), we

have the ability to use the coordinate pixel values to numerically identify the sample, background and edge regions at a certain frame:

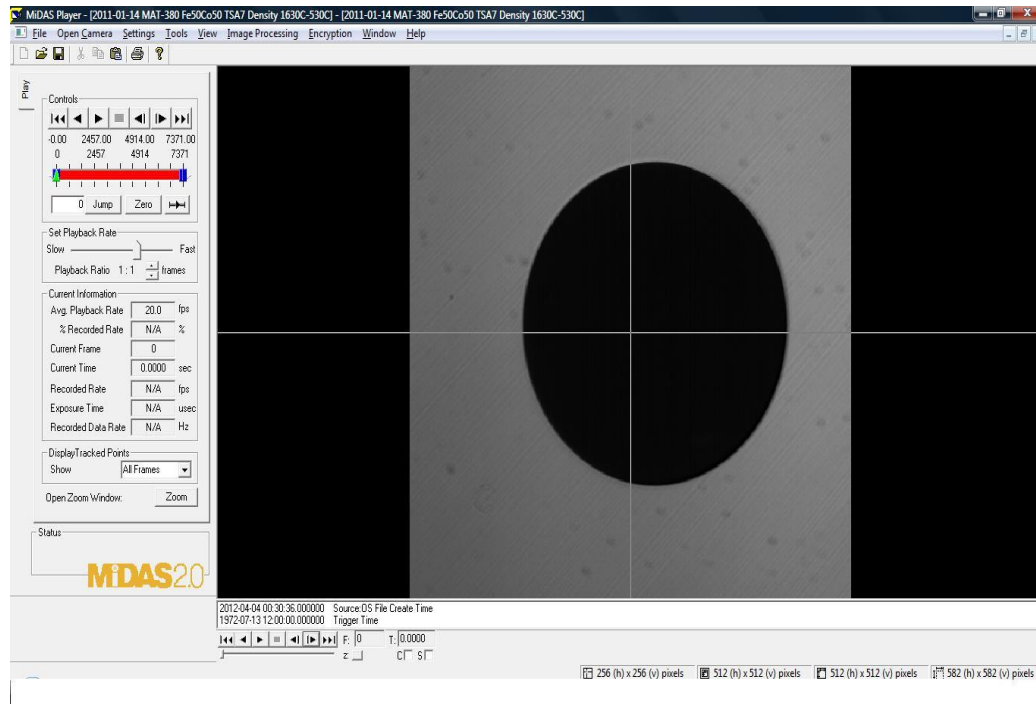


**Figure 1: Screen-shot of a video file of the sample during a density test as seen through the MiDAS Player software which displays the pixel coordinates on the sample, edge and background.**

From the diagram shown, a graph of Pixel Intensity vs. Pixel (horizontal)

Distance is produced, as shown in Figure 2:

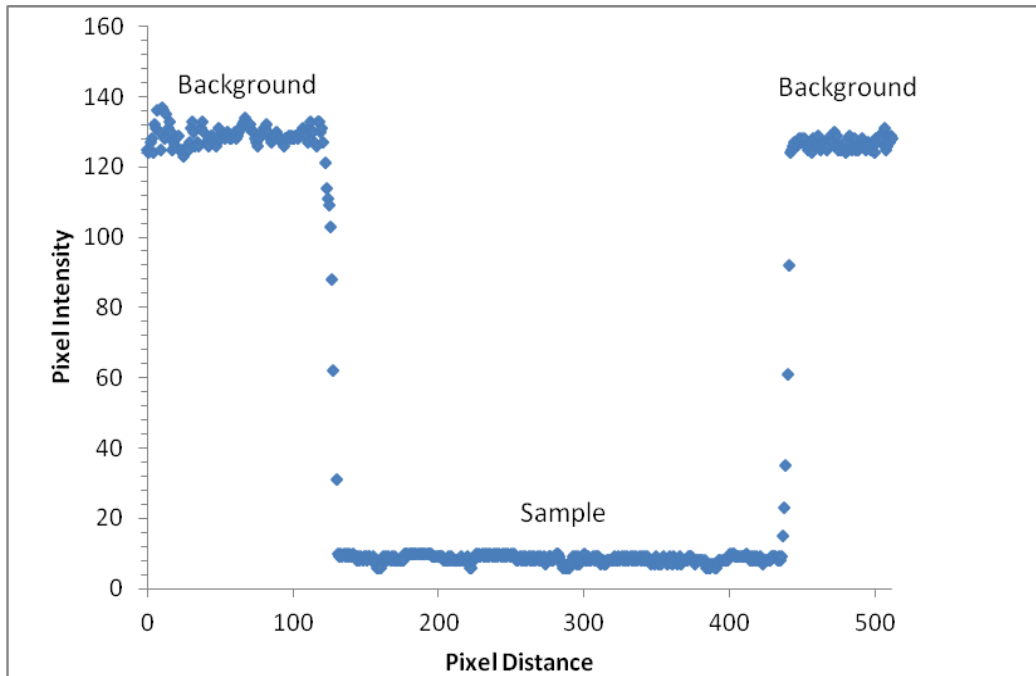


**Figure 2: Plot showing the graph of Pixel Intensity vs Pixel (horizontal) Distance generated through edge detection.**

- As can be observed from the graph, the lighter background of the image has a representation of pixel intensities between 120 and 140, while the dark profile itself is symbolized by pixel intensities between 0 and 10 in value. The two vertical series of values, on either side of the sample regions, are both used to carry out sub-pixel edge detection, which is critical for measuring density. There are two steps for edge detection: coarse edge detection and sub-pixel detection [2].
- In coarse edge detection, the program looks for the edge of the sample in each row of the image. For each image, individual values are concluded on each sample edge.

- A 21x21-pixel square section encapsulates each edge point. A ring including edge transition pixels for the entire sample is formed. In this ring, sub-pixel edge detection is performed [2].
- Figure 3 shows a coarsely detected edge ring:

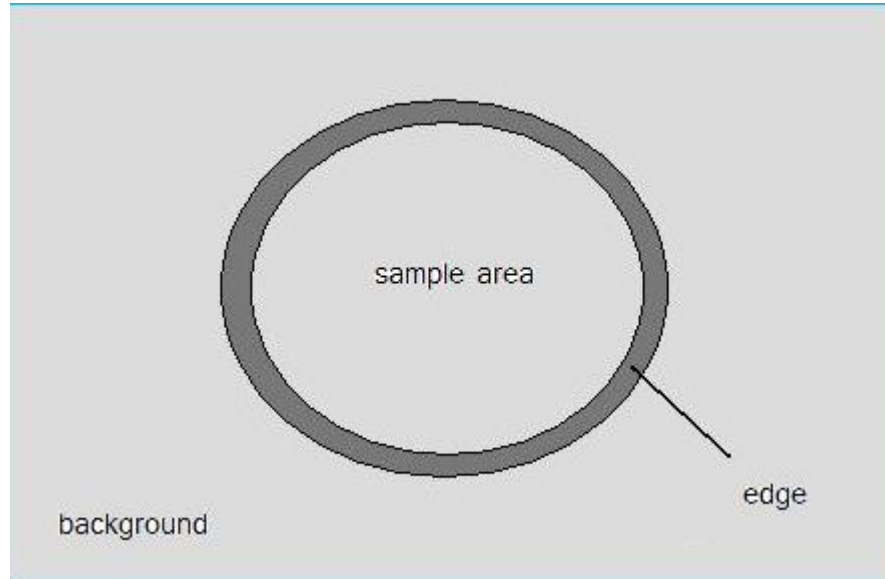


**Figure 3: Coarsely detected edge ring representing the edge transition region (in which sub-pixel edge detection is performed) which separates the background and sample area.**

- Sub-pixel detection, on the other hand, is performed in the edge transition region, through seeking out pixel intensity values along radial vectors emanating from the sample's centroid [2].
- Several hundred different search directions are used, and they depend on the size of the sample under study.

- The edge transition region undergoes cubic interpolation through the edge transition pixels along each search direction [2]. The cubic polynomial fit interpolates the edge transition region, as shown in Figure 4:

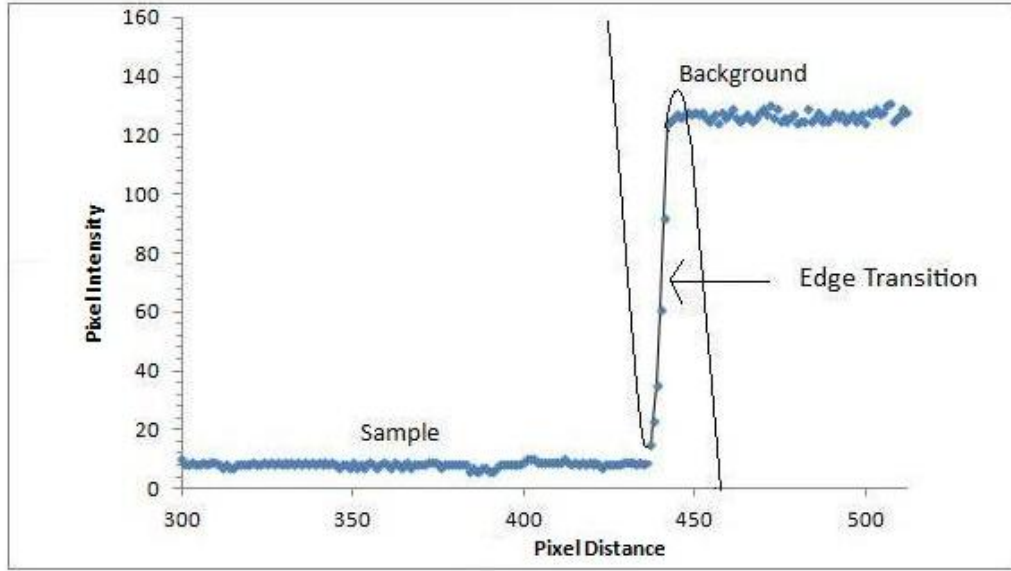


**Figure 4: Plot showing the graph of Pixel Intensity vs Pixel Horizontal Distance where the edge transition region undergoes interpolation through a cubic polynomial fit example represented by the black curve.**

- On each search direction, the polynomial is solved for a radial location from the centroid of the image, at a position halfway between the sample and background pixel values.

During levitation on earth, samples are not exactly spherical due to effects of gravity and the electromagnetic field. There is sphere deformation; hence a representative Legendre polynomial is used to fit the radius (distance of the centre of mass of the droplet to the average edge of the droplet). The polynomial is being fitted to the edge transition region, from which we get the following [2, 4, 10]:

$$R(\theta) = \sum_{i=0}^6 a_i P_i(\cos(\theta))$$

The location of the edge itself is determined through interpolation of the (pixel) intensity values at specific locations on the sample's perimeter.

Using rotational symmetry, the volume can be obtained through the following [2, 4, 10]:

$$Volume = \frac{2}{3} \pi \int_0^{\pi} R(\theta)^3 \sin(\theta) d\theta$$

where  $a(i)$  is the  $i^{\text{th}}$  coefficient and  $R$  is the radius of the sample shape as a function of the angle of rotation  $\theta$  ( $\Theta$ ).

- The volume is obtained in cubic pixels, and should be converted to real volume through a calibration factor. This factor is obtained through measuring the volume of a calibration sphere of known volume.
- A density measurement can be derived from each video image/frame, and each measurement can be associated with a temperature; thus enabling density-temperature plots.

Volume integration for each image is done automatically by the program to avert errors in computations if the sample is vibrating during levitation.

We divide the sample mass by volume to obtain density:  $\rho = \frac{m}{V}$

## Previous experiments and their results

Previous experiments were done on different alloys, and we obtained consistent results for the thermophysical properties upon testing the alloy samples. The aim is to obtain results consistent with those in previous endeavours.

The alloy Ti-Zr-Ni underwent electrostatic levitation, and its surface tension and viscosity were measured by Hyers et al. in 2004 [1]. The following graphs (Figures 5, 6) were obtained for each of the aforementioned properties:

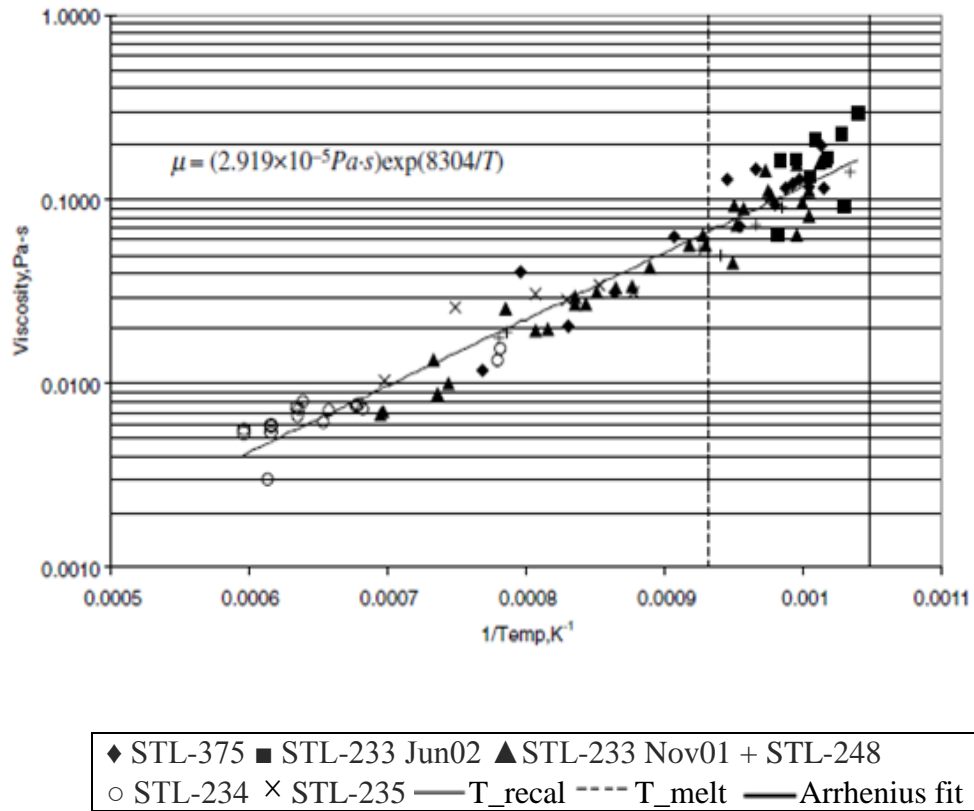


**Figure 5: Graph showing an Arrhenius fit for the plot of Viscosity vs. 1/Temperature for the different samples of the alloy  $Ti_{37}Zr_{42}Ni_{21}$  [10].**



The graph above (Figure 5) depicts an Arrhenius fit for the viscosity, plotted versus  $1/\text{temperature}$  [13]. The alloy under study is  $Ti_{37}Zr_{42}Ni_{21}$ . The graph below (Figure 6) depicts the graph of surface tension versus temperature for the same alloy [1]. We see that in the temperature range after the melting temperature, surface tension seems to be decreasing linearly very slightly with temperature – it takes an almost horizontal shape after the melting temperature, which is approximately 1070 K.

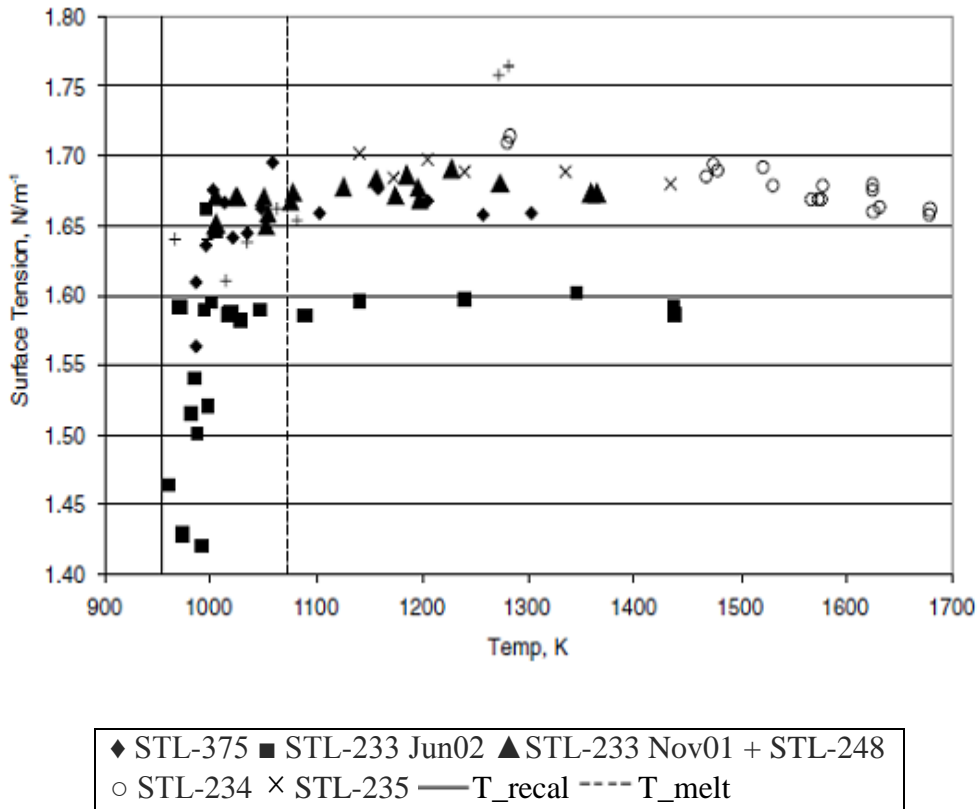


**Figure 6: Graph showing the plot of Surface Tension vs. Temperature for the different samples of the alloy  $Ti_{37}Zr_{42}Ni_{21}$  [10].**

Further studies of alloys include viscosity, surface tension and density measurements on the commercial Ni-based superalloy CMSX-4, using a laser

flash technique. The work was performed as part of the European Space Agency project [16].

The following graph (Figure 7) depicts density versus temperature, as generated by Matsushita et al. in 2009 [16]. The relationship is linear - density decreases linearly with temperature:

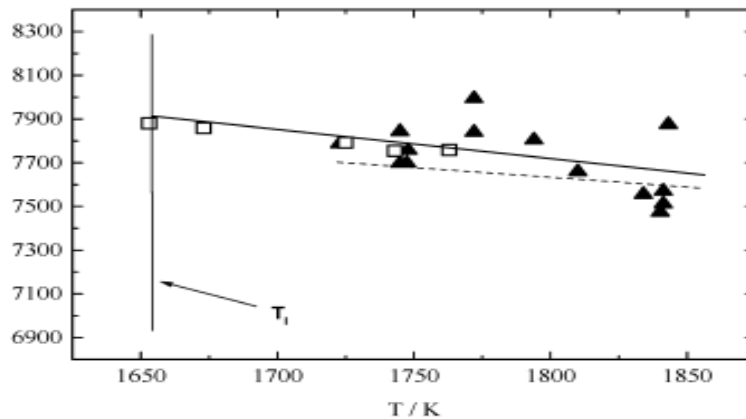


**Figure 7: Graph showing the linearly decreasing plot of Density vs. Temperature for the Ni-based superalloy CMSX-4.**

The triangles represent the density values measured through electromagnetic levitation. The squares represent the density values measured through the sessile drop method [16].

Beforehand, in 2007, the following graph (Figure 8) which depicts viscosity versus  $1/\text{temperature}$  [5, 16], was obtained by Higuchi et al. The relationship between the viscosity and temperature is of an Arrhenius nature [13]. The specimen is of low-oxygen content.

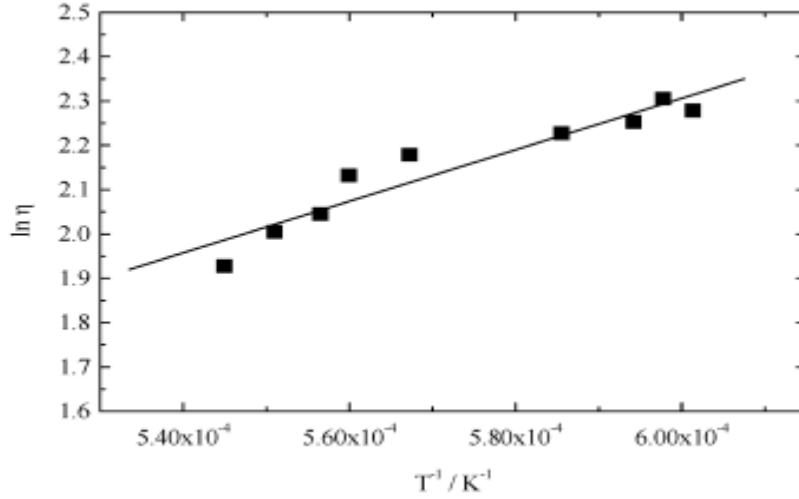


**Figure 8: Graph illustrating the Arrhenius relationship of the viscosity with temperature, showing the positive-slope, oblique line plot of the natural logarithm of the Viscosity vs. 1/Temperature for the Ni-based superalloy CMSX-4.**

The following graph (Figure 9) reflects on the relationship between the surface tension and the temperature, also generated by Higuchi et al. in 2007 [5, 16]. We can deduce that the surface tension decreases linearly with temperature.

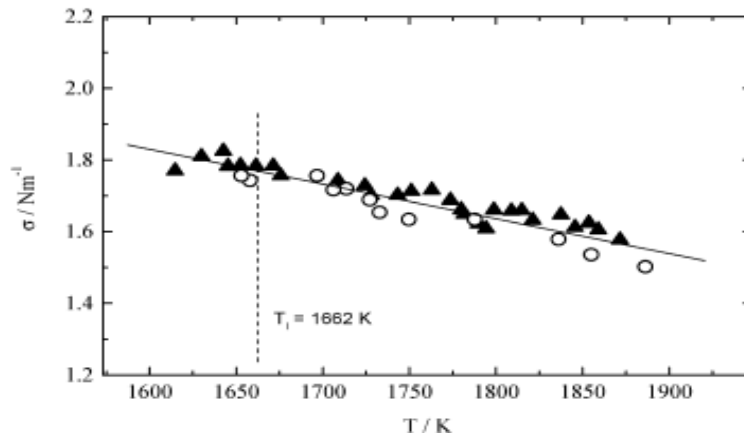


**Figure 9: Graph showing the linearly decreasing plot of Surface Tension vs. Temperature for the Ni-based superalloy CMSX-4.**

The hollow circles represent the surface tension values of the specimen at the first processing attempt, while the solid triangles represent the corresponding values of the specimen at the second processing attempt [5].

In addition, density measurement was performed on the liquid Si-Cu binary alloy, as the different concentrations of silicon and copper within the binary system were subjected to electromagnetic levitation, thus resulting in the following graphical relationship between the different Si-Cu concentrations and temperature, as Adachi et al. came up with in 2010 [6]:

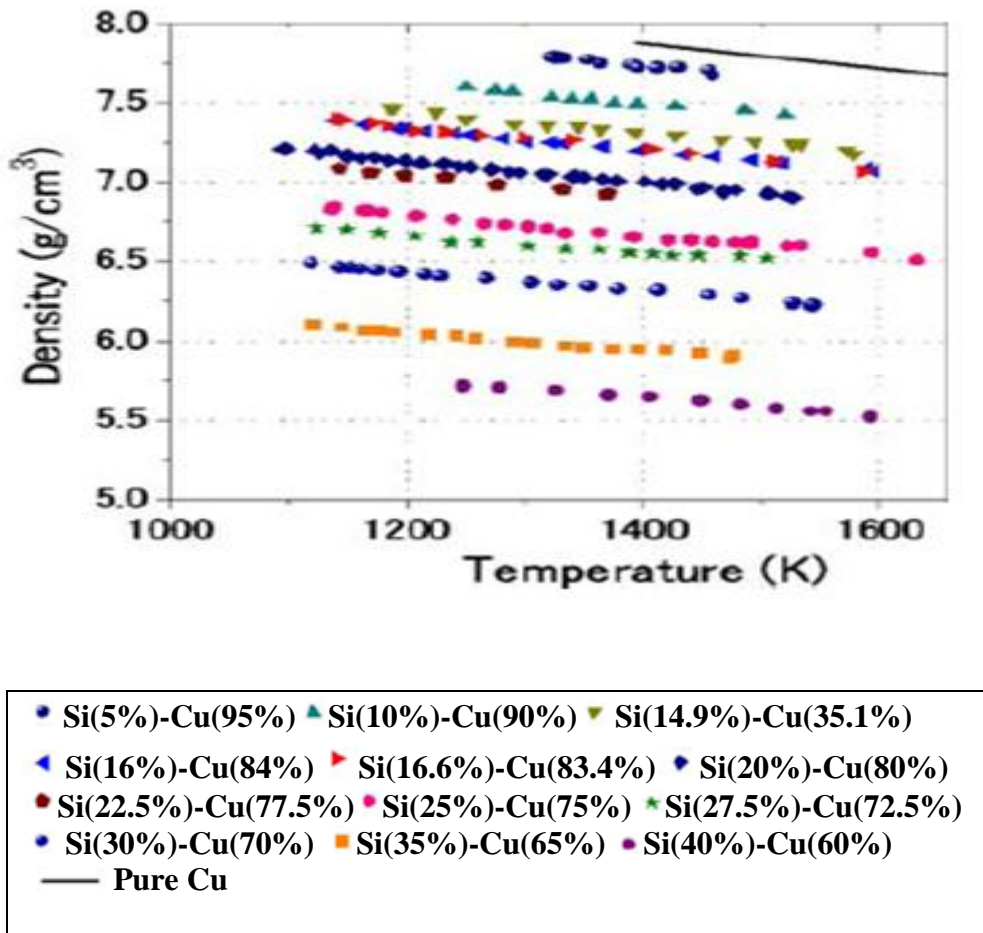


**Figure 10: Graph showing the linearly decreasing plot of Density vs. Temperature for pure Cu and the different elemental compositions of the alloy Si-Cu.**

As we can see in Figure 10, the general relationship for the density of the Si-Cu alloy is that it decreases linearly with increasing temperature. The density-temperature plot for pure copper, as shown in Figure 10, was obtained from Brillo et al. in 2003 [23].

Similar trends for the density data were established by Brillo et al. for different elemental compositions of the alloy Au-Cu in 2004, as shown in Figure 11 (density of the liquid Au-Cu alloy samples were measured through electromagnetic levitation) [24]:

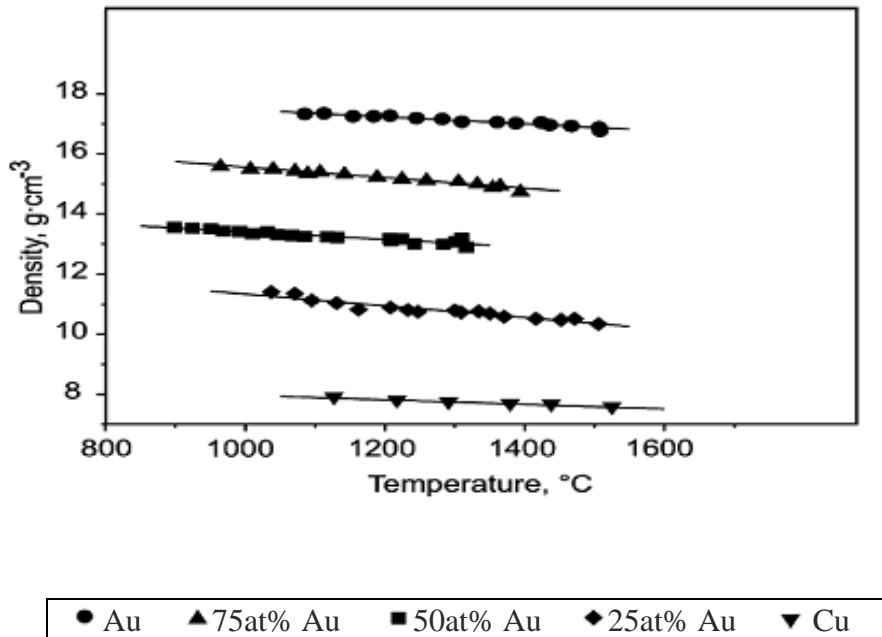
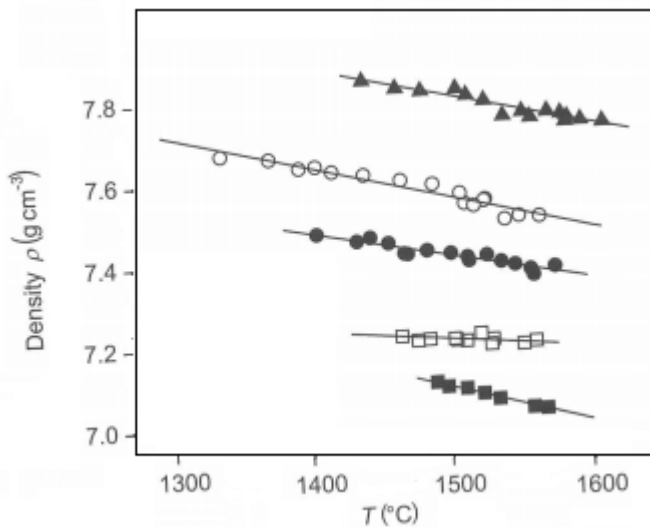


**Figure 11: Graph showing the linearly decreasing plots of Density vs. Temperature for different elemental compositions of the liquid Au-Cu alloy.**

J. Brillo et al. (2006) derived the negative linear relationship for the density of liquid Fe(50%)-Co(50%) with temperature, shown in Figure 12 [36]. Brillo used a non-contact technique as a method to measure density of a Fe-Co liquid sample at a high temperature, comprising electromagnetic levitation and optical dilatometry. In an EML chamber, the sample undergoes positioning and melting through induction between the sample itself and the alternating electromagnetic field of the coil around the chamber. A laser beam lights up the sample, whose image is captured by a digital CCD camera and analyzed through edge detection, resulting in the location of the edge curve which is averaged over 1000 frames and then fitted by Legendre polynomials. The edge curve is then integrated to obtain the volume; knowing the mass, density can be determined. Laminar flow of the Helium-Hydrogen gas mixture inside the chamber is used to cool the sample [36].



■ Fe    ○ Fe(25%)-Co(75%)    ● Fe(50%)-Co(50%)  
□ Fe(75%)-Co(25%)    ▲ Co

**Figure 12: Graph showing Brillo's linearly decreasing plots of Density vs. Temperature for different elemental compositions of the liquid Fe-Co alloy.**

Shunroku Watanabe (1971) obtained the density graphs, shown in Figure 13, for Fe(40%)-Co(60%) and Fe(60%)-Co(40%), having performed density measurements on the alloy samples using the maximum bubble pressure method. The liquid density is measured through a pressure difference of a gas (blown through a tube inserted in the liquid sample) between two levels [17].

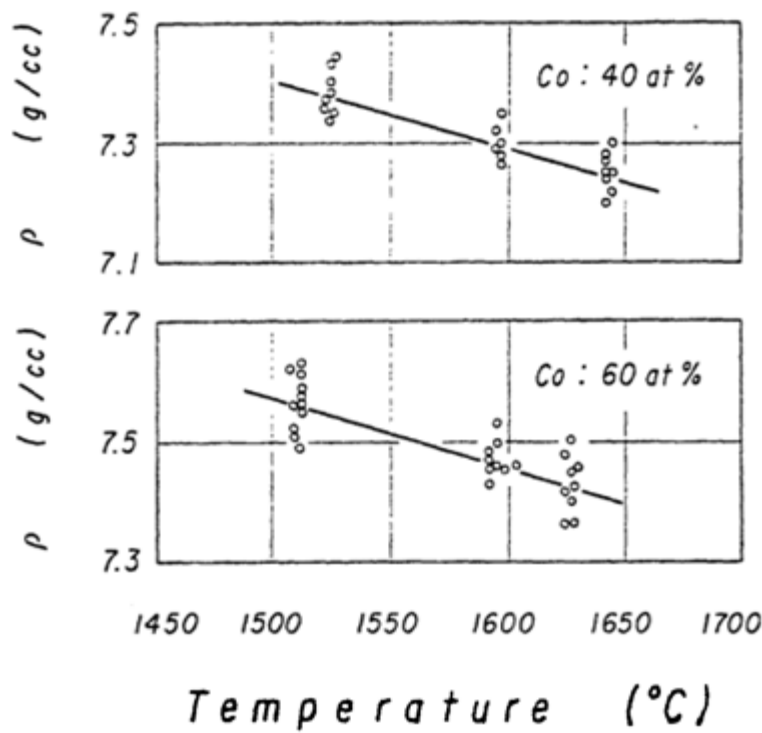


**Figure 13: Graphs showing Watanabe's linearly decreasing plots of Density vs. Temperature for Fe(60%)-Co(40%) and Fe(40%)-Co(60%).**

Watanabe also obtained the following viscosity-temperature graphical relations (Figure 14) for different compositions of the Fe-Co alloy. The viscosity measurements were taken using the oscillating crucible method. The viscosity is derived by its relationship with the liquid's number of oscillations and amplitude, the liquid sample (undergoing an electromagnetically-initiated rotational oscillation about its axis) being inside a cylindrical vessel/crucible heated by the surrounding graphite [17].

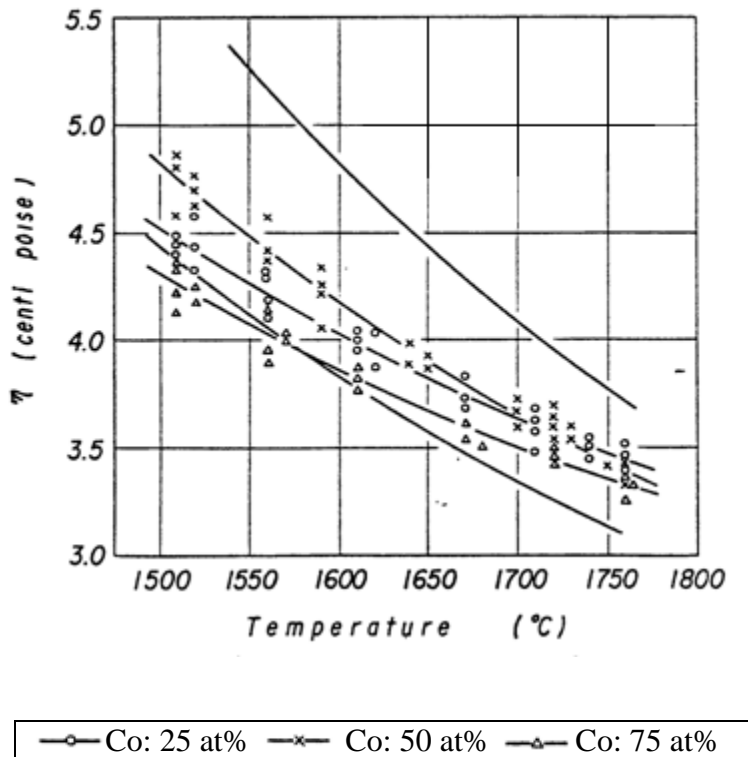


**Figure 14: Graph showing Watanabe's viscosity plots with temperature for Fe(75%)-Co(25%), Fe(50%)-Co(50%), and Fe(25%)-Co(75%).**

Rüdiger-Albert Eichel and Ivan Egry (1999) evaluated the surface tension of liquid Fe-Co and Co-Cu as functions of temperature and concentration (Figure 15) using the oscillating drop technique on the alloy sample droplets formed upon



the melting and alloying of the different metal pieces due to the electromagnetic levitation field [37].

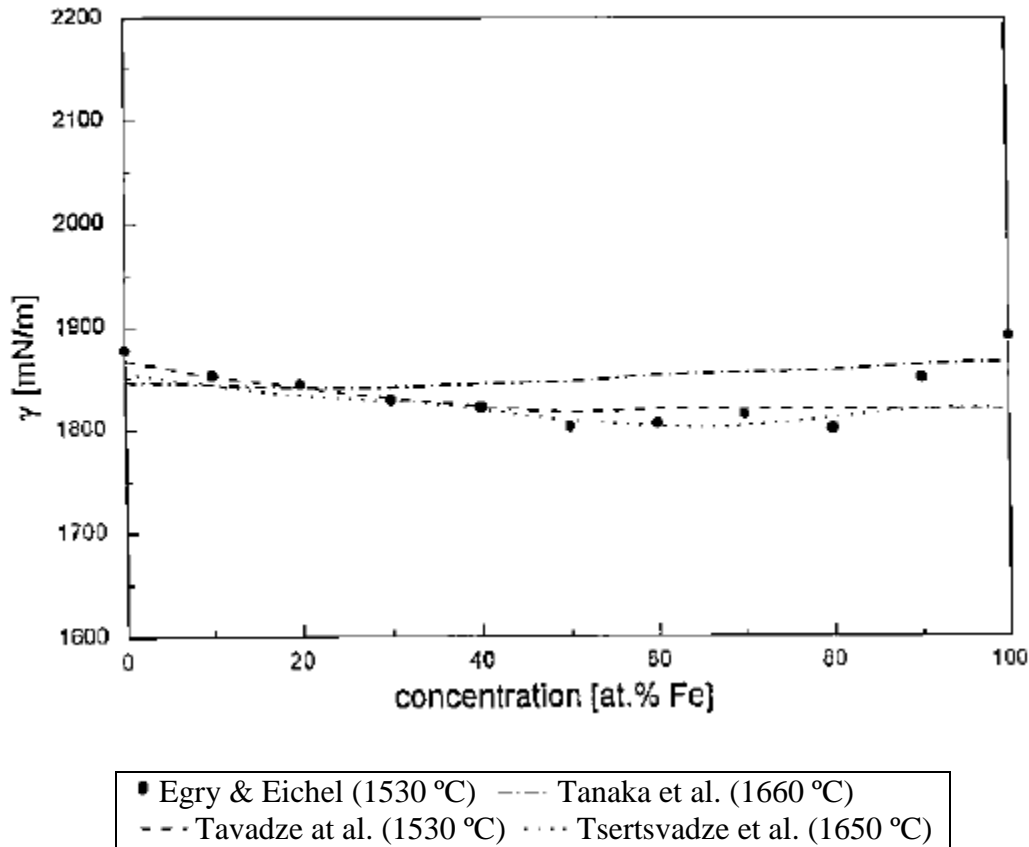


**Figure 15: Graph showing the plot by Egry and Eichel compared to previous published plots, displaying the Fe-Co surface tension-Fe atomic concentration relationship at the given liquidus temperatures.**

In addition, John Li (2009) performed surface tension and viscosity tests on different alloy concentrations of Si-Ge, namely Si(25%)-Ge(75%), Si(52%)-Ge(48%), and Si(78%)-Ge(22%), and obtained similar trends for each property with respect to temperature as above. As the temperature increases, the viscosity and surface tension fall. Li also measured the viscosity of a number of Bulk Metallic Glasses (BMGs) in the high-temperature liquid region, and obtained an

Arrhenius relationship between the viscosity and the temperature. John Li used the electrostatic levitator at Caltech to carry out these measurements [25].

Further support of the theory of surface tension decreasing linearly with temperature in undercooled melts is present in the work of Ivan Egry et al. (1995) where the aforementioned relationship exists for liquid  $Au_{56}Cu_{44}$ . The surface tension was measured using electromagnetic levitation and the oscillating drop technique [11, 15]. In the same year, Mark Przyborowski et al. (1995) came up with a similar relationship between the surface tension and temperature for molten silicon using the same means [14]. Later on, Won-Kyu Rhim and Takehiko Ishikawa (2000) obtained similar linear relationships for the surface tension and density with respect to temperature, through measuring these properties for molten germanium using the High Temperature Electrostatic Levitator (HTESL) at the Jet Propulsion Laboratory in Caltech [20, 26]. In the same year (2000), Yuzuru Sato et al. obtained the linear relationship for the density of molten germanium, as well as the Arrhenius relationship between the viscosity and temperature [27].

Additionally, two years earlier, K. Ohsaka et al. (1998) generated the same Arrhenius relationship between the viscosity and temperature for different atomic concentrations of the liquid alloy Ni-Zr, subjected to electrostatic levitation. G. Lohofier et al. also derived an Arrhenius relationship between the viscosity and temperature for the alloy Co(80%)-Pd(20%) (2001), having performed the experiments in the EML facility TEMPUS during the MSL-1 Spacelab mission

[19]. The graph of the viscosity versus temperature for the alloy NiZr, Ni(36%)-Zr(64%),  $NiZr_2$ , and Ni(24%)-Zr(76%) is shown below in Figure 16 [20, 28]:

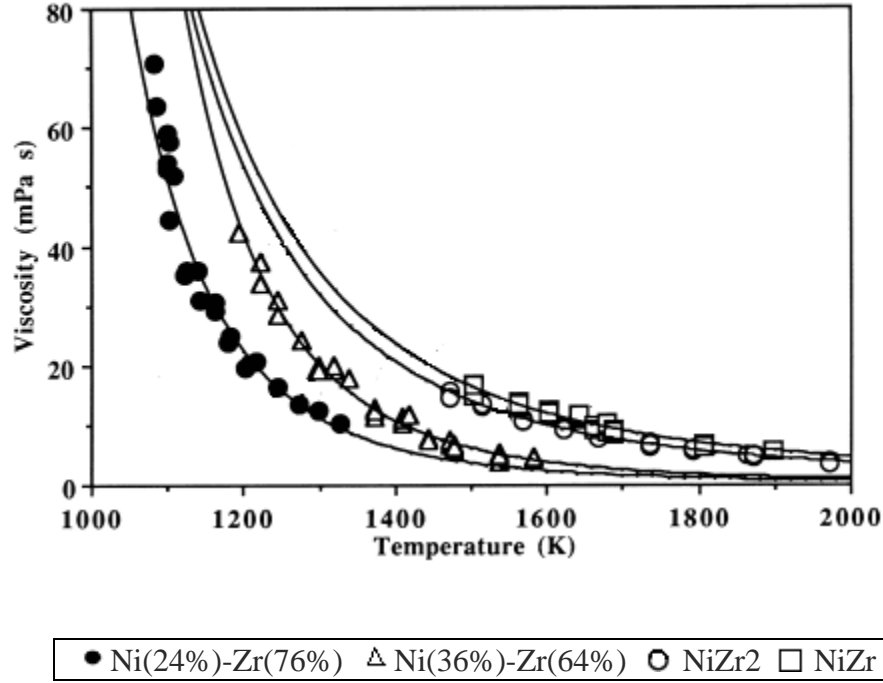


**Figure 16: Graph illustrating the Arrhenius relationship of the viscosity with temperature for the alloys NiZr and NiZr<sub>2</sub>.**

At high temperatures, the evaporation of the Fe-Co alloy sample's external layers occurs, therefore reducing the sample's mass and affecting the atomic composition of the iron and cobalt elements. Therefore, we are compelled to account for and numerically calculate the compositions and masses of both elements at each time interval during the thermal cycle. This composition and mass change especially occurs in the region encapsulated by both melt plateaus in the thermal cycle.

At each time interval, the mass flux is calculated for each of the iron and cobalt elements of the alloy, and it is subtracted from the original mass of the element at that corresponding time interval, in order to generate the mass for the next time interval, and hence the new composition for the next time interval.

First of all, the vapor pressure in vacuum conditions ( $P_{vac}$ ) is calculated at each time interval, accounting for the absolute temperature  $T$  at each time interval, using the following vapor pressure equation [30]:

$$\log_{10} P_{vac} = \frac{A}{T} + B \log_{10} T + CT + DT^2 + E$$

The constants A, B, C, D, and E are coefficients for the vapor pressure equation, and are obtained (for each element) from Table 1 shown below. There is a set of constants for iron, and a different set of constants for cobalt [30].

**Table 1: Table showing the coefficient values of the vapor pressure equation for the given elements.**

$\log_{10} p = AT^{-1} + B \log_{10} T + CT + DT^2 + E$					
Element	$A \times 10^{-3}$	$B$	$C \times 10^3$	$D \times 10^7$	$E$
Ac	-17.7341	17.2465	-5.17499	5.14609	-41.2601
Ag	-14.6161	2.89719	-1.73349	1.88393	2.16168
Al	-21.2723	-20.8781	5.10048	-4.76838	71.9262
Am	-12.8443	4.51889	-1.84623	2.14564	-4.77711
As <sub>4</sub>	-10.1229	-23.8712	17.2518	-46.7800	72.9144
At <sub>2</sub>	-11.4698	-102.302	96.3406	-356.743	261.151
Au	-10.8341	28.4756	-6.28179	4.92752	-78.2602
B	-11.5438	54.6475	-10.0179	6.46365	-161.488
Ba	-6.79902	17.5307	-7.66757	10.9540	-40.7911
Be	-16.4158	4.07537	-1.71749	1.60266	-1.65282
ΣBi	-7.80776	18.5666	-9.00512	14.5289	-41.8270
ΣC	-66.2865	-61.9691	8.90609	-4.75218	214.399
Ca	-8.14332	10.7485	-5.52755	7.61326	-20.0282
Cd	-7.03178	-6.41839	-4.72486	7.24139	28.6976
Ce	-30.9855	-29.6790	5.51952	-3.70988	101.825
Co	-7.00440	54.1831	-12.0134	9.31868	-155.981
Cr	-13.5048	33.6576	-9.29028	8.38147	-89.2017
ΣCs	-3.31260	9.37850	-8.75464	25.7349	-15.5653
Cu	-22.0262	-12.3445	1.09189	2.26164	49.9838
Dy	-14.2933	7.31737	-2.91644	2.62705	-11.1896
Er	-24.6963	-27.1995	4.94931	-3.80748	94.0684
Eu	-7.31387	15.0789	-7.26914	10.1959	-32.5243
Fe	-24.6099	-8.32083	6.68600	-3.04822	38.0026
Fr	-1.73063	24.7577	-18.8857	49.6180	-55.5492
Ga	-12.9207	4.16752	-1.21743	1.30174	-3.82918

Second, we account for the non-vacuum condition in which the experiment is performed. For each metal component, we calculate the vapor pressure ( $P_v$ ) using the following equation, which includes the arbitrary gas pressure  $p$  and the vapor pressure in vacuum conditions  $P_{vac}$  [31]:

$$P_v = P_{vac} * \frac{1}{1 + 0.012 * p}$$

From the vapor pressure, the evaporation flux  $J$  can be calculated, for each metal component, using the following equation [32, 34, 35]:

$$J = \frac{\alpha P_v}{\sqrt{2\pi MRT}}$$

$\alpha$  is an evaporation coefficient to be determined,  $M$  is the molecular weight of the element in question (iron or cobalt) and  $R$  is the universal gas constant.

The metal component flux calculated is in mass units per second per unit area. To calculate the flux in unit mass, we multiply the flux calculated by 0.06 seconds (time interval) and the area of the iron or cobalt part of the sample. The area of each metal component of the sample is calculated by multiplying its atomic fraction by the total sample area. The total sample area is calculated using the following formula:

$$Total\ Area = 4\pi * \left( \frac{Sample\ Mass}{Density} \times \frac{3}{4\pi} \right)^{2/3}$$

Finally, as previous stated, the mass at the next time interval can be calculated by subtracting the aforementioned mass flux from the mass at that time interval, as shown in the following equation:

$$m_{t+0.06} = m_t - J_t$$

From the mass of each element (Fe and Co); the element's composition can be calculated.

## Methodology

We are performing the testing and analysis on the alloy Fe-Co. We are using two concentrations: Fe(50%)-Co(50%) and Fe(45%)-Co(55%).

There will be studies of the thermophysical properties (density, viscosity and surface tension) of these alloys, performed through a range of temperatures. We will attempt to monitor the samples, which undergo the thermal cycle during electrostatic levitation, through their images captured by the Redlake camera. I will explain the thermal cycle in the diagrams below. For viscosity and surface tension evaluation, the camera operates in high-speed mode at a rate of 1000 frames/second. For density evaluation, the camera operates at a lower speed at a rate of 5 frames/second. Both evaluations can be performed in the same cycle.

The study on the thermophysical properties would involve temperature-time profiles derived from pyrofiles, as well as video files. The video files are clips in .AVI format, and could be viewed with Windows Media Player. In the ESL chamber, the samples themselves that are electrostatically levitated by the charged electrodes and heated by the laser are spherical, arc-melted Fe-Co samples in the mass range of 40-55 mg. The pyrometer used to detect the wavelength of the light emitted from the sample is a single-color pyrometer, where temperature-time data was recorded at time intervals of 0.06 seconds. The pyrometer's model name is Impac IGA 140, s/n 446. Its wavelength range is 1.45-1.8  $\mu\text{m}$  and its temperature range is 300 to 2500  $^{\circ}\text{C}$ .

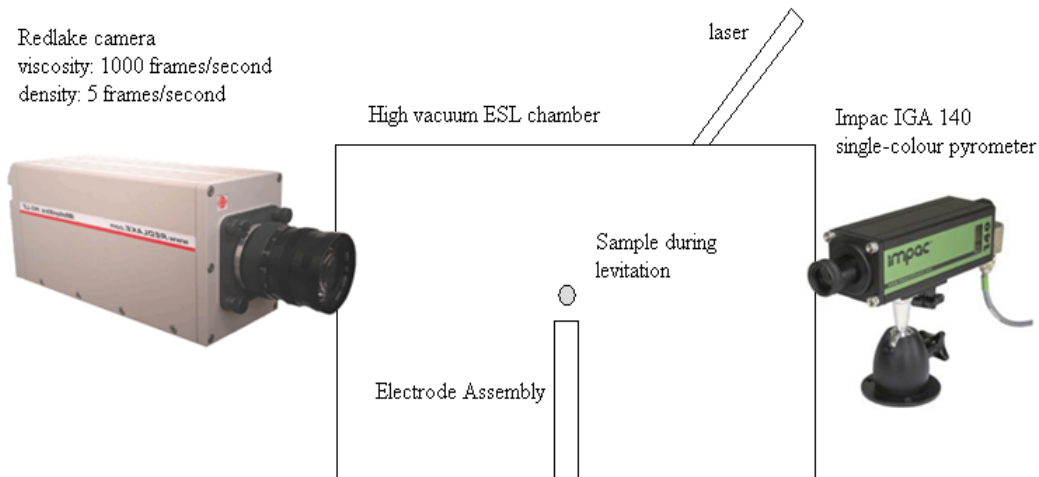


**Figure 17: Simplified schematic illustrating the key apparatus of the electrostatic levitator at MSFC, NASA.**

The following picture (Figure 18) depicts the electrostatic levitator used at MSFC, NASA:

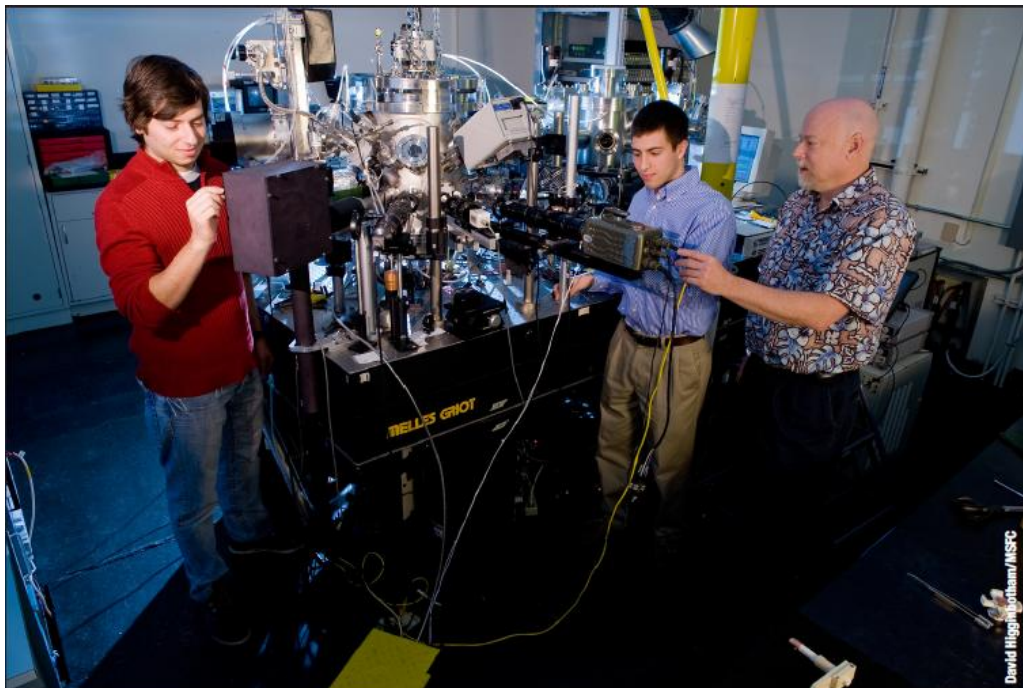


**Figure 18: Picture showing the electrostatic levitator in which the Fe-Co samples underwent tests, at MSFC, NASA.**



### Cases of the thermal profile

The theoretical operations at MSFC would involve the following thermal cycles:

First of all, we melt the sample and after cooling it, we arrest the temperature at a superheated level (temperature greater than melting temperature by 30 degrees) for about 10 seconds. While cooling it to the superheated level, we obtain the density values as a function of temperature. We perform three (or more) deformations to obtain the viscosity before and after each deformation. We then allow the sample to cool below its melting temperature and collect the density as a function of temperature. We also collect the surface tension data. The deformations transform the sample's composition irrevocably. We save the data. The initial aim for the superheated temperature is a temperature 30 degrees greater than the melting temperature.

The temperature profile (temperature vs. time) for this operation is shown in

Figure 19:

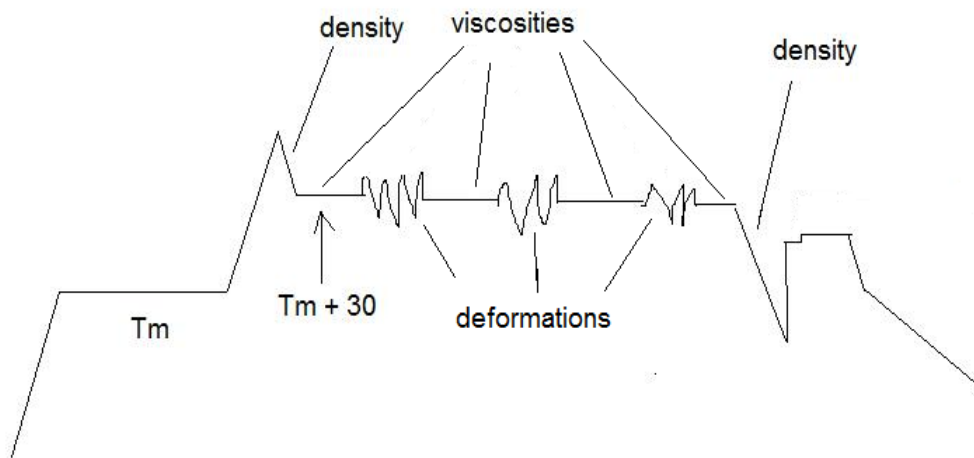


**Figure 19: Diagram showing thermal profile of sample in the case of isothermal viscosity tests performed at a temperature 30 °C greater than the melting point.**

Second, we melt the sample and let it undercool to a temperature less than the melting temperature by 30 degrees. While cooling it, we obtain the density values as a function of temperature. We arrest the temperature for about 10 seconds and perform three deformations (or more) in order to obtain the viscosity before and after each one. We also collect the surface tension data. We then allow the sample to cool and collect the density as a function of temperature. We save the data. The initial aim for the undercooled temperature is a temperature 30 degrees less than the melting temperature.

The temperature profile for this operation is shown in Figure 20:

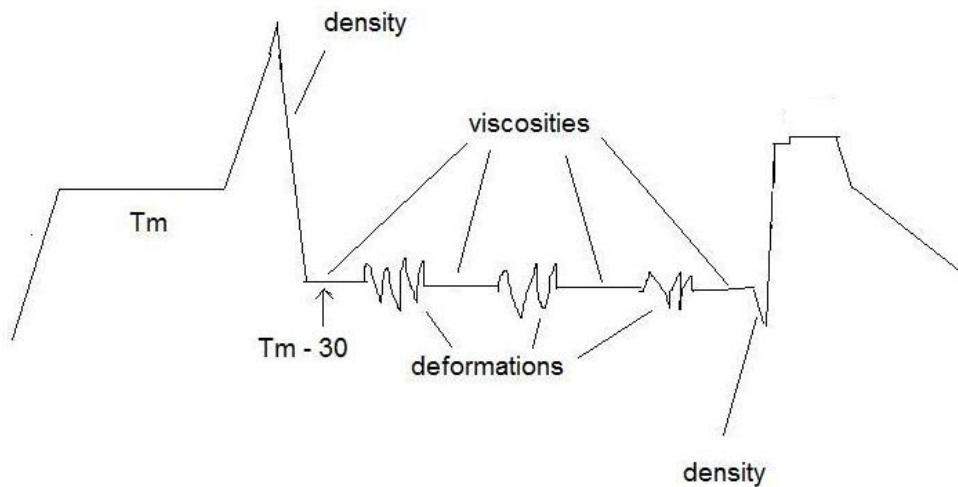


**Figure 20: Diagram showing thermal profile of sample in the case of isothermal viscosity tests performed at a temperature 30 °C less than the melting point.**

The above two processes are elemental; the idea is to establish a relationship between the laser setting and the thermal hold temperature, since the laser itself is

responsible for the heating and temperature of the sample. Additionally, we don't perform deformations while the sample cools to its superheated or undercooled state, since these deformations affect the sample's density, and we need the initial density data during the thermally dynamic stage of the temperature profile. Next, we melt the sample, and while cooling it to an undercooled temperature (cooling through a range of approximately 50 degrees) we perform the deformations. We account for the density as a function of temperature as well as the viscosity as a function of temperature in this thermally dynamic region; in the previous two cases, the viscosity measurements were taken in thermally static conditions. We don't account for the laser setting in this region. The temperature profile for this operation is shown in Figure 21:

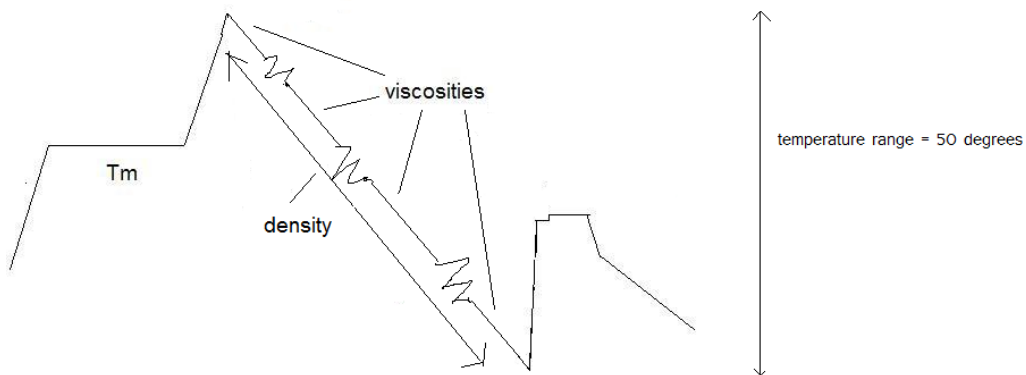


**Figure 21: Diagram showing thermal profile of sample in the case of thermotransient viscosity tests performed down a temperature range of 50 °C, from the thermal peak to the lowest temperature before recalescence occurs.**

Then, we use the same sample that we ran earlier; we melt it and cool it to its initial melting temperature and arrest it to that temperature for a longer period of

time than the first two examples above: approximately 30 seconds. Due to the lengthy period of time, there is a significant change in sample composition as the sample undergoes the deformations. The aim here is to obtain viscosity as a function of composition at the melting temperature. We save the data as usual.

The temperature profile for this operation is shown in Figure 22:

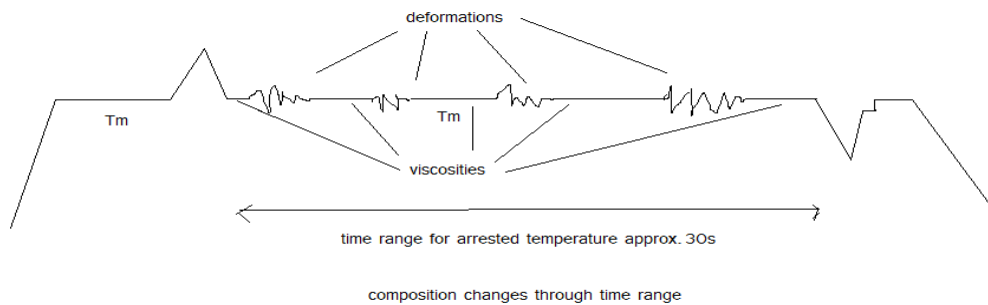


**Figure 22: Diagram showing thermal profile of sample in the case of isothermal viscosity tests performed at a temperature equal to the melting point.**

Lastly, we perform tests for a new sample similar to the scenario in Figure 21 (executing deformations while cooling the sample and taking density and viscosity measurements) before re-melting the same sample. However, we now cool the sample to a pre-chosen superheated temperature or to a pre-chosen undercooled temperature. We repeat this process several times, and again, we save the data.

### **Composition Analysis:**

We had sent a group of Fe-Co samples from our January 2011 analysis to Luvak Inc., a company that specializes in the analysis of alloying metals, in order to

perform weight percentage analysis of each of the alloy components in the samples. The method used for this analysis is direct current plasma emission spectroscopy – ASTM E 1097-07. The samples were levitated and tested at MSFC. We obtained a list of results on the samples from Luvak Inc. The final weight percentages of Fe and Co for the samples are needed in order to determine the optimum evaluation of the aforementioned evaporation coefficient,  $\alpha$ .

On a different set of tests on a different set of samples, the obtained evaporation coefficient is then used in calculating the proper mass flux  $J$ , at each time interval throughout the thermal cycle, in order to determine the masses and compositions of the samples throughout their thermal cycles.

The importance of the final weight percentages, for the samples sent to Luvak Inc. for elemental analysis, is present in the fact we can calculate the actual final individual masses for iron and cobalt respectively, and compare them to the corresponding predicted (calculated) values using the method of decrements due to (flux) evaporation loss for every time interval. The result of this comparison would support the decision to use the method we are using to estimate the masses and compositions of iron and cobalt at each time interval.

In our calculations, we initially assume the value of the evaporation coefficient  $\alpha$  to be unity, and after generating the predicted total final mass (the sum of the predicted final masses of iron and cobalt), we divide it by the actual total final mass. The answer should be close to unity, but it is not. Next, through the process of trial and error as well as mental numerical interpolation, we try different values

of  $\alpha$  and keep generating the ratio of the predicted final mass to the actual final mass, until we get unity. Once we achieve that, we record the value of the evaporation coefficient  $\alpha$ . We perform the same operation for the rest of the samples which underwent elemental analysis at Luvak Inc. and record the values of  $\alpha$  for each sample, always bearing in mind that the individual respective masses of Fe and Co are very close to their predicted counterparts, hence resulting in a very close proximity between the actual and predicted final masses.

The samples which underwent elemental analysis at Luvak Inc. were all subjected to isothermal viscosity tests. Therefore, we will attempt to see if there is a link to be established between the temperature at which the sample underwent the viscosity test, and the value of the evaporation coefficient. Our aim is to observe whether the coefficient  $\alpha$  is a constant value, or if it is linear with temperature. The result of this study would be the input in our mass flux calculations for different samples' density and viscosity tests, therefore enabling us to use the accurate masses in the calculations for their density, (isothermal and thermotransient) viscosity and surface tension values. Finally, we would be able to establish whether or not the evaporation coefficient is dependent on temperature.

## Experimental Results

### Composition Results:

Our composition analysis for the samples sent to Luvak Inc. for testing yielded the following values (Table 2) for the evaporation coefficient,  $\alpha$  (samples underwent viscosity testing at given temperatures):

**Table 2: Table showing the values of the evaporation coefficients obtained upon performing evaporation and composition analysis on the samples sent to Luvak Inc. for elemental analysis; the samples underwent viscosity tests at MSFC at the given temperatures.**

Sample	Evaporation coefficient, $\alpha$	Temperature (K)
MAT-376	0.8997	1771.31
MAT-378	0.8241	1678.94
MAT-391	0.9560	1754.63
MAT-392	0.9823	1842.51
MAT-393	0.8350	1766.52
MAT-396	0.9431	1800.85

Evaporation coefficient equation to be used:  $\alpha = 0.000918 * T - 0.717$

The equation is obtained through performing a linear fit on the evaporation coefficient values with respect to their corresponding temperatures.

The evaporation coefficient values were based on the results of our composition analysis for the samples themselves.

Table 3 depicts the samples' weights and compositions before and after the viscosity testing is performed on the samples:

**Table 3: Table showing the values of the initial and final masses and weight compositions of the samples sent to Luvak Inc.**

Sample	MAT-376	MAT-378	MAT-391	MAT-392	MAT-393	MAT-396
Initial Mass Fe (mg)	24.16	20.37	19.00	19.51	18.62	20.25
Initial Mass Co (mg)	25.86	21.82	20.33	21.33	20.15	21.23
Initial Total Mass (mg)	50.02	42.19	39.33	40.84	38.77	41.49
Final Mass Fe (mg)	23.15	18.60	16.88	17.17	17.82	18.81
Final Mass Co (mg)	24.94	21.02	20.10	19.87	19.19	20.83
Final Total Mass (mg)	48.14	39.66	37.01	37.08	37.05	39.68
Initial Wt% Fe (mg)	0.483	0.483	0.483	0.478	0.480	0.488
Initial Wt% Co (mg)	0.517	0.517	0.517	0.522	0.520	0.512
Final Wt% Fe (mg)	0.481	0.469	0.456	0.463	0.481	0.474
Final Wt% Co (mg)	0.518	0.530	0.543	0.536	0.518	0.525



The description of the structure of the results for each of the samples is as follows:

- A table displaying the masses and atomic percentages of the iron and cobalt components of the sample, as well as the total mass of the sample. There are three sets of values, namely values representing the initial stage (before viscosity testing) and final stage (after viscosity testing), as well as values calculated using the flux evaporation method (after viscosity testing). Also included is the mass percentage difference between the actual final mass and the calculated (using the flux evaporation method) final mass of the sample. Table 4 is an example of the results for sample MAT-376.
- The sample's temperature (°C) vs. time (s) plot, representing the performed test.
- A technical description of the viscosity runs and the average temperature of each. The average temperature of all runs is calculated and accounted for. A typical graph for this analysis is shown in Figure 23.

## **MAT-376 TSA-3 Fe(50%)-Co(50%) Viscosity**

**Table 4: Table showing the initial values, actual final values and calculated final values of the masses and atomic compositions of the sample MAT-376, as well as the mass percentage difference between the actual and calculated final masses.**

	Mass Fe (mg)	Mass Co (mg)	Total Mass (mg)	At% Fe	At% Co	Mass % difference
Initial	24.16	25.86	50.02	0.496	0.504	
Actual	23.15	24.94	48.14	0.495	0.505	
Flux Evaporation Method	22.65	25.28	47.93	0.486	0.514	0.43

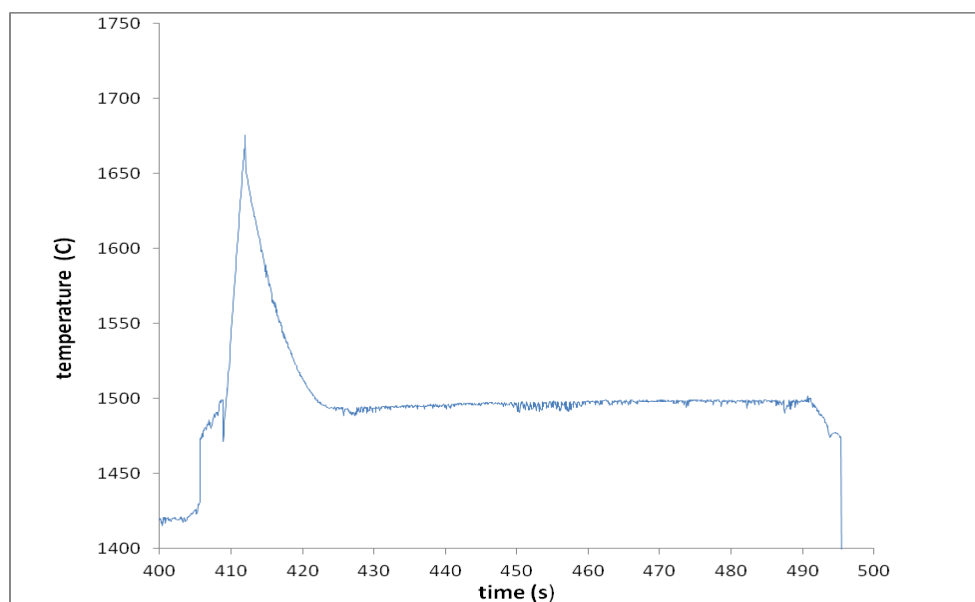


**Figure 23: Figure showing the section of the thermal cycle of MAT-376 where the sample underwent viscosity tests.**

- We accounted for two viscosity runs for this sample.
- The average temperature for each run is 1498.33 °C and 1498.10 °C, respectively.
- The average temperature of both viscosity runs is 1498.16 °C.

## **MAT-378 TSA-5 Fe(50%)-Co(50%) Viscosity**

**Table 5: Table showing the initial values, actual final values and calculated final values of the masses and atomic compositions of the sample MAT-378, as well as the mass percentage difference between the actual and calculated final masses.**

	Mass Fe (mg)	Mass Co (mg)	Total Mass (mg)	At% Fe	At% Co	Mass % difference
Initial	20.37	21.82	42.19	0.496	0.504	
Actual	18.60	21.02	39.66	0.483	0.517	
Flux Evaporation Method	18.24	20.90	39.14	0.479	0.521	1.31

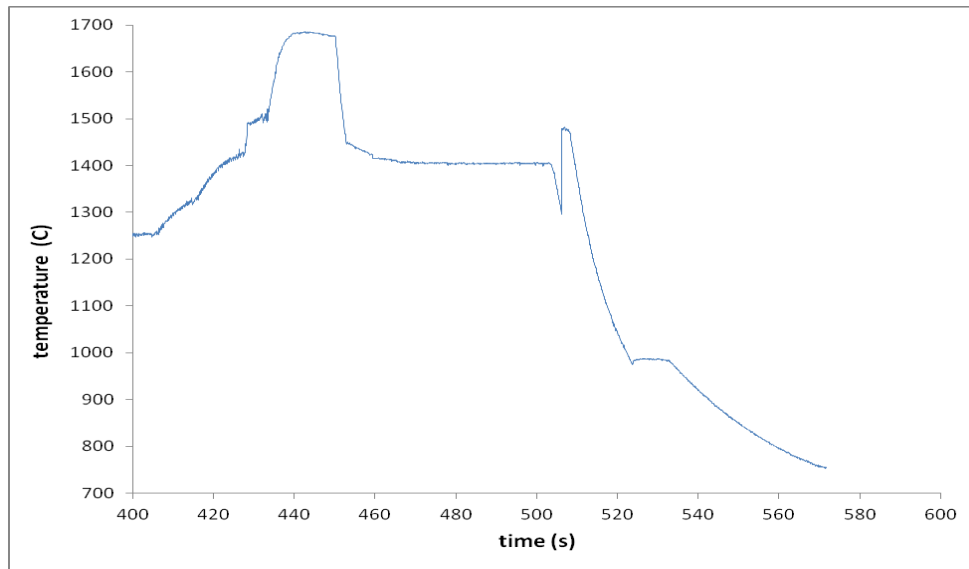


**Figure 24: Figure showing the section of the thermal cycle of MAT-378 where the sample underwent viscosity tests.**

- We accounted for four viscosity runs for this sample.
- The average temperature for each run is 1406.96 °C, 1405.49 °C, 1405.62 °C and 1406.05 °C, respectively.
- The average temperature of all four viscosity runs is 1405.79 °C.

## **MAT-391 TSA-13 Fe(50%)-Co(50%) Viscosity**

**Table 6: Table showing the initial values, actual final values and calculated final values of the masses and atomic compositions of the sample MAT-391, as well as the mass percentage difference between the actual and calculated final masses.**

	Mass Fe (mg)	Mass Co (mg)	Total Mass (mg)	At% Fe	At% Co	Mass % difference
Initial	19.00	20.33	39.33	0.452	0.548	
Actual	16.88	20.10	37.01	0.408	0.592	
Flux Evaporation Method	17.27	19.63	37.91	0.416	0.584	0.28

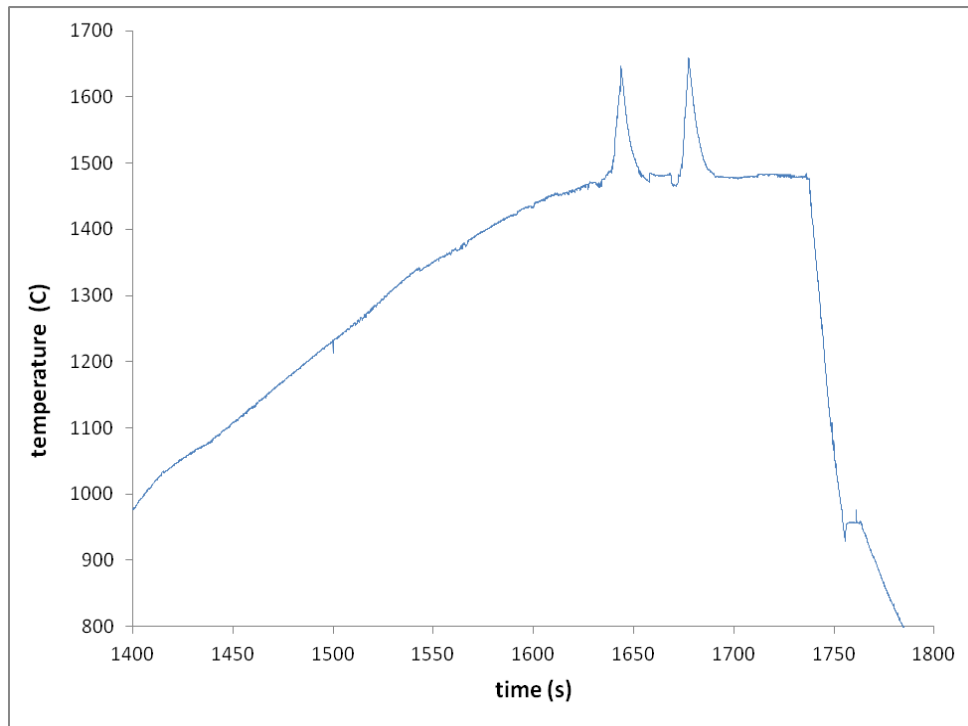


**Figure 25: Figure showing the section of the thermal cycle of MAT-391 where the sample underwent viscosity tests.**

- We accounted for one viscosity run for this sample.
- The temperature for this run is 1481.48 °C.

## **MAT-392 TSA-14 Fe(50%)-Co(50%) Viscosity**

**Table 7: Table showing the initial values, actual final values and calculated final values of the masses and atomic compositions of the sample MAT-392, as well as the mass percentage difference between the actual and calculated final masses.**

	Mass Fe (mg)	Mass Co (mg)	Total Mass (mg)	At% Fe	At% Co	Mass % difference
Initial	19.51	21.33	40.84	0.491	0.509	
Actual	17.17	19.87	37.08	0.477	0.523	
Flux Evaporation Method	15.74	21.24	36.98	0.439	0.561	0.25

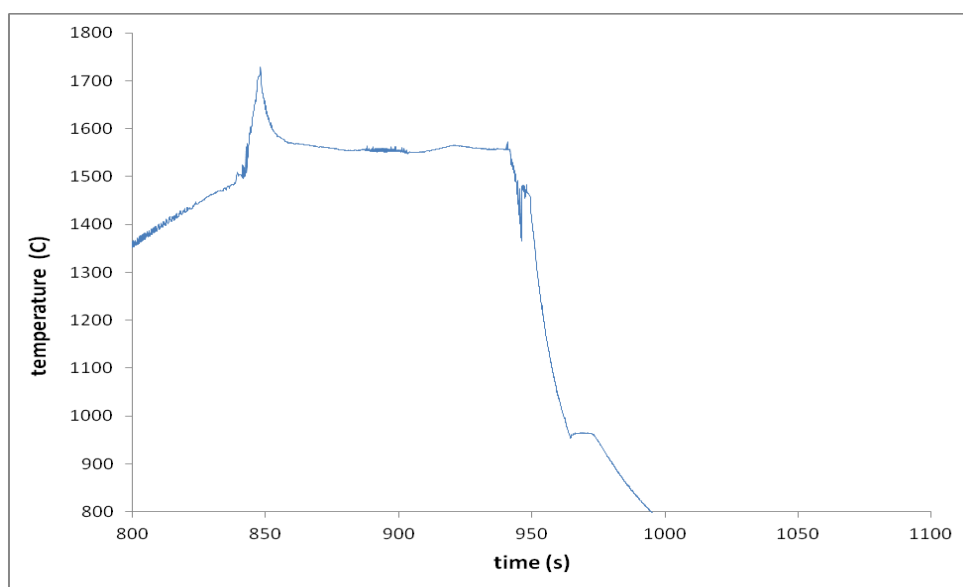


**Figure 26: Figure showing the section of the thermal cycle of MAT-392 where the sample underwent viscosity tests.**

- We accounted for three viscosity runs for this sample.
- The average temperature for each run is 1567.68 °C, 1573.11 °C and 1566.16 °C, respectively.
- The average temperature of all three viscosity runs is 1569.36 °C.

## **MAT-393 TSA-16 Fe(50%)-Co(50%) Viscosity**

**Table 8: Table showing the initial values, actual final values and calculated final values of the masses and atomic compositions of the sample MAT-393, as well as the mass percentage difference between the actual and calculated final masses.**

	Mass Fe (mg)	Mass Co (mg)	Total Mass (mg)	At% Fe	At% Co	Mass % difference
Initial	18.62	20.15	40.84	0.494	0.506	
Actual	17.82	19.19	37.08	0.495	0.505	
Flux Evaporation Method	17.13	19.58	36.98	0.480	0.520	0.90

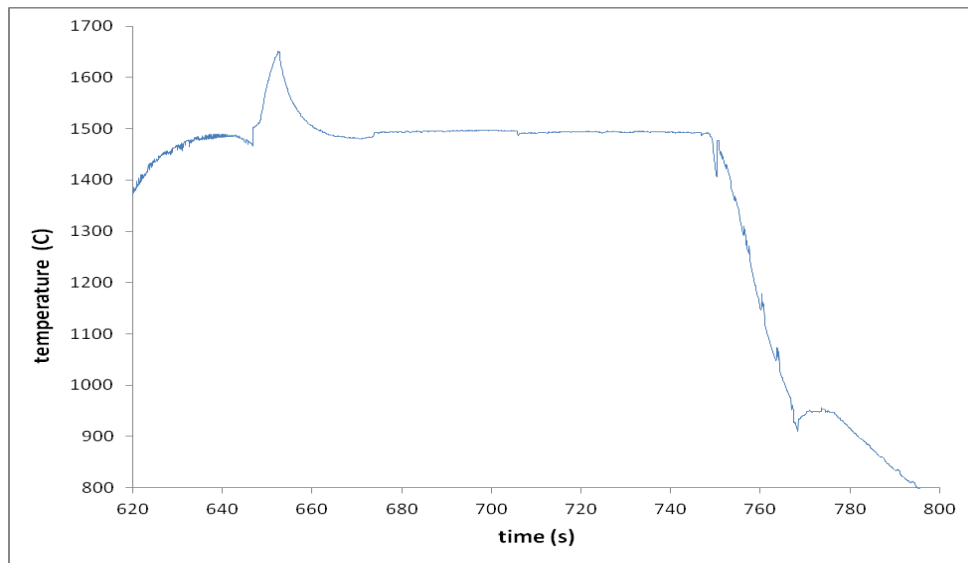


**Figure 27: Figure showing the section of the thermal cycle of MAT-393 where the sample underwent viscosity tests.**

- We accounted for five viscosity runs for this sample.
- The average temperature for each run is 1494.13 °C, 1493.23 °C, 1493.30 °C, 1493.75 °C and 1493.03 °C, respectively.
- The average temperature of all five viscosity runs is 1493.37 °C.

## **MAT-396 TSA-21 Fe(50%)-Co(50%) Viscosity**

**Table 9: Table showing the initial values, actual final values and calculated final values of the masses and atomic compositions of the sample MAT-396, as well as the mass percentage difference between the actual and calculated final masses.**

	Mass Fe (mg)	Mass Co (mg)	Total Mass (mg)	At% Fe	At% Co	Mass % difference
Initial	20.25	21.23	41.49	0.502	0.498	
Actual	18.81	20.83	39.68	0.488	0.512	
Flux Evaporation Method	18.87	20.70	39.57	0.490	0.510	0.27

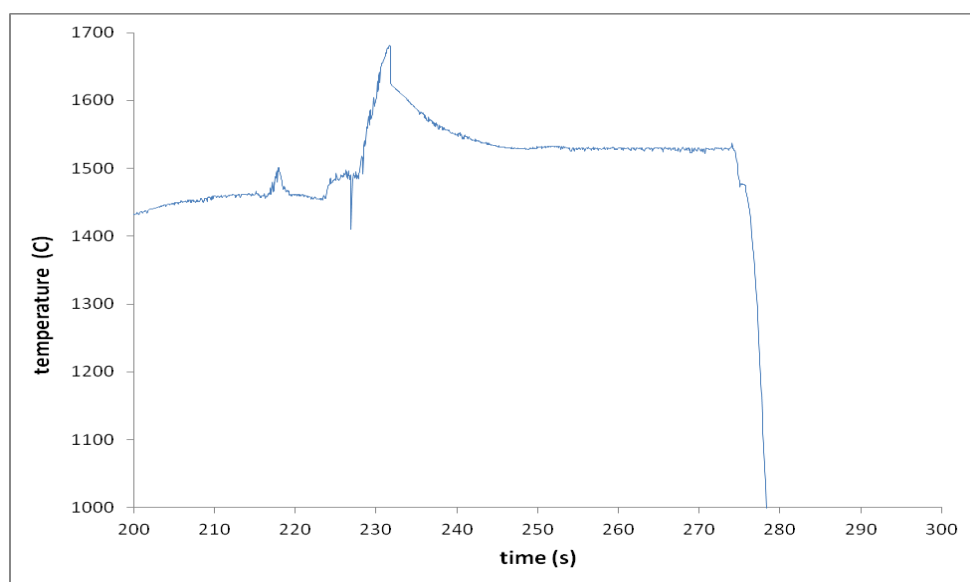


**Figure 28: Figure showing the section of the thermal cycle of MAT-396 where the sample underwent viscosity tests.**

- We accounted for two viscosity runs for this sample.
- The average temperature for each run is 1528.32 °C and 1526.56 °C, respectively.
- The average temperature of both viscosity runs is 1527.70 °C.

Using the linear equation  $\alpha = 0.000918 * T - 0.717$  for the evaporation coefficient, we were able to generate the following graph (Figure 29) and relationship for the liquid region of the Fe(45%)-Co(55%) alloy concentration:

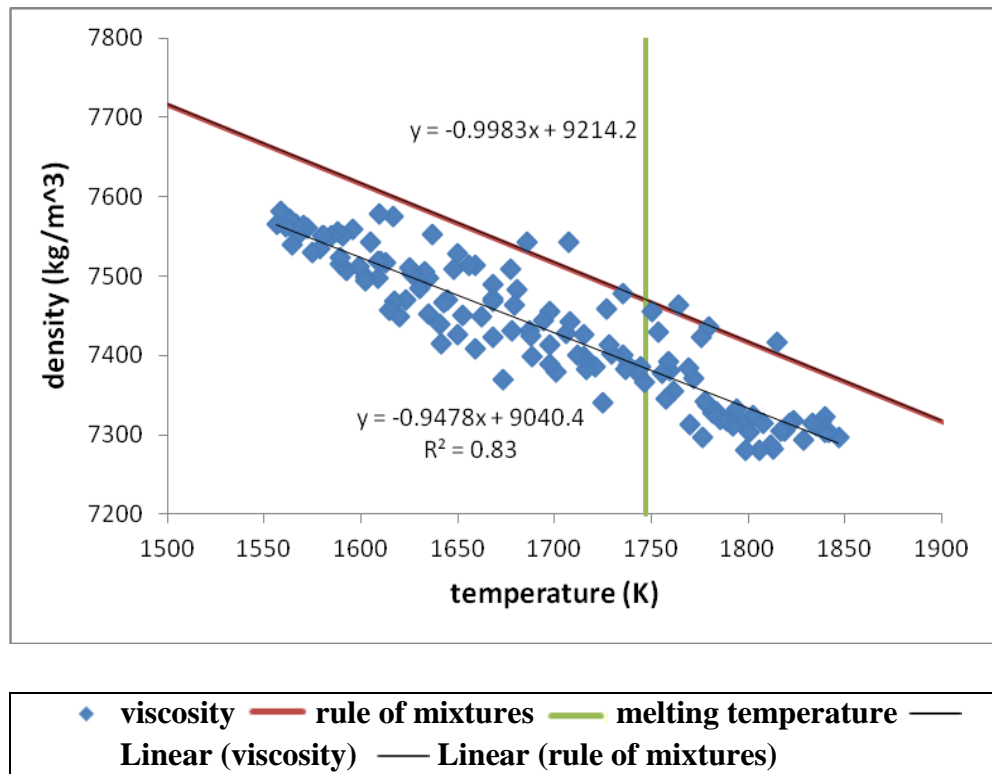


**Figure 29:** Figure showing the liquid section graph of density vs. temperature for the Fe(45%)-Co(55%) alloy sample.



**Table 10: Table showing the experimental and predicted values of the slope and density at the melting temperature for the liquid section density graph of the Fe(45%)-Co(55%) alloy sample.**

Experimental density at melting temperature	7384.59 kg/m <sup>3</sup>
Predicted density at melting temperature	7470.17 kg/m <sup>3</sup>
Percentage difference between densities	1.15%
Experimental slope	-0.9478 kg/(K m <sup>3</sup> )
Predicted slope	-0.9983 kg/(K m <sup>3</sup> )
Percentage difference between slopes	5.06%

The following graphs (Figures 30, 31) obtained are those of the isothermal viscosity for the Fe(45%)-Co(55%) alloy concentration:

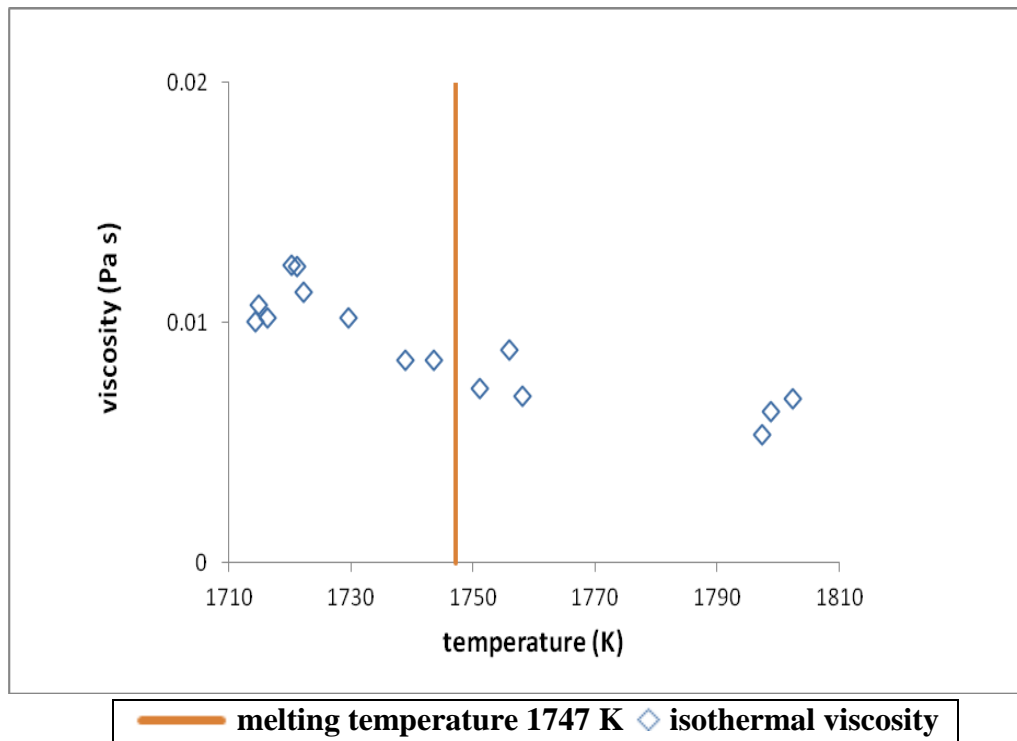


**Figure 30: Figure showing the graph of isothermal viscosity vs. temperature for the Fe(45%)-Co(55%) alloy.**

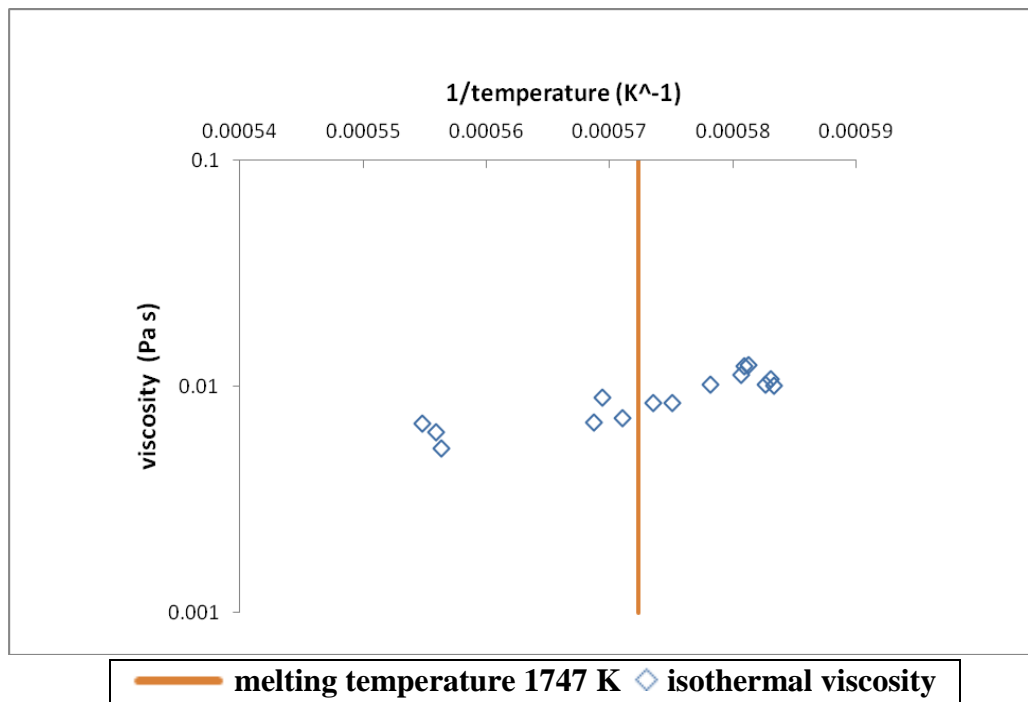


**Figure 31: Figure showing the graph of isothermal viscosity vs.  $1/\text{temperature}$  for the Fe(45%)-Co(55%) alloy.**

The following graph (Figure 32) obtained is that of the isothermal surface tension for the Fe(45%)-Co(55%) alloy concentration:

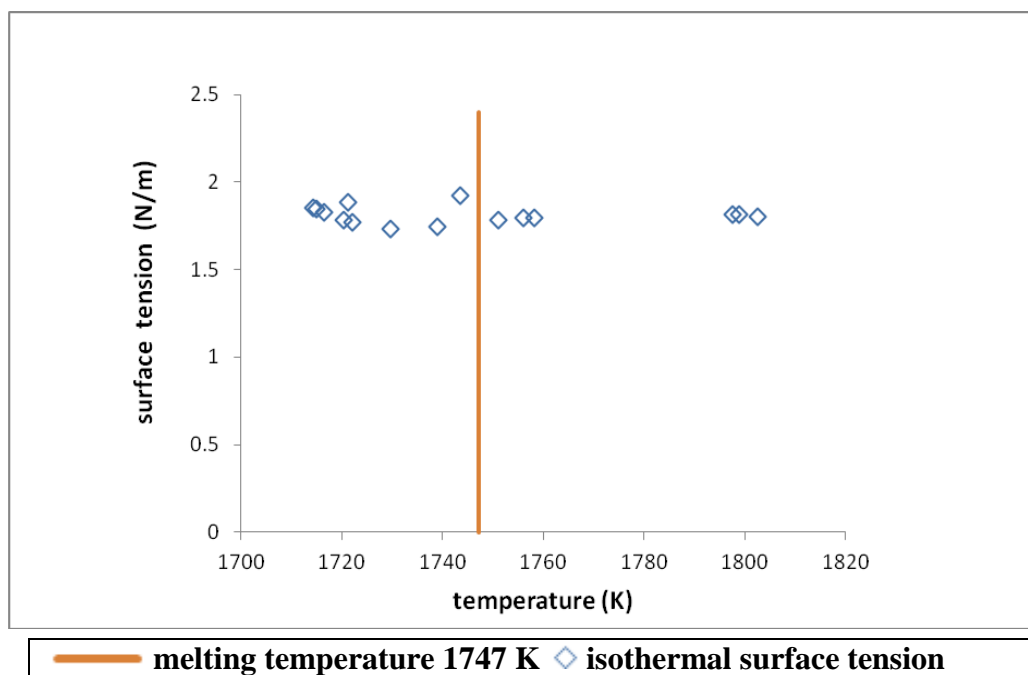


**Figure 32: Figure showing the graph of isothermal surface tension vs. temperature for the Fe(45%)-Co(55%) alloy.**

The following graphs (Figures 33, 34) obtained are those of the thermotransient viscosity for the Fe(45%)-Co(55%) alloy concentration. The three different data sets shown represent cooling viscosity values for three liquid samples whose respective oscillations were damped down different temperature gradients:

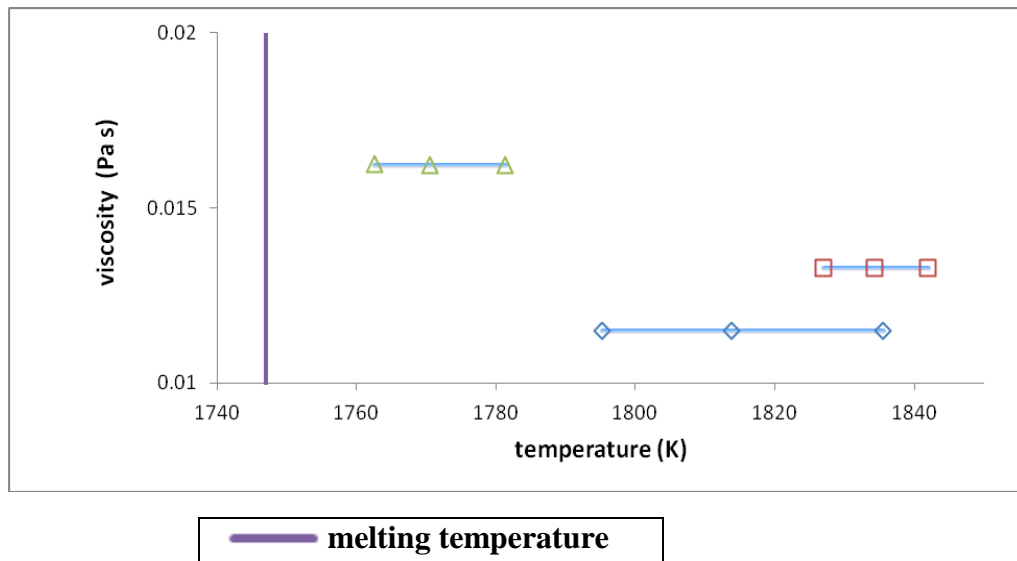


**Figure 33: Figure showing the graph of thermotransient viscosity vs. temperature for the Fe(45%)-Co(55%) alloy.**

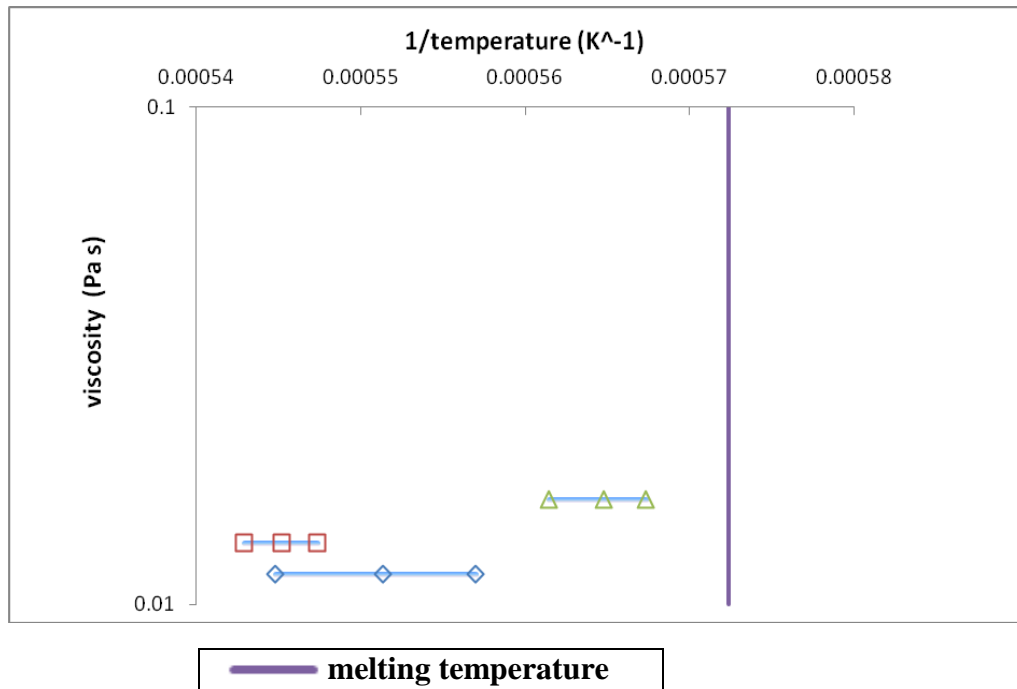


**Figure 34: Figure showing the graph of thermotransient viscosity vs. 1/temperature for the Fe(45%)-Co(55%) alloy.**

Using the linear equation  $\alpha = 0.000918 * T - 0.717$  for the evaporation coefficient, we were able to generate the following graph and relationship for density as a function of temperature for the Fe(50%)-Co(50%) alloy concentration (Figure 35):

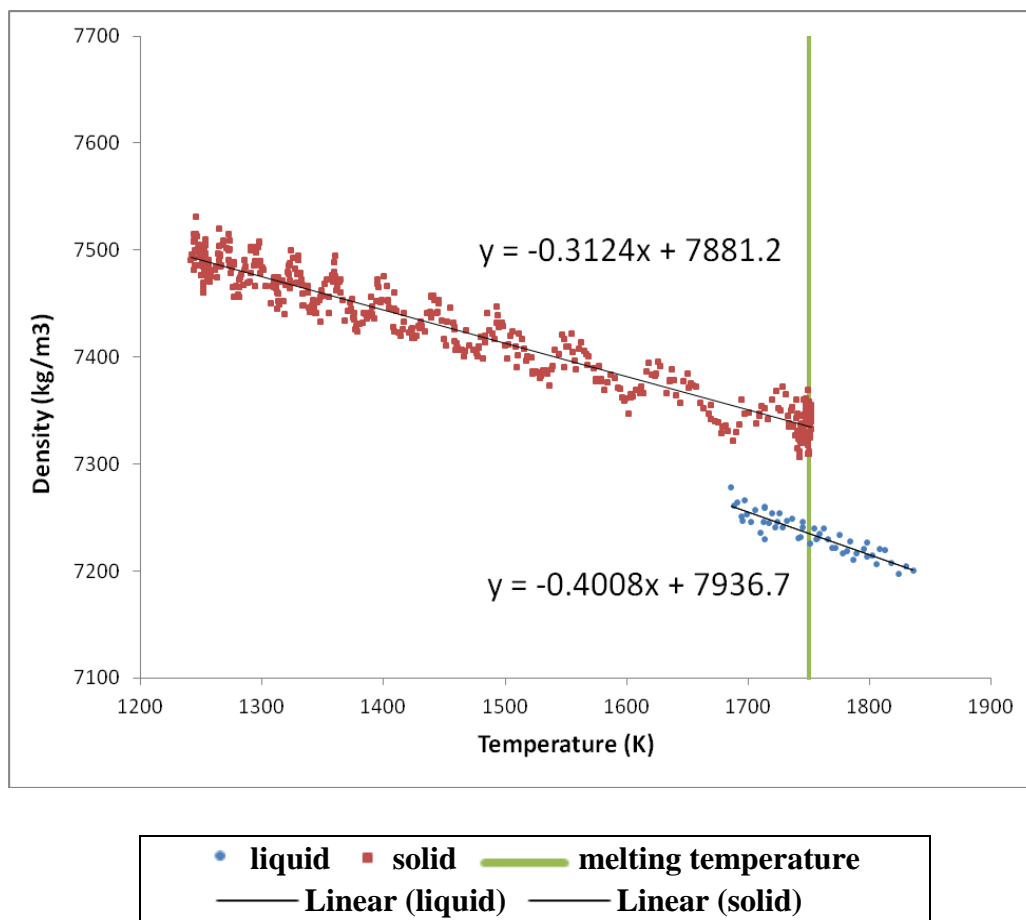


**Figure 35: Figure showing the liquid and solid sections of the graph of density vs. temperature for the Fe(50%)-Co(50%) alloy sample.**

The equations on the graph above represent the density-temperature relationships for the liquid and solid portions of the graph. Table 11 summarizes the findings and the differences between measured and calculated values.

**Table 11: Table showing the experimental and predicted values of the slopes and densities at the melting temperature, for both the solid and liquid sections of the density graph for the Fe(50%)-Co(50%) alloy sample.**

Experimental liquid density at melting temperature	7235.30 kg/(m <sup>3</sup> )
Predicted liquid density at melting temperature	7433.11 kg/(m <sup>3</sup> )
Percentage difference between densities	2.66%
Experimental liquid slope	-0.4008 kg/(K m <sup>3</sup> )
Predicted slope	-0.9878 kg/(K m <sup>3</sup> )
Percentage difference between slopes	59.42%
Experimental solid slope	-0.3124 kg/(K m <sup>3</sup> )
Experimental solid density at melting temperature	7334.50 kg/(m <sup>3</sup> )

The following graphs (Figures 36, 37) obtained are those of the isothermal viscosity for the Fe(50%)-Co(50%) alloy concentration:

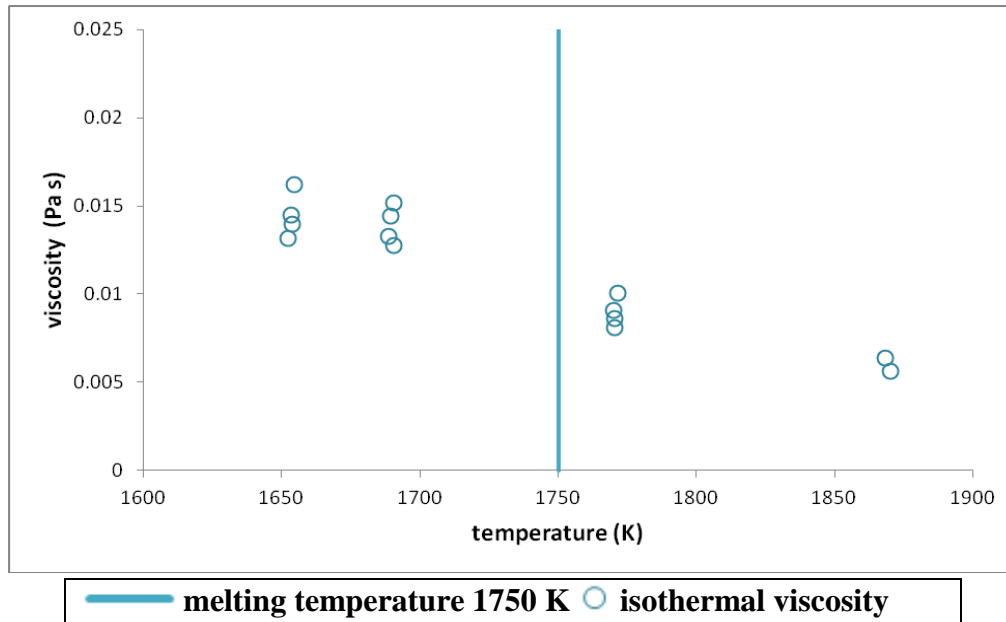


**Figure 36: Figure showing the graph of the isothermal viscosity vs. temperature for the Fe(50%)-Co(50%) alloy.**

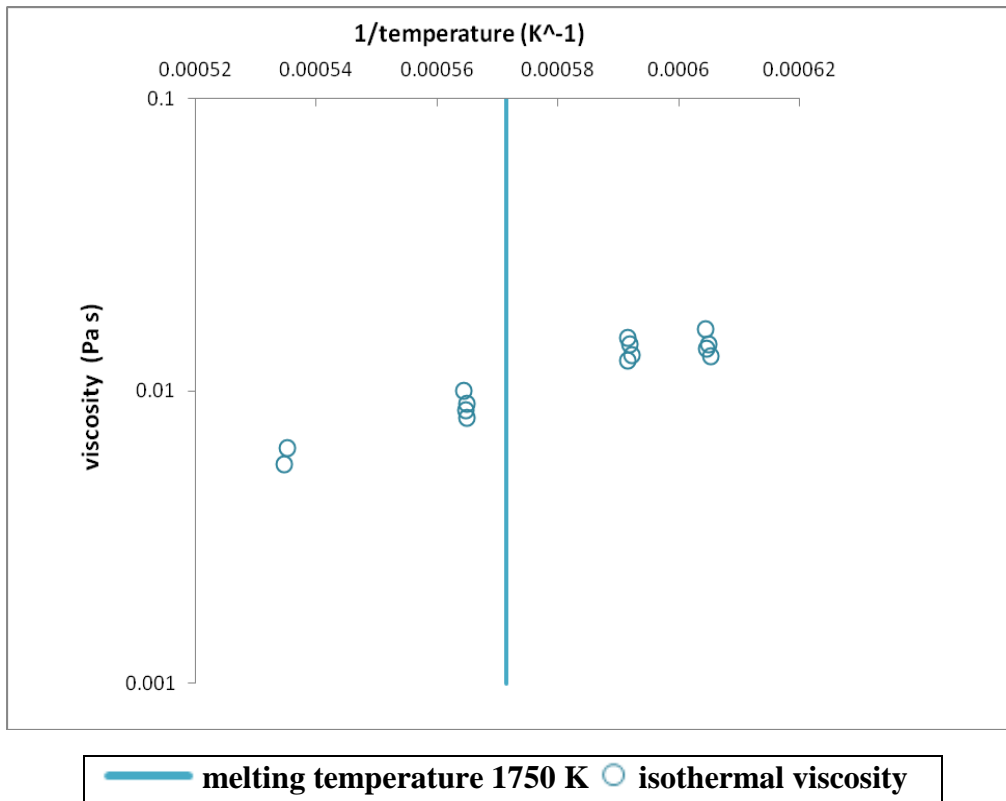


**Figure 37: Figure showing the graph of the isothermal viscosity vs. 1/temperature for the Fe(50%)-Co(50%) alloy.**

The following graph (Figure 38) obtained is that of the isothermal surface tension for the Fe(50%)-Co(50%) alloy concentration:

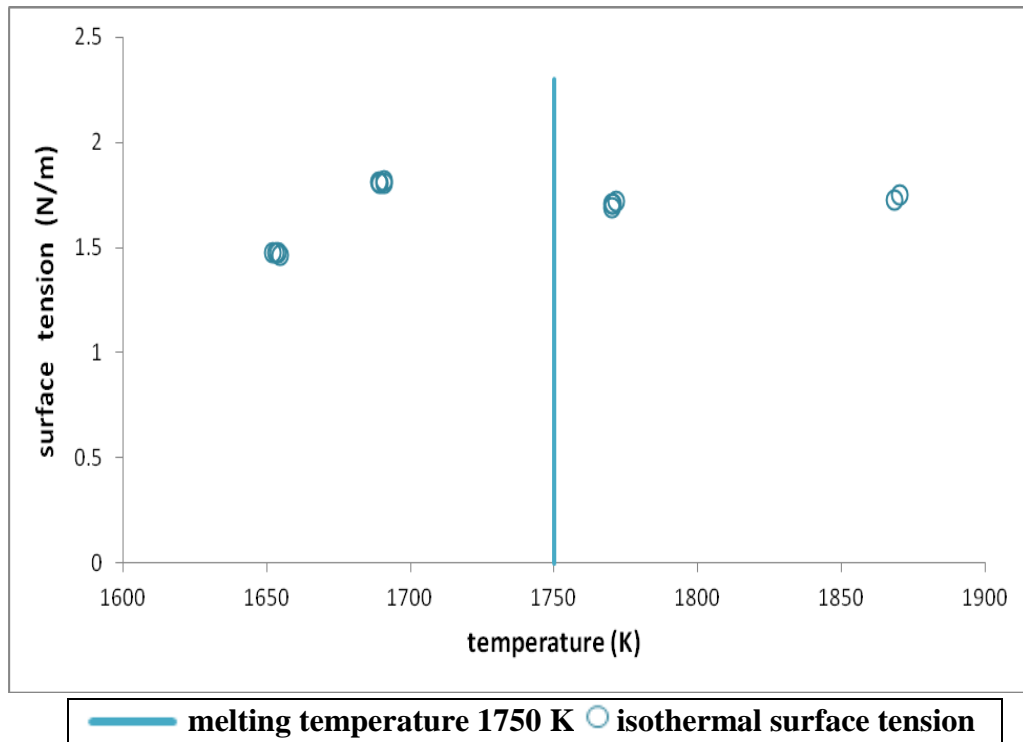


**Figure 38: Figure showing the graph of the isothermal surface tension vs. temperature for the Fe(50%)-Co(50%) alloy.**

The following graphs (Figures 39, 40) obtained are those of the thermotransient viscosity for the Fe(50%)-Co(50%) alloy concentration. The four different data sets shown represent cooling viscosity values for four liquid samples whose respective oscillations were damped down different temperature gradients:



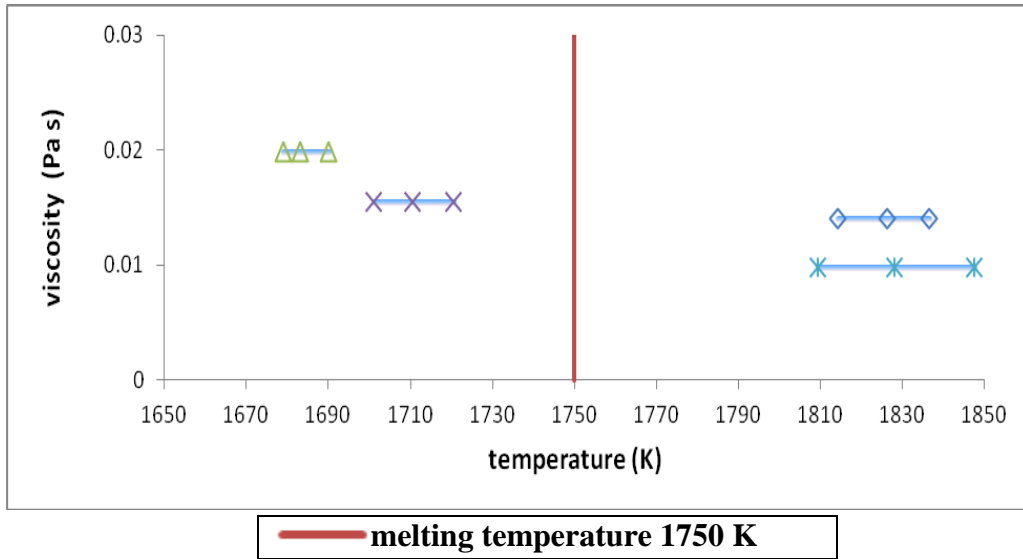


**Figure 39:** Figure showing the graph of the thermotransient viscosity vs. temperature for the Fe(50%)-Co(50%) alloy.

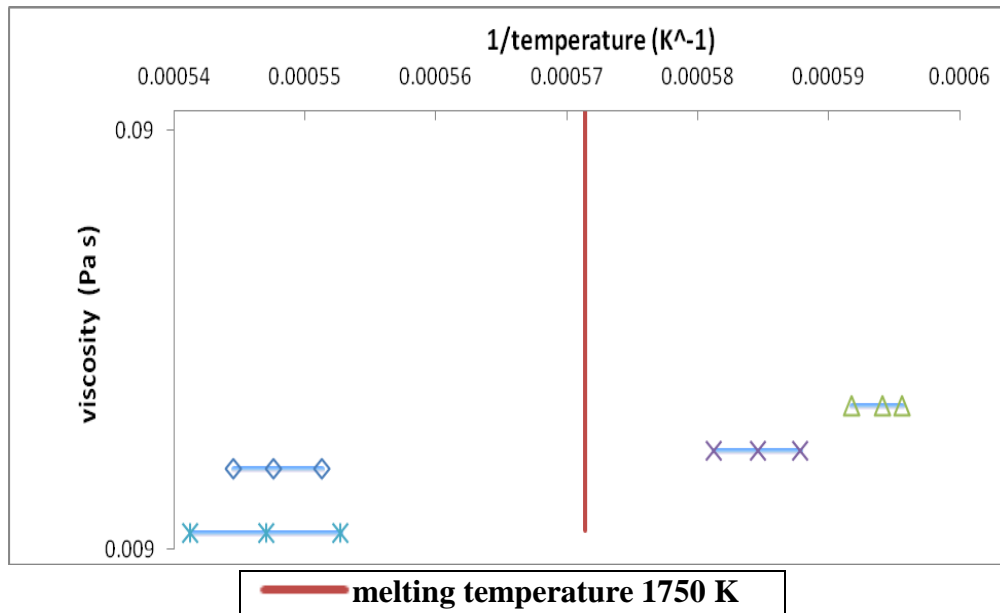


**Figure 40:** Figure showing the graph of the thermotransient viscosity vs. 1/temperature for the Fe(50%)-Co(50%) alloy.

## Discussion

### Data analysis and relation to theory

Evaporation coefficient equation to be used (obtained through linearly fitting the evaporation coefficient values with respect to temperature):

$$\alpha = 0.000918 * T - 0.717$$

We use our evaporation coefficient equation in our composition analysis for our Fe(50%)-Co(50%) and Fe(45%)-Co(45%) samples which we have performed density and viscosity tests on. Namely, we use the generated, temperature-dependent values for the evaporation coefficient  $\alpha$ , in order to calculate the evaporation flux using the following equation [32, 34, 35]:

$$J = \frac{\alpha P_v}{\sqrt{2\pi MRT}}$$

Therefore, as explained in the background section, the compositions and masses for each metal component (iron and cobalt) of the alloy at each time interval can be calculated, and we end up with the ratio of the predicted total final mass to the actual total final mass to be practically equal to unity. We then utilized the proper masses in performing the calculations of the densities, viscosities and surface tensions.

We were able to generate the following liquid region density-temperature graph for one of the density tests performed on a Fe(45%)-Co(55%) sample (Figure 41):

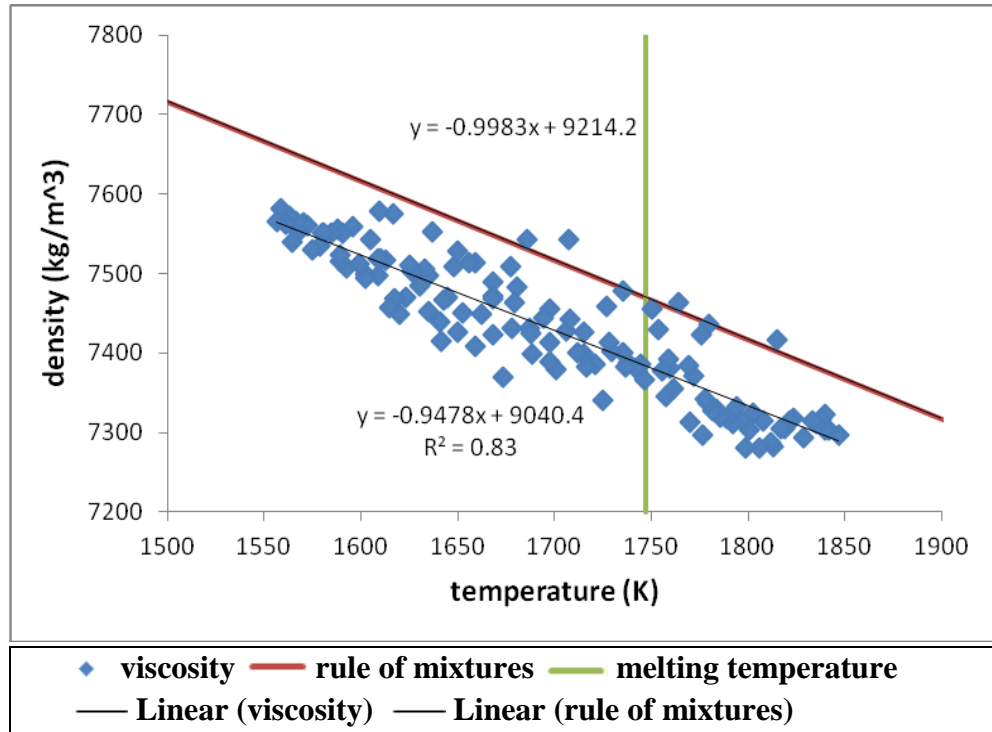


**Figure 41: Figure showing the liquid section graph of density vs. temperature for the Fe(45%)-Co(55%) alloy sample.**

**Table 12: Table showing the experimental and predicted values of the slope and density at the melting temperature for the liquid section density graph of the Fe(45%)-Co(55%) alloy sample.**

Experimental density at melting temperature (kg/m³)	7384.59
Predicted density at melting temperature (kg/m³)	7470.17
Percentage difference between densities	1.15%
Experimental slope (kg/(K m³))	-0.9478
Predicted slope (kg/(K m³))	-0.9983
Percentage difference between slopes	5.06%

As we see in Figure 41 and Table 12, we got a very good approximation of the liquid density-temperature relationship for this alloy concentration – the graph we obtained is very close to the ideal graph which is generated through the rule of

mixtures. This fact is represented by a very small percentage difference, 1.15%, between the densities at the melting temperature, 1474 °C (1747 K). Another statistic which confirms the quality and extreme accuracy of our graph is the percentage difference between the slope of the graph we got and that of the rule of mixtures. It is 5.06%, a very low percentage error.

We were also able to generate the following density-temperature graph for one of the density tests performed on a Fe(50%)-Co(50%) sample (Figure 42):

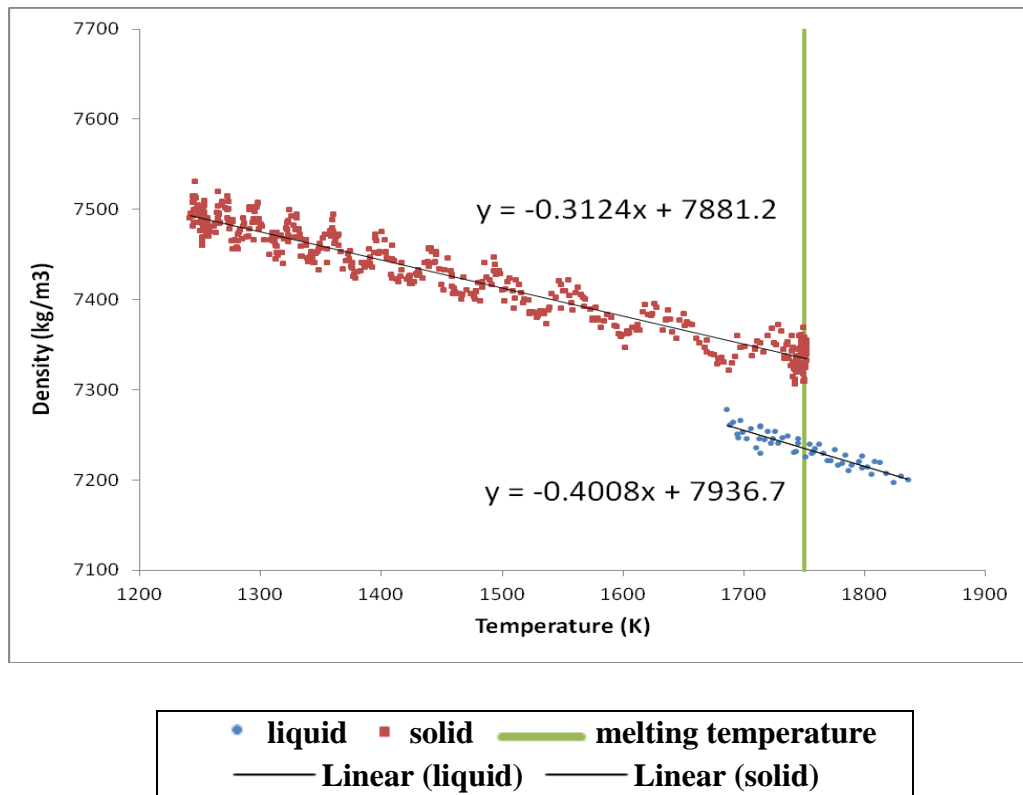


**Figure 42: Figure showing the liquid and solid sections of the graph of density vs. temperature for the Fe(50%)-Co(50%) alloy sample.**

**Table 13: Table showing the experimental and predicted values of the slopes and densities at the melting temperature, for both the solid and liquid sections of the density graph for the Fe(50%)-Co(50%) alloy sample.**

Experimental density at melting temperature (kg/m <sup>3</sup> )	7235.30
Predicted density at melting temperature (kg/m <sup>3</sup> )	7433.11
Percentage difference between densities	2.66%
Experimental slope (kg/(K m <sup>3</sup> ))	-0.4008
Predicted slope (kg/(K m <sup>3</sup> ))	-0.9878
Percentage difference between slopes	59.42%
Experimental solid slope (kg/(K m <sup>3</sup> ))	-0.3124
Experimental solid density at melting temperature (kg/m <sup>3</sup> )	7334.50

As we see, in comparing the liquid densities at the melting temperature, 1477 °C (1750 K), the percentage difference between the experimental liquid density we obtained and density obtained through the rule of mixtures is a mere 2.66%. This is proof of the accuracy of our graph, its quality shown by the mathematical precision we see among both sections of points, namely the two sections of points representing the liquid and solid regions under study in the thermal cycle. The difference in the slope between the solid and liquid sections does not hinder the validity or the quality of the graph, since the most important characteristic is the density at the melting point. The issue of the big difference in slope is of secondary importance to the density of the melting temperature. In addition, the slope is a value which would easily change between several density test runs, since each singular point on the graph would have a significant impact on the slope value itself. This increases the level of subjectivity in the slope value.

Therefore, obtaining a slope of the liquid section of the experimental density-temperature plot that is close to the rule-of-mixtures-generated slope of the corresponding graph is a luxury, not a necessity. The linearly decreasing density-temperature relationships obtained are harmonious with those that Shunroku Watanabe obtained for different elemental compositions for the Fe-Co alloy in liquid state [17].

The linear relationship Watanabe obtained for Fe(60%)-Co(40%) is the following:

$$\rho(g/cm^3) = 9.44 - 0.00115 * T(K)$$

The linear relationship Watanabe obtained for Fe(40%)-Co(60%) is the following:

$$\rho(g/cm^3) = 9.58 - 0.00113 * T(K)$$

The following table shows the densities obtained at the melting temperatures for the different alloy compositions of molten Fe-Co, based on Watanabe's density-temperature relations. The precision figures shown with the densities are calculated with 95% confidence. We used the method of linear interpolation to generate the densities for Fe(45%)-Co(55%) and Fe(50%)-Co(50%), as shown in Table 14:

**Table 14: Table showing the density values and errors for each composition at the given melting temperature, based on Watanabe's density-temperature relations.**

Composition	Melting Temperature (K)	Density (kg/m <sup>3</sup> )	% Error
Fe(60%)-Co(40%)	1755	7435.16 ± 70.43	1.03 %
Fe(40%)-Co(60%)	1746	7606.79 ± 79.38	1.35 %
Fe(45%)-Co(55%)	1747	7563.88 ± 77.14	1.25 %
Fe(50%)-Co(50%)	1750	7520.97 ± 74.91	1.18 %

Based on the density measurements performed by J. Brillo et al. (2006), the linear density-temperature relationship obtained for liquid Fe(50%)-Co(50%) is the following [36]:

$$\begin{aligned}\rho(g/cm^3) &= 7.43 - 0.000748 * (T(^{\circ}C) - 1479) \\ &= 8.54 - 0.000748 * T(^{\circ}C)\end{aligned}$$

The density at the melting point, 1477 °C (1750 K), with 95% confidence, is (7431.50 ± 18.69) kg/m<sup>3</sup>, and carries a 0.02% error with the predicted value.

With respect to the density measurements on our samples, we obtained the following densities for both Fe-Co concentrations, with 95% confidence:

$$\rho(\text{Fe(45\%)-Co(55\%)}) = (7384.59 \pm 72.48) \text{ kg/m}^3$$

$$\rho(\text{Fe(50\%)-Co(50\%)}) = (7235.32 \pm 15.34) \text{ kg/m}^3$$

Based on the above density measurements, we conclude that the accuracy is high for all measurements. The densities obtained using the containerless processes for Brillo's measurements and ours, as well as using the contact process for Watanabe's measurements were accurate, yet the results show that the precisions obtained through the containerless processes surpass those of the contact process density measurements.

We notice how the solid section of the density-temperature graph for Fe(50%)-Co(50%) is wavy in its appearance due to the fact that upon solidification, the solid sample does not have a spherical shape. In its liquid form, the sample undergoes vibration and rotation in its suspended position in the ESL, specified by the electrostatic forces and its weight. When it freezes, the sample's previous orientation and structure reflects in its current solid state, which causes the wavy pattern of the sample's solid section, as well as the larger-than-liquid-section disparity and scatter in the solid section's points.

Moreover, the obtained value for the solid density at the melting temperature is biased. This is because the nature of the solidification process is such that solidification begins at the surface of the sample. Due to the present solid-liquid phase gradient at that point, there is a contraction in the sample, due to a certain pull by the solid surface on the liquid depths of the sample. This happens because the solidified surface has a smaller volume than the liquid inner part of the sample, and because the solid phase is stronger than the liquid phase, the pull occurs in the outward direction from the sample's center. Therefore, this process leaves a cavity in the center of the sample in its wake, a vacuum which is



generated by the physical process of solidification which begins at the surface and continues inwards towards the center. Due to the fact that this solidification process is opposite to the traditional case of freezing where you have nucleation starting from the center of the droplet, our value of the solid density of the sample at the melting point is subjective.

The following graph (Figure 43) obtained is that of the isothermal surface tension for the Fe(45%)-Co(55%) alloy concentration:

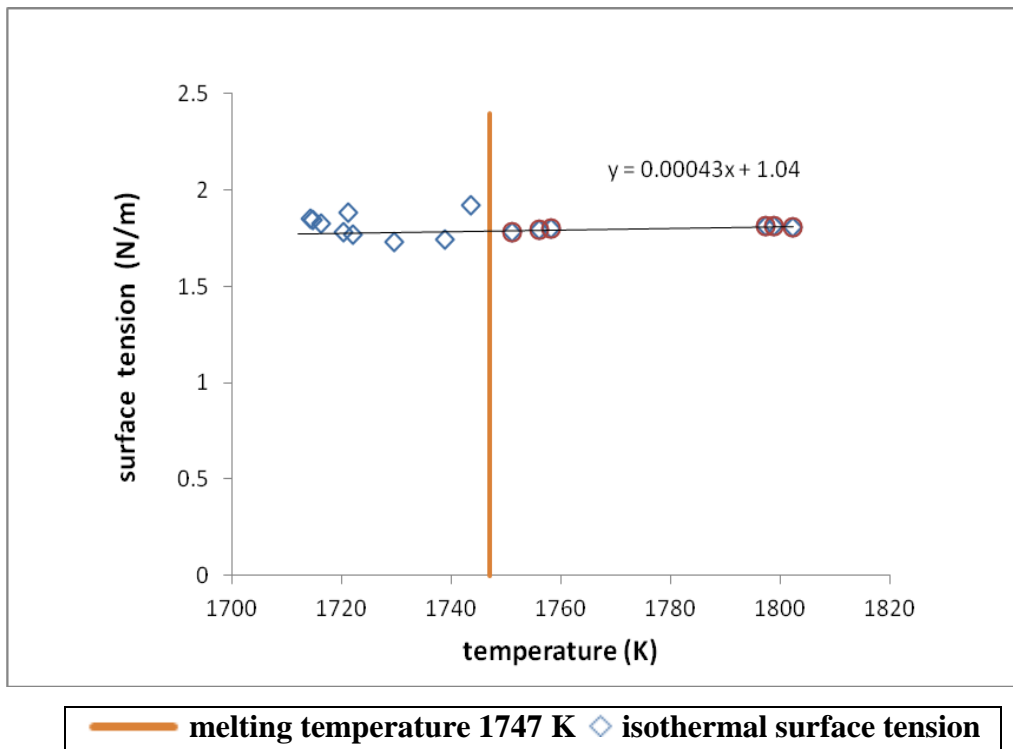


**Figure 43: Figure showing the graph of isothermal surface tension vs. temperature for the Fe(45%)-Co(55%) alloy.**

The following graph (Figure 44) obtained is that of the isothermal surface tension for the Fe(50%)-Co(50%) alloy concentration:

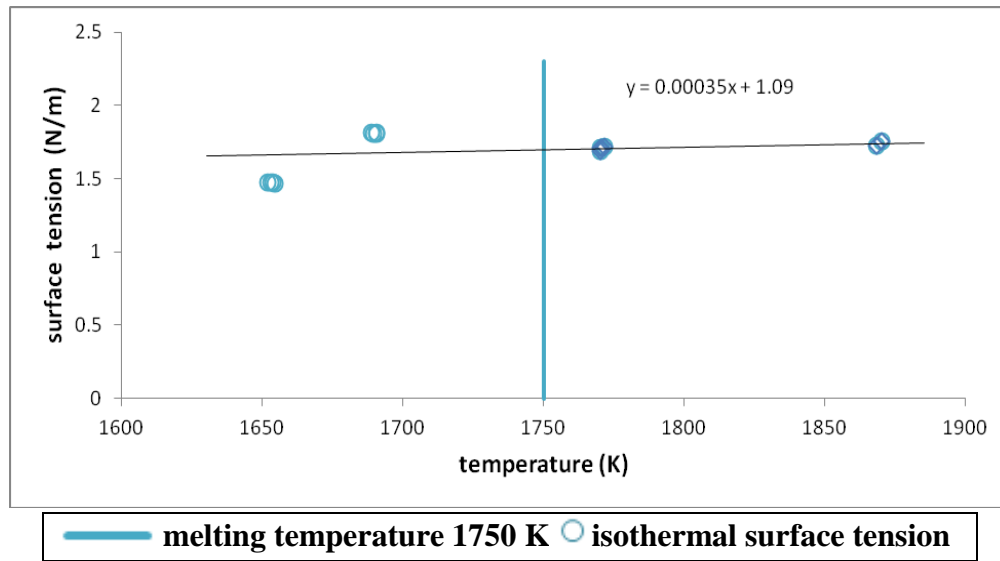


**Figure 44: Figure showing the graph of isothermal surface tension vs. temperature for the Fe(50%)-Co(50%) alloy.**

With respect to the surface tension graphs, we see that the curves are practically horizontal at temperatures greater than the melting temperature (and even at temperatures up to 60 K below the melting temperature). The surface tension at the melting temperature for Fe(50%)-Co(50%) is approximately 1.70 N/m, while that of Fe(45%)-Co(55%) is approximately 1.79 N/m.

We calculated the values by accounting for a linear fit in the surface tension points greater than the melting temperature. Performing linear fits on these points for each alloy concentration, we get the equations which represent practically horizontal lines, as expected.

For  $T > 1750$  K,

Fe(50%)-Co(50%) surface tension equation:

$$\gamma = 0.00035 * T + 1.09$$

The surface tension at 1750 K equals

$$\gamma = 0.00035 * 1750 + 1.09 = 1.70 \text{ N/m}$$

For  $T > 1747 \text{ K}$ ,

Fe(45%)-Co(55%) surface tension equation:

$$\gamma = 0.00043 * T + 1.04$$

The surface tension at 1747 K equals

$$\gamma = 0.00043 * 1747 + 1.04 = 1.79 \text{ N/m}$$

Therefore, from our horizontal surface tension-temperature graphs, we state that our surface tension values at temperatures greater than the melting temperature are constant, equal to 1.70 N/m for Fe(50%)-Co(50%) and 1.79 N/m for Fe(45%)-Co(55%).

Based on the Fe-Co surface tension plot obtained by Egry and Eichel, shown in Figure 15, it can be estimated that the surface tension at the liquidus temperature (1530 °C) is 1830 mN/m (1.830 N/m) and 1815 mN/m (1.815 N/m) for Fe(45%)-Co(55%) and Fe(50%)-Co(50%), respectively.

Based on our surface tension equations, we calculate our surface tension values at 1530 °C (1803 K).

For Fe(45%)-Co(55%), we have:

$$\gamma = 0.00043 * 1803 + 1.04 = 1.81 \text{ N / m}$$

For Fe(50%)-Co(50%), we have:

$$\gamma = 0.00035 * 1803 + 1.09 = 1.72 \text{ N / m}$$

The percentage errors of our surface tension measurements with respect to those of Egry and Eichel's corresponding surface tension values are 0.98% for Fe(45%)-Co(55%) and 5.38% for Fe(50%)-Co(50%). These low percentage errors are reflections of the accuracy and precision of both sets of surface tension values, and vindicate the use of the oscillating drop technique as the containerless process to measure surface tension.

Based on our conclusion that surface tension is constant with temperature, from

the equation  $\gamma = \frac{3\pi m f_l^2}{l(l-1)(l-2)}$ , we derive that the natural frequency of surface

oscillations,  $f_l$ , is constant with varying temperature. Therefore, this validates our use of the ESL Area Processor Labview program, since we end up with a fitted plot from which we have one final oscillation frequency throughout the oscillations in the cycle under study.

For each concentration, we plotted the isothermal and thermotransient viscosity data on one graph (Figures 45 and 46 for Fe(45%)-Co(55%) and Fe(50%)-

Co(50%) respectively). Simultaneously, we plotted the upper and lower limits of the isothermal viscosities, as shown in Figures 45 and 46:

Fe(45%)-Co(55%):

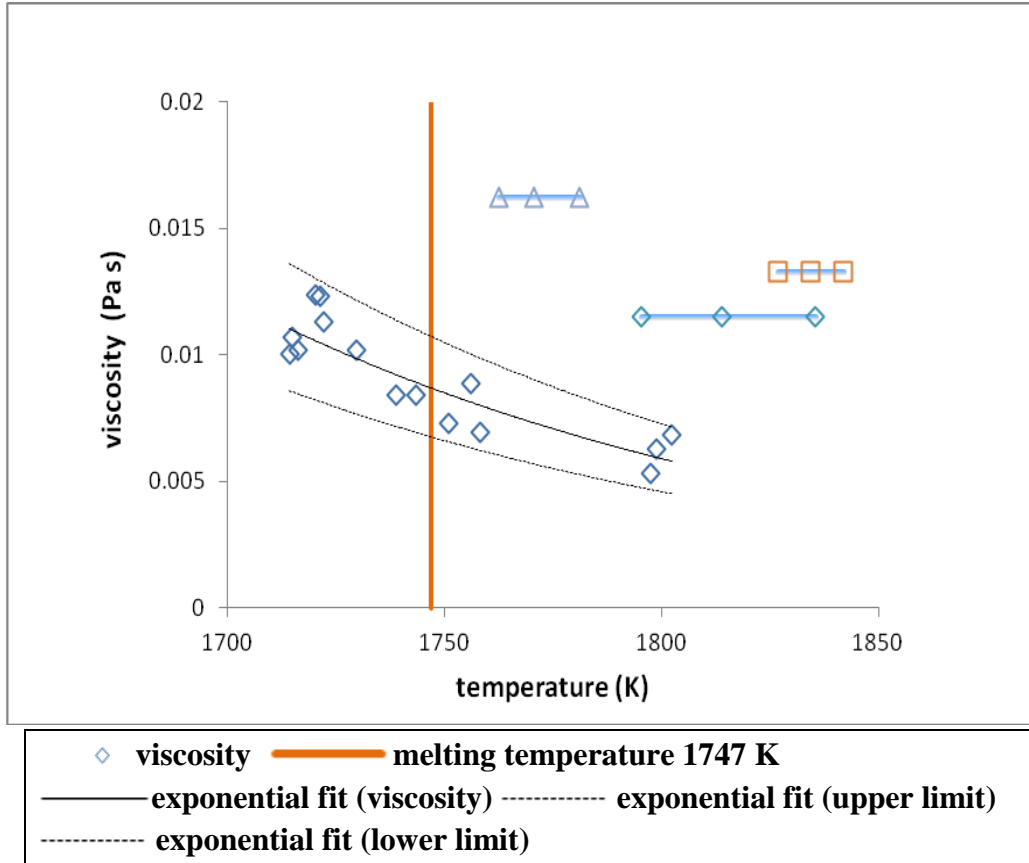


**Figure 45:** Figure showing the isothermal and thermotransient viscosities vs. temperature for the Fe(45%)-Co(55%) alloy composition, as well as the upper and lower limits of the isothermal viscosity points.

Fe(50%)-Co(50%):

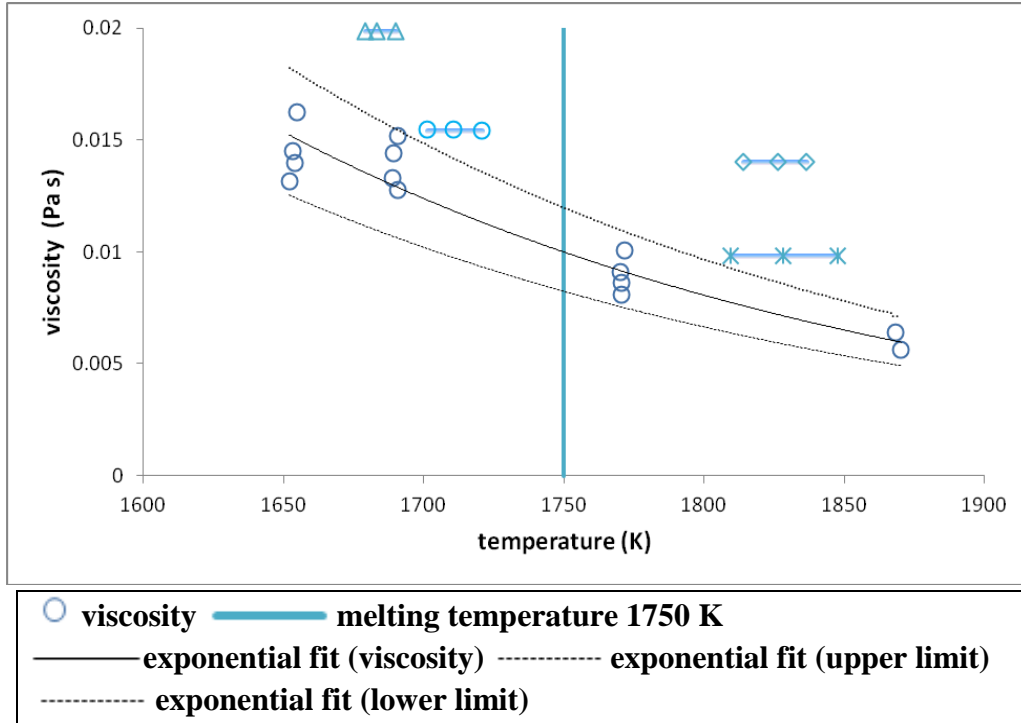


**Figure 46: Figure showing the isothermal and thermotransient viscosities vs. temperature for the Fe(50%)-Co(50%) alloy composition, as well as the upper and lower limits of the isothermal viscosity points.**

As we can see from each plot, the thermotransient viscosity points are not within a reasonable range specified by the isothermal viscosity points. Therefore, following our motivation for these experiments, we conclude, with 95% confidence, that isothermal viscosity testing will be required at the ISS. Namely, viscosity testing which involves the inconvenient thermal hold on the sample in question will be pursued (despite the inconvenience caused in terms of sample composition change and facility contamination), in addition to viscosity measurements based on tests down a temperature gradient. Both sets of tests will

be required to determine the viscosity-temperature graphs and the viscosity values at the melting point for each Fe-Co concentration.

We determined that our viscosity-temperature relations for liquid Fe-Co (Fe(45%)-Co(55%) and Fe(50%)-Co(50%)) at high temperatures followed an Arrhenius relation. Previous results obtained for different metal alloys at high temperatures also followed an Arrhenius relation.

For Fe(45%)-Co(55%), we have the following (Figure 47):

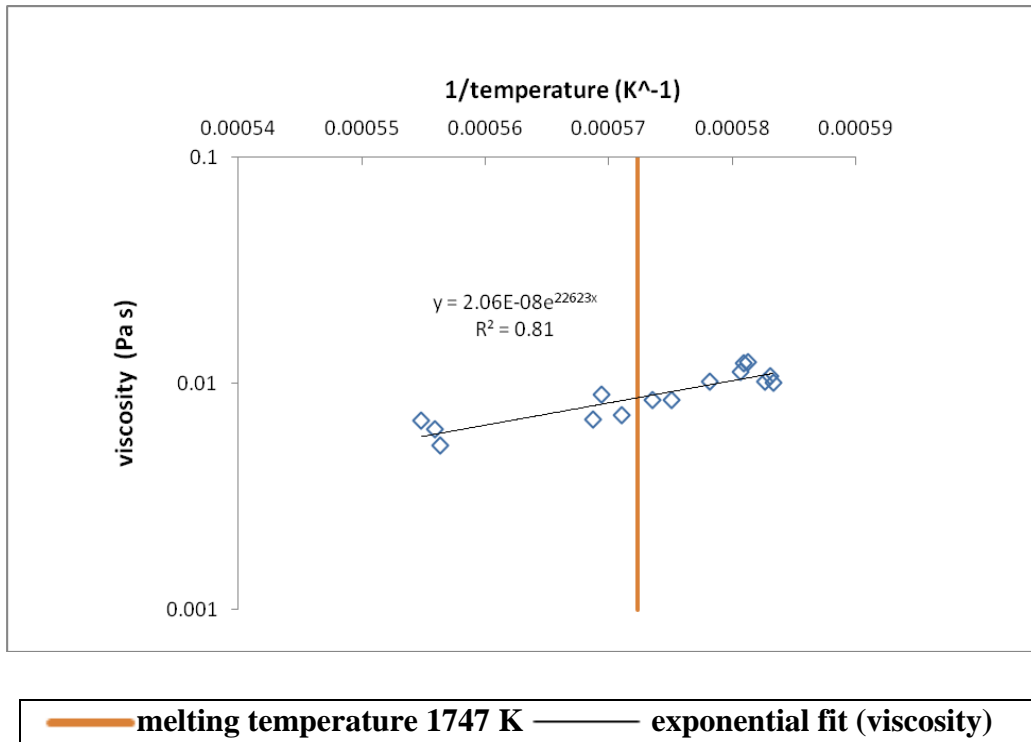


**Figure 47: Figure showing the Arrhenius relation between the isothermal viscosity and temperature on the viscosity-1/temperature graph for the Fe(45%)-Co(55%) alloy concentration.**

As we see, there is a strong Arrhenius relation between the viscosity and temperature. The equation depicting the relationship is

$$\mu = 2.06E-08 * \exp(22623/T)$$

For Fe(50%)-Co(50%), we have the following (Figure 48):

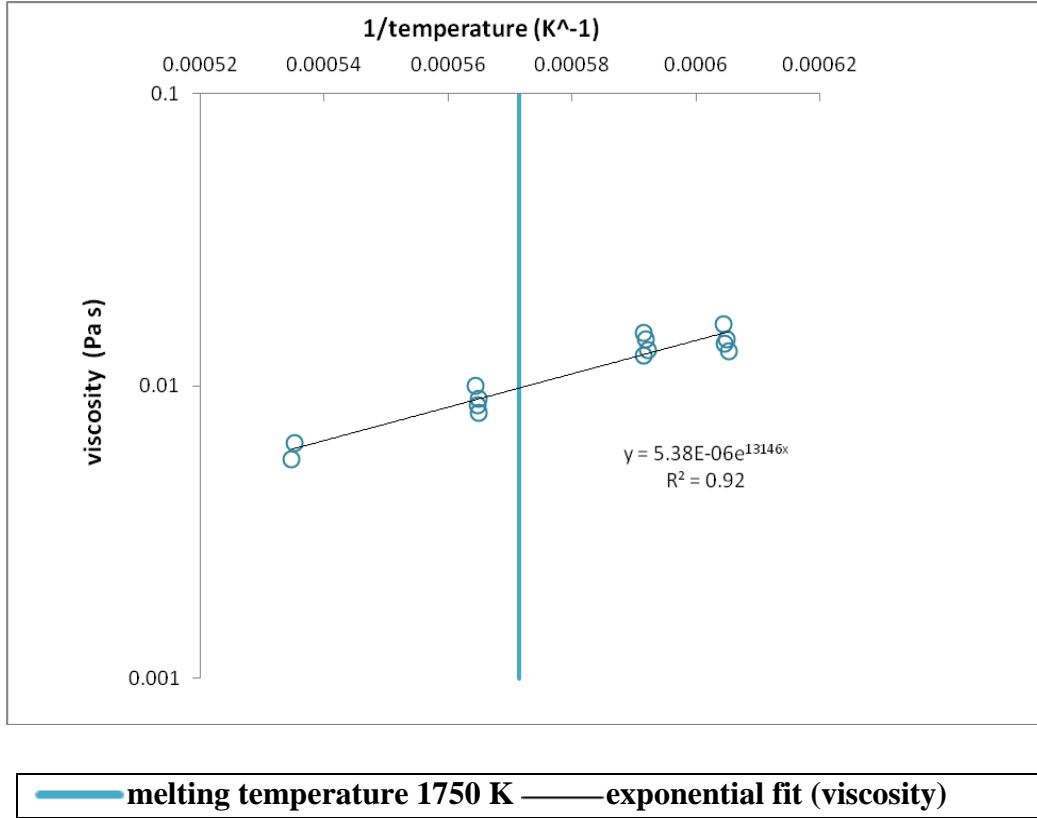


**Figure 48:** Figure showing the Arrhenius relation between the isothermal viscosity and temperature on the viscosity-1/temperature graph for the Fe(50%)-Co(50%) alloy concentration.

As we see, there is a strong Arrhenius relation between the viscosity and temperature. The equation depicting the relationship is

$$\mu = 5.38E-06 * \exp(13146/T)$$



**Table 15: Table showing the values of A (the pre-exponential factor) and Q (the activation energy) as well as their error bars for each composition.**

Composition	Fe(45%)-Co(55%)	Fe(50%)-Co(50%)
A	2.06E-08 Pa s	5.38E-06 Pa s
Q	-188 x 10 <sup>3</sup> J	-109 x 10 <sup>3</sup> J
Error bars for A (95% confidence)	A=(2.06E-8 + 0.56E-8) Pa s A=(2.06E-8 - 0.41E-8) Pa s	A=(5.38E-6 + 0.98E-6) Pa s A=(5.38E-6 - 1.00E-6) Pa s
Error bars for Q (95% confidence)	Q = (-188 x 10 <sup>3</sup> ± 54 x 10 <sup>3</sup> ) J	Q = (-109 x 10 <sup>3</sup> ± 20 x 10 <sup>3</sup> ) J

Calculating the viscosities at the melting point from our fitted equations we obtain the following:

- At the melting point (1747 K) of Fe(45%)-Co(55%), the viscosity value equals  $2.06\text{E-}08 \cdot \exp(22623/1747) = 0.00865 \text{ Pa s}$ .
- The Fe(45%)-Co(55%) melting point viscosity, accounting for error with 95% confidence, is  $0.00865 + 0.00203/-0.00192 \text{ Pa s}$ .
- At the melting point (1750 K) of Fe(50%)-Co(50%), the viscosity value equals  $5.38\text{E-}06 \cdot \exp(13146/1750) = 0.00985 \text{ Pa s}$ .
- The Fe(50%)-Co(50%) melting point viscosity, accounting for error with 95% confidence, is  $0.00985 + 0.00194/-0.00174 \text{ Pa s}$ .

According to the viscosity-temperature graphical and mathematical relation which was determined by Watanabe for liquid Fe-Co in 1971, the viscosity of Fe(50%)-

Co(50%) measured at the melting point (1750 K) is approximately 5.02 centipoise, or 0.00502 Pa s [17]. Our viscosity value for Fe(50%)-Co(50%) at the melting point is almost double that of Watanabe's viscosity value, prompting a 96% percentage error. Watanabe's viscosity at 1750 K, accounting for error with 95% confidence, is  $0.00502 \pm 0.00021$  Pa s.

Likewise, for the Fe(50%)-Co(50%) alloy viscosity measured by Watanabe, the pre-exponential factor A and activation energy Q equal  $(3.0\text{E-}4 \pm 0.1\text{E-}4)$  Pa s and  $(41 \times 10^3 \pm 3 \times 10^3)$  J, respectively.

Our Fe(50%)-Co(50%) viscosity value at the melting point was almost double that of Watanabe's. We cannot be certain of the reason for this large disparity between both sets of viscosity values and precision errors, although we can say that the processes used to generate the viscosities were markedly different: Watanabe's oscillating crucible method was a contact method which was used to measure viscosities in 1970; our viscosities, measured in 2011, were determined using the containerless process that is the oscillating drop method.

In addition, we notice that in each plot of the thermotransient viscosities with respect to temperature, the high-viscosity points reflect a short damping time and therefore a short temperature range. Physically, the more viscous sample will understandably have a smaller damping capability due to an applied deformation; therefore the time for the damping process will be less. For the lower-viscosity points, there is a higher temperature range due to a larger damping time.

Physically, this can be understood in that the less viscous sample will be more

fluid, and therefore will have a larger damping capacity and hence a longer damping process. A larger time span will correspond to a larger temperature range through which the damping will occur due to the deformation applied on the sample in question.

### **Error Analysis**

We performed a t-test to study if there is a strong linear relationship between the evaporation coefficient and the temperature.

The data shown in Table 16 was used in this analysis:

**Table 16: Table showing the t-test setup on the relation between the evaporation coefficient and temperature, showing the deviations from the linear fit and constant at average as the two sets of data to be analyzed in the final reckoning.**

Evaporation coefficient	Temperature in K	Linear fit	Deviation from linear fit	Deviation from constant at average
0.8997	1771.31	0.9088	-0.0092	-0.0072
0.8249	1678.94	0.8240	0.0009	-0.0819
0.9560	1754.63	0.8935	0.0624	0.0491
0.9823	1842.51	0.9742	0.0081	0.0755
0.8350	1766.52	0.9044	-0.0694	-0.0718
0.9431	1800.85	0.9359	0.0071	0.0362

We perform the t-test on the deviation from the linear fit and the deviation from the constant average (Table 17):

**Table 17: Table showing the t-test which accounts for the deviations from the linear fit and the constant at average.**

	Deviation from linear fit	Deviation from constant at average
	-0.0092	-0.0072
	0.0009	-0.0819
	0.0624	0.0491
	0.0081	0.0755
	-0.0694	-0.0718
	0.0071	0.0362
Average	-4.272E-07	-1.110E-16
N	6	6
Variance (var)	0.0018	0.0043
Standard Deviation	0.0422	0.0653

For our t-tests, we used the relevant critical values in Table 18 [38]:

**Table 18: Table showing the t-test critical values for different confidence probability levels (90%, 95%, 99%, 99.9%) for each given degree of freedom.**

Degrees of Freedom	Probability, p			
	0.1	0.05	0.01	0.001
1	6.314	12.706	63.657	636.619
2	2.920	4.303	9.925	31.598
3	2.353	3.182	5.841	12.941
4	2.132	2.776	4.604	8.610
5	2.015	2.571	4.032	6.859
6	1.943	2.447	3.707	5.959
7	1.895	2.365	3.499	5.405
8	1.860	2.306	3.355	5.041
9	1.833	2.262	3.250	4.781
10	1.812	2.228	3.169	4.587
11	1.796	2.201	3.106	4.437

12	1.782	2.179	3.055	4.318
13	1.771	2.160	3.012	4.221
14	1.761	2.145	2.977	4.140
15	1.753	2.131	2.947	4.073
16	1.746	2.120	2.921	4.015
17	1.740	2.110	2.898	3.965
18	1.734	2.101	2.878	3.922
19	1.729	2.093	2.861	3.883
20	1.725	2.086	2.845	3.850
21	1.721	2.080	2.831	3.819
22	1.717	2.074	2.819	3.792
23	1.714	2.069	2.807	3.767
24	1.711	2.064	2.797	3.745
25	1.708	2.060	2.787	3.725
26	1.706	2.056	2.779	3.707
27	1.703	2.052	2.771	3.690
28	1.701	2.048	2.763	3.674
29	1.699	2.045	2.756	3.659
30	1.697	2.042	2.750	3.646
40	1.684	2.021	2.704	3.551
60	1.671	2.000	2.660	3.460
120	1.658	1.980	2.617	3.373
infinity	1.645	1.960	2.576	3.291

We calculate the value of  $t$ , using the following equation:

$$t = \frac{|average_1 - average_2|}{\sqrt{\frac{var_1^2}{N_1} + \frac{var_2^2}{N_2}}} = 0.000226$$

$$Degrees\ of\ freedom = N_1 + N_2 - 2 = 6 + 6 - 2 = 10$$

Using Table 18:

For the degrees of freedom being 10, we have the threshold value equal to 1.812.

Since  $t_{statistic} = 0.000226 < t_{critical} = 1.812$ , we accept/retain the null hypothesis.

The null hypothesis states that there is statistically no difference between the two sets of data. It states that the two sets of data are from the same population; the mean of one group equals the mean of the second group.

Since the null hypothesis is accepted, we conclude that there is statistically no significant difference between the two sets of values.

Therefore, we use the  $R^2$  and variance values as means to determine if the evaporation coefficient should be a constant at the average or a linear function of temperature.

For the linear fit of the evaporation coefficients,  $R^2$  is equal to 0.582. For the horizontal fit of the constant at the coefficient average,  $R^2$  is equal to 0. Therefore, mathematically, the linear fit of the evaporation coefficient is stronger.

Additionally, the variance of the deviations from the linear fit is approximately 0.0018 and the variance of deviations from the constant at average is 0.0043.

Since a variance is a measure of the scatter of the points, a smaller variance in the case of the linear fit deviations shows that a linear relationship between the evaporation coefficient and temperature is stronger and more precise than a horizontal fit at the coefficient average, in the case where the evaporation coefficient is independent of temperature.

Hence, we can account for a linear relationship between the evaporation coefficient and temperature. That is why, in conclusion, we use a linear equation for the evaporation coefficient in our forthcoming calculations, namely the

equation of the line used to fit the evaporation coefficients obtained from our analysis of the samples sent to Luvak Inc. for composition analysis.

Evaporation coefficient equation used:

$$\alpha = 0.000918 * T - 0.717$$

The standard error for the evaporation coefficient equals 0.047.

With 95% confidence (certainty), we can say that the evaporation coefficient  $\alpha$  can be written as:

$$\alpha = 0.907 \pm 2.776 \times 0.047 = 0.907 \pm 0.131$$

The slope can be written as:

$$0.000918 \pm 0.001080$$

The intercept can be written as:

$$-0.717 \pm 1.911$$

The following table illustrates the percentage difference between the densities at the melting point for liquid Fe-Co (Table 19):

**Table 19: Table showing the experimental and predicted densities of both given alloy compositions in the liquid state.**

Alloy Composition	Fe(45%)-Co(55%)	Fe(50%)-Co(50%)
Experimental density at melting temperature (kg/m <sup>3</sup> )	7384.59	7235.30
Predicted density at melting temperature (kg/m <sup>3</sup> )	7470.17	7433.11
Percentage difference between densities	1.15%	2.66%

For Fe(45%)-Co(55%), we have the following (Tables 20 and 21):

**Table 20: Table showing the numerical results when generating the upper and lower limits of the isothermal viscosities for Fe(45%)-Co(55%).**

Isothermal viscosities (Pa s)	Exponential fit values (Pa s)	Difference (Pa s)	Difference /Fit	1+D/F	Upper limit	Lower limit
0.0107	0.0110	-0.0003	-0.024	0.976	0.0135	0.0085
0.0102	0.0109	-0.0006	-0.060	0.940	0.0134	0.0084
0.0100	0.0110	-0.0010	-0.091	0.909	0.0136	0.0086
0.0068	0.0058	0.0010	0.177	1.177	0.0071	0.0045
0.0053	0.0060	-0.0007	-0.115	0.885	0.0074	0.0047
0.0063	0.0059	0.0003	0.055	1.055	0.0073	0.0046
0.0070	0.0080	-0.0011	-0.131	0.869	0.0099	0.0062
0.0089	0.0081	0.0007	0.092	1.092	0.0100	0.0063
0.0073	0.0084	-0.0012	-0.137	0.863	0.0104	0.0066
0.0084	0.0089	-0.0005	-0.056	0.944	0.0110	0.0069
0.0113	0.0104	0.0009	0.084	1.084	0.0129	0.0081
0.0123	0.0105	0.0018	0.174	1.174	0.0129	0.0082
0.0124	0.0106	0.0018	0.171	1.171	0.0130	0.0082
0.0102	0.0099	0.0003	0.035	1.035	0.0122	0.0077
0.0084	0.0092	-0.0008	-0.086	0.914	0.0114	0.0072



**Table 21: Table showing the average of the  $(1+(\text{fit deviation}/\text{fit}))$  values in Table 20 as well as the standard deviation, and upper and lower coefficients.**

Average	Standard deviation	Upper coefficient	Lower coefficient
1.006	0.114	1.234	0.778

The upper and lower limits in Table 20 are obtained by multiplying the upper and lower coefficients in Table 21 by the exponential fit values in Table 20. The upper and lower limits are plotted (Figure 45) to establish the isothermal viscosity limits in order to compare them with the thermotransient viscosity values.

For Fe(50%)-Co(50%), we have the following (Tables 22 and 23):

**Table 22: Table showing the numerical results when generating the upper and lower limits of the isothermal viscosities for Fe(50%)-Co(50%).**

Isothermal viscosities (Pa s)	Exponential fit values (Pa s)	Difference (Pa s)	Difference /Fit	1+D/F	Upper limit	Lower limit
0.0100	0.0091	0.0009	0.103	1.103	0.0109	0.0075
0.0086	0.0091	-0.0005	-0.060	0.940	0.0110	0.0075
0.0091	0.0092	-0.0001	-0.009	0.991	0.0110	0.0075
0.0081	0.0092	-0.0011	-0.116	0.884	0.0110	0.0075
0.0144	0.0130	0.0014	0.112	1.112	0.0155	0.0107
0.0151	0.0129	0.0023	0.178	1.178	0.0154	0.0106
0.0128	0.0129	-0.0001	-0.010	0.990	0.0154	0.0106
0.0133	0.0130	0.0003	0.022	1.022	0.0156	0.0107
0.0140	0.0151	-0.0011	-0.074	0.926	0.0181	0.0124
0.0145	0.0151	-0.0006	-0.042	0.958	0.0181	0.0125
0.0132	0.0152	-0.0021	-0.135	0.865	0.0182	0.0125
0.0162	0.0150	0.0012	0.078	1.078	0.0180	0.0124
0.0056	0.0060	-0.0003	-0.056	0.944	0.0071	0.0049
0.0064	0.0060	0.0004	0.062	1.062	0.0072	0.0049

**Table 23: Table showing the average of the  $(1+(\text{fit deviation}/\text{fit}))$  values in Table 22 as well as the standard deviation, and upper and lower coefficients.**

Average	Standard deviation	Upper coefficient	Lower coefficient
1.011	0.093	1.197	0.824

The upper and lower limits in Table 22 are obtained by multiplying the upper and lower coefficients in Table 23 by the exponential fit values in Table 22. The upper and lower limits are plotted (Figure 46) to establish the isothermal viscosity limits in order to compare them with the thermotransient viscosity values.

The following analysis depicts the t-test which shows that the isothermal viscosities and thermotransient viscosities for Fe(45%)-Co(55%) are different:

**Table 24: The following table shows the isothermal viscosity information for Fe(45%)-Co(55%).**

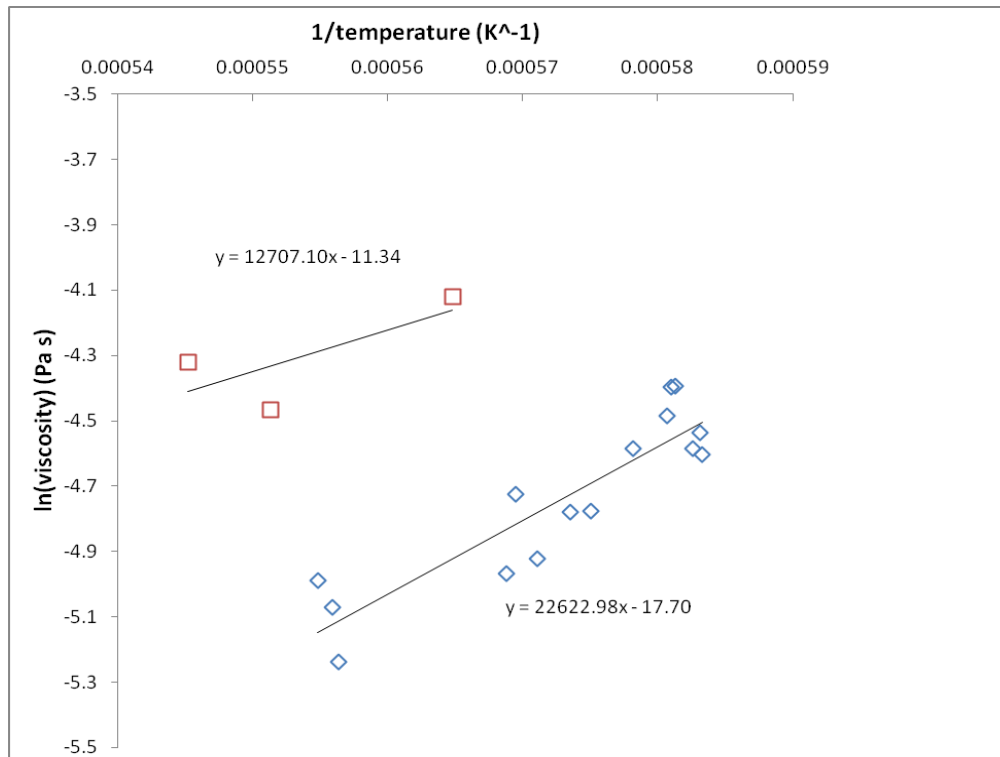
Isothermal viscosity points (Pa s)	Temperature (K)	$\ln(\text{viscosity})$ (Pa s)	$1/\text{Temperature (K}^{-1})$
0.0107	1714.91	-4.54	0.000583
0.0102	1716.37	-4.58	0.000583
0.0100	1714.32	-4.60	0.000583
0.0068	1802.39	-4.99	0.000555
0.0053	1797.46	-5.24	0.000556
0.0063	1798.88	-5.07	0.000556
0.0070	1758.17	-4.97	0.000569
0.0089	1756.03	-4.72	0.000569
0.0073	1751.09	-4.92	0.000571
0.0084	1743.54	-4.78	0.000574
0.0113	1722.15	-4.48	0.000581
0.0123	1721.25	-4.40	0.000581
0.0124	1720.33	-4.39	0.000581
0.0102	1729.58	-4.58	0.000578
0.0084	1738.92	-4.78	0.000575

**Table 25: The following table shows the thermotransient viscosity information for Fe(45%)-Co(55%).**

Thermotransient viscosity (Pa s)	Temperature (K)	ln(viscosity) (Pa s)	1/Temperature (K <sup>-1</sup> )
0.0115	1813.80	-4.47	0.000551
0.0133	1834.26	-4.32	0.000545
0.0162	1770.55	-4.12	0.000565

The thermotransient viscosities in the above table represent the midpoint viscosities of the thermotransient viscosity bars for Fe(45%)-Co(55%), the viscosities at the average temperatures of the respective temperature ranges corresponding to the damping time of the sample oscillations.

Figure 49 depicts the graph of the natural logarithm of the viscosity (Pa s) vs. 1/temperature (K<sup>-1</sup>):



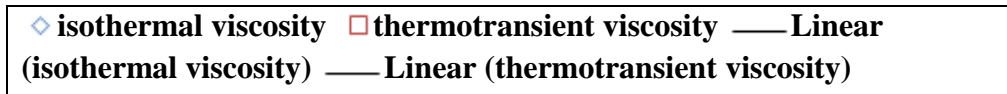


**Figure 49: Figure showing the plots of the natural logarithm for the Fe(45%)-Co(55%) isothermal and thermotransient viscosities vs. 1/temperature, as well as their linear fits and equations.**

From the above graph, we deduce that the linear fits for the isothermal and thermotransient viscosities are, respectively:

$$\ln(\mu_{isothermal}) = 22622.98 * (1/T) - 17.70$$

$$\ln(\mu_{thermotransient}) = 12707.10 * (1/T) - 11.34$$

We use the linear fits to generate isothermal and thermotransient viscosities for our t-test.

**Table 26: The following table shows the viscosity fitted values and t-test information for Fe(45%)-Co(55%).**

1/Temperature (K <sup>-1</sup> )	Ln(Isothermal viscosity) (Pa s)	Ln(Thermotransient viscosity) (Pa s)
0.00055	-5.257	-4.350
0.00056	-5.031	-4.223
0.00057	-4.805	-4.096
0.00058	-4.579	-3.969
0.00059	-4.352	-3.842
Average	-4.805	-4.096
N	5	5
Variance	0.128	0.040

We calculate the value of t, using the following equation:

$$t = \frac{|average_1 - average_2|}{\sqrt{\frac{var_1^2}{N_1} + \frac{var_2^2}{N_2}}} = 11.82$$

$$Degrees\ of\ freedom = N_1 + N_2 - 2 = 5 + 5 - 2 = 8$$

For the degrees of freedom being 8, we have the threshold value equal to 5.041.

Since  $t_{statistic} = 11.82 > t_{critical} = 5.041$ , we reject the null hypothesis.

The null hypothesis states that there is statistically no difference between the two sets of data. It states that the two sets of data are from the same population; the mean of one group equals the mean of the second group.

Since the null hypothesis is rejected, we conclude that there is statistically a significant difference between the two sets of values, with 99.9% certainty.

Therefore, there is no relation between both sets of values; we conclude that the isothermal and thermotransient viscosities for Fe(45%)-Co(55%) are different.

This serves to emphasize that the thermotransient viscosity values we have do not provide reasonable estimates for the viscosity values as required within aforementioned upper and lower limits of the isothermal viscosity values. This is further justification for requiring the thermal hold on the samples when performing viscosity tests at the ISS, in order to generate the isothermal viscosity values which are valid estimates for the viscosity of Fe(45%)-Co(55%).

The following analysis depicts the t-test which shows that the isothermal viscosities and thermotransient viscosities of Fe(50%)-Co(50%) are different:

**Table 27: The following table shows the isothermal viscosity information for Fe(50%)-Co(50%).**

Isothermal viscosity points (Pa s)	Temperature (K)	ln(viscosity) (Pa s)	1/Temperature (K <sup>-1</sup> )
0.0100	1771.61	-4.60	0.000564
0.0086	1770.60	-4.76	0.000565
0.0091	1770.16	-4.70	0.000565
0.0081	1770.30	-4.82	0.000565
0.0144	1689.41	-4.24	0.000592
0.0152	1690.70	-4.19	0.000591
0.0128	1690.68	-4.36	0.000591
0.0133	1688.83	-4.32	0.000592
0.0140	1653.86	-4.27	0.000605
0.0145	1653.24	-4.23	0.000605
0.0132	1652.13	-4.33	0.000605
0.0162	1654.67	-4.12	0.000604
0.0056	1870.12	-5.18	0.000535
0.0064	1868.33	-5.05	0.000535

**Table 28: The following table shows the thermotransient viscosity information for Fe(50%)-Co(50%).**

Thermotransient viscosity (Pa s)	Temperature (K)	ln(viscosity) (Pa s)	1/Temperature (K <sup>-1</sup> )
0.0140	1826.08	-4.27	0.000548
0.0199	1683.18	-3.92	0.000594
0.0154	1710.59	-4.17	0.000585
0.0098	1827.95	-4.62	0.000547

The thermotransient viscosities in the above table represent the midpoint viscosities of the thermotransient viscosity bars for Fe(50%)-Co(50%), the viscosities at the average temperatures of the respective temperature ranges corresponding to the damping time of the sample oscillations.

Figure 50 depicts the graph of the natural logarithm of the viscosity (Pa s) vs.  $1/\text{temperature (K}^{-1}\text{)}$ :

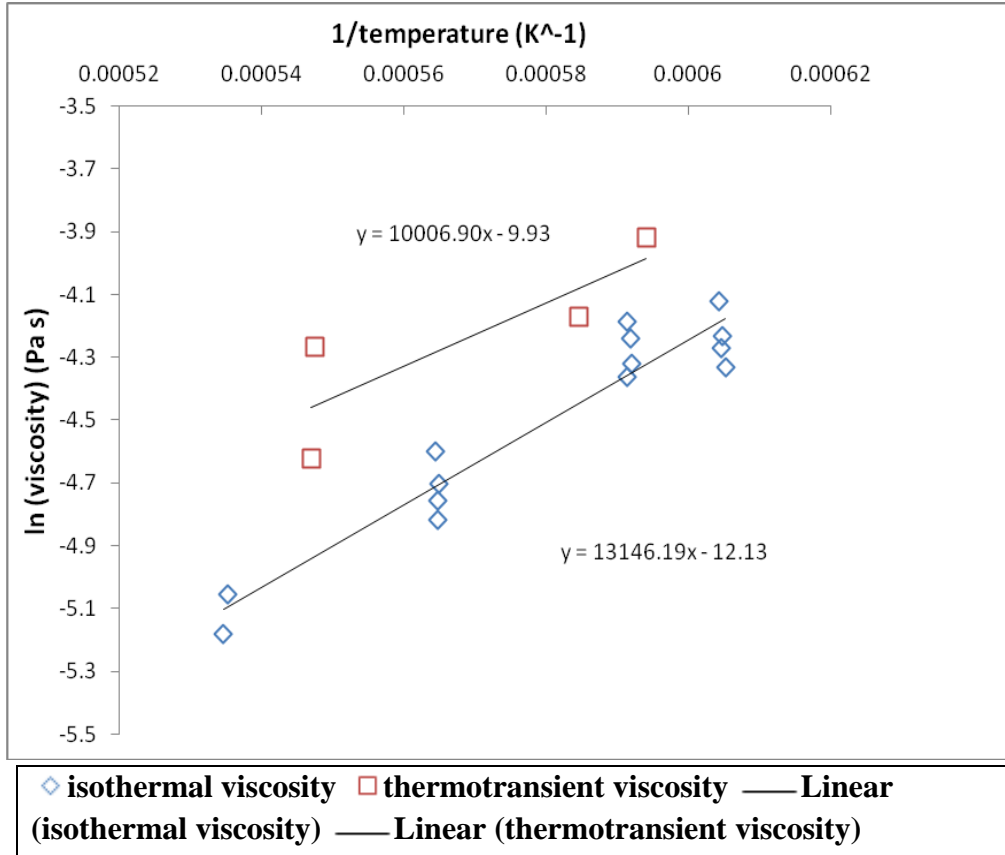


**Figure 50: Figure showing the plots of the natural logarithm for the Fe(50%)-Co(50%) isothermal and thermotransient viscosities vs.  $1/\text{temperature}$ , as well as their linear fits and equations.**

From the above graph, we deduce that the linear fits for the isothermal and thermotransient viscosities are, respectively:

$$\ln(\mu_{\text{isothermal}}) = 13146.19 * (1/T) - 12.13$$

$$\ln(\mu_{\text{thermotransient}}) = 10006.90 * (1/T) - 9.93$$

We use the linear fits to generate isothermal and thermotransient viscosities for our t-test:

**Table 29: The following table shows the viscosity fitted values and t-test information for Fe(50%)-Co(50%).**

1/Temperature (K <sup>-1</sup> )	Ln(Isothermal viscosity) (Pa s)	Ln(Thermotransient viscosity) (Pa s)
0.00055	-4.902	-4.429
0.00056	-4.771	-4.329
0.00057	-4.639	-4.229
0.00058	-4.508	-4.129
0.00059	-4.376	-4.028
Average	-4.639	-4.229
N	5	5
Variance	0.043	0.025

We calculate the value of t, using the following equation:

$$t = \frac{|average_1 - average_2|}{\sqrt{\frac{var_1^2}{N_1} + \frac{var_2^2}{N_2}}} = 18.39$$

$$Degrees\ of\ freedom = N_1 + N_2 - 2 = 5 + 5 - 2 = 8$$

For the degrees of freedom being 8, we have the threshold value equal to 5.041.

Since  $t_{statistic} = 18.39 > t_{critical} = 5.041$ , we reject the null hypothesis.

The null hypothesis states that there is statistically no difference between the two sets of data. It states that the two sets of data are from the same population; the mean of one group equals the mean of the second group.

Since the null hypothesis is rejected, we conclude that there is statistically a significant difference between the two sets of values, with a 99.9% certainty.

Therefore, there is no relation between both sets of values; we conclude that the



isothermal and thermotransient viscosities for Fe(50%)-Co(50%) are different. This serves to emphasize that the thermotransient viscosity values we have do not provide reasonable estimates for the viscosity values as required within the aforementioned upper and lower limits of the isothermal viscosity values. This is further justification for requiring the thermal hold on the samples when performing viscosity tests at the ISS, in order to generate the isothermal viscosity values which are valid estimates for the viscosity of Fe(50%)-Co(50%).

# Conclusions

## Evaporation

- Upon performing our t-test, we concluded that the evaporation coefficient  $\alpha$  has a positive linear relationship with temperature.

## Density

- For each concentration of Fe-Co at high temperatures, Fe(45%)-Co(55%) and Fe(50%)-Co(50%), we concluded that the density linearly decreases with temperature, for both of the liquid and (for the Fe(50%)-Co(50%) composition) solid regions. We could not obtain a good density-temperature relation for the solid region of the Fe(45%)-Co(55%) composition because our solid region consisted of a muddled, disordered group of points from which no coherent correlation can be drawn.
- Our density-temperature relations are correct since they depict the linear relationship similar to that of different alloys which also underwent containerless density tests.
- Further support of the accuracy and quality of the density-temperature relations we obtained lie in the small percentage differences between the predicted and experimental liquid densities at the melting temperatures, the closeness of the experimental graphical relation to the rule-of-mixtures relation for the liquid section of the Fe(45%)-Co(55%) alloy composition,

as well as the compact liquid section and more scattered solid section for the Fe(50%)-Co(50%) solid composition.

### Surface Tension

- For each of the two concentrations of liquid Fe-Co at high temperatures, we determined that the surface tension is practically constant at temperatures higher than the melting temperature. This is consistent with surface tension results obtained for other alloys (at temperatures greater than the melting temperature) which underwent similar containerless surface tension tests.
- The use of our ESL Area Processor Labview program is validated through the fact that the natural frequency of surface oscillations is constant with temperature, because of the invariability of surface tension with temperature at temperatures higher than the melting temperature.

### Viscosity

- For each of the two concentrations of liquid Fe-Co at high temperatures, we concluded that there is an Arrhenius relationship between the isothermal viscosities and the temperature, a relationship whose nature is similar to corresponding viscosity-temperature correlations for different alloys which also underwent containerless viscosity tests.

- The thermotransient viscosities for each of the two liquid Fe-Co concentrations do not fall within the upper and lower limits specified by the Arrhenius fit of the isothermal viscosities.
- An undesirable high-temperature thermal hold on the sample is necessary to run viscosity tests and generate isothermal viscosities at the ISS, since the thermotransient viscosities are not sufficient in providing proper estimates of the desired viscosity data.
- With respect to the thermotransient viscosities, the lower viscosities at higher temperatures account for a longer damping time for the sample and therefore a higher temperature range; the higher viscosities at lower temperatures occur when the sample undergoes less damping, accounting for a smaller temperature range.

#### Error Analysis

- From our t-test, we conclude that we have a linear relationship between the evaporation coefficient and the temperature.
- The low percentage difference between the predicted and experimental densities at the melting temperature for each liquid alloy composition supports the density-temperature relations that we generated.
- Based on the calculated lower and upper limits that we obtained for the isothermal viscosities, we conclude that the thermotransient viscosities do not fall within these limits; therefore a thermal hold at high temperature on

the sample is necessary to run viscosity tests to produce isothermal viscosities at the ISS.

## Future Work

There is a need to further continue the work in finding and determining the thermophysical properties of density, viscosity and surface tension with respect to temperature for the metal alloy Fe-Co. In that sense, the implication is to work with different concentrations of the alloy. The work that was completed previously involved the Fe(50%)-Co(50%) and Fe(45%)-Co(55%) alloys; similar data collection and analysis should be performed on the Fe(60%)-Co(40%) alloy, in order to obtain the material properties and to model solidification for this Fe-Co composition too. Furthermore, the work should be repeated for Fe-Co alloys with lower Co composition, such as Fe(70%)-Co(30%). The underlying purpose and task at hand is to enhance the material properties (by adjusting the solidification processes) of Fe-Co alloys with low Co composition to the grade of the properties exhibited by Fe-Co alloys with higher Co composition.

Additionally, the task of collecting the thermophysical property data on the different concentrations of the Fe-Co alloy should be replicated in microgravity conditions, as per the NASA project. The thermophysical properties of density, viscosity and surface tension which were determined on earth as a function of temperature serve as a benchmark for the same material properties which would be generated by performing similar levitation experiments in space in the future. The containerless, microgravity measurements will be conducted by NASA at the International Space Station. These material properties are under study for applications in industry and material science.

## References

- [1] R.W. Hyers, R.C. Bradshaw, J.R. Rogers, T.J. Rathz, G.W. Lee, A.K. Gangopadhyay and K.F. Kelton, "Surface Tension and Viscosity of Quasicrystal-Forming Ti-Zr-Ni Alloys", *International Journal of Thermophysics*, **25**, (2004), No. 4, pp.1155-1162.
- [2] R.C. Bradshaw, D.P. Schmidt, J.R. Rogers, K.F. Melton and R.W. Hyers, "Machine vision for high-precision volume measurement applied to levitated containerless material processing", *Review of Scientific Instruments*, **76**, (2005), 125108: 1-8.
- [3] R.C. Bradshaw, A.D. Arsenault, R.W. Hyers, J.R. Rogers, T.J. Rathz, G.W. Lee, A.K. Gangopadhyay and K.F. Kelton, "Non-linearities in the undercooled properties of  $Ti_{39.5}Zr_{39.5}Ni_{21}$ ", *Philosophical Magazine*, **86**, (2006), Nos. 3-5, pp. 341-347.
- [4] R.C. Bradshaw, M.E. Warren, J.R. Rogers, T.J. Rathz, A.K. Gangopadhyay, K.F. Kelton and R.W. Hyers, "Containerless Measurements of Thermophysical Properties of  $Zr_{54}Ti_8Cu_{20}Al_{10}Ni_8$ ", *Annal New York Academy of Sciences*, (2006), 1077: 63-74.
- [5] K. Higuchi, H.J. Fecht and R.K. Wunderlich, "Surface Tension and Viscosity of the Ni-based Superalloy CMSX-4 Measured by the Oscillating Drop Method in Parabolic Flight Experiments", *Advanced Engineering Materials*, **9**, (2007), No. 5.
- [6] M. Adachi, M. Schick, J. Brillo, I. Egry and M. Watanabe, "Surface Tension and Density Measurement of liquid Si-Cu Binary Alloys", *J Mater Sci*, (2010), 45: 2002-2008.
- [7] I. Egry, D. Herlach, M. Kolbe, L. Ratke, S. Reutzel, C. Perrin and D. Chatain, "Surface Tension, Phase Separation, and Solidification of Undercooled Cobalt-Copper Alloys", *Advanced Engineering Materials*, **5**, (2003), No. 11.
- [8] T. Hibiya and I. Egry, "Thermophysical Property Measurements of High Temperature Melts: Results from the Development and Utilization of Space", *Measurement Science and Technology*, **16**, (2005), pp.317-326.
- [9] I. Egry and J. Brillo, "Surface Tension and Density of Liquid Metallic Alloys Measured by Electromagnetic Levitation", *Journal of Chemical & Engineering Data*, **54**, (2009), No. 9, pp. 2347-2352.
- [10] Bradshaw, R.C. (2006). *Automatic Containerless Measurements of*

*Thermophysical Properties of Quasicrystal Forming Melts* (Doctoral Dissertation). University of Massachusetts Amherst, Amherst, MA.

- [11] I. Egry, G. Lohoefer and G. Jacobs, “Surface Tension of Liquid Metals: Results from Measurements on Ground and in Space”, *Physical Review Letters*, **75**, (1995), No. 22.
- [12] E. Schwartz and J. Szekely, “The Free Surface Shape and Temperature Distribution Produced in Liquid Metal Droplets by Heating Coil Pulses in the Tempus Electromagnetic Levitation Facility”, *Metallurgical and Materials Transactions B*, **29B**, (1998), pp. 1127-1134.
- [13] A.V.Grosse, “The Viscosity of Liquid Metals and an Empirical Relationship between their Activation Energy of Viscosity and their Melting Points”, *Journal of Inorganic and Nuclear Chemistry*, **23**, (1961), pp. 333-339.
- [14] M. Przyborowski, T. Hibiya, M. Eguchi and I. Egry, “Surface tension measurement of molten silicon oscillating drop method using electromagnetic levitation”, *Journal of Crystal Growth*, **151**, (1995), pp. 60-65.
- [15] I. Egry, E. Schwartz, J. Szekely, G. Jacobs, G. Lohoefer and P. Neuhaus, “Surface Tension Measurements on Liquid Metals in Microgravity”, *Metallurgical and Materials Transactions B*, **29B**, (1998), pp. 1031-1035.
- [16] T. Matsushita, H.J. Fecht, R. K. Wunderlich, I. Egry and S. Seetharaman, “Studies of the Thermophysical Properties of Commercial CMSX-4 Alloy”, *Journal of Chemical & Engineering Data*, **54**, (2009), No.9, pp. 2584-2592.
- [17] S. Watanabe, “Densities and Viscosities of Iron, Cobalt and Fe-Co Alloy in Liquid State”, *Research Institute of Mineral Dressing and Metallurgy*, **12**, (1971), pp. 17-22.
- [18] Y. Sato, K. Sugisawa, D. Aoki and T. Yamamura, “Viscosities of Fe-Ni, Fe-Co and Ni-Co binary melts”, *Measurement Science and Technology*, **16**, (2005), pp. 363-371.
- [19] G. Lohoefer, S. Schneider and I. Egry, “Thermophysical Properties of Undercooled Liquid  $Co_{80}Pd_{20}$ ”, *International Journal of Thermophysics*, **22**, (2001), No.2, pp. 593-604.



- [20] W.-K. Rhim, "Development of an electrostatic levitator and containerless processing of metals, alloys, and semiconductors", *SPIE, Materials Research in Low Gravity*, (1999), pp.1-12.
- [21] T. Ishikawa, J.T. Okada, P.-F. Paradis and Y. Watanabe, "Improvement of Viscosity Measurements Using Oscillation Drop Techniques with Electrostatic Levitators", *JAXA Research and Development Report*, (2010), pp.1-16.
- [22] I. Egry, H. Giffard and S. Schneider, "The Oscillating Drop Technique Revisited", *Measurement Science and Technology*, **16**, (2005), pp.426-431.
- [23] J. Brillo and I. Egry, "Density Determination of Liquid Copper, Nickel, and Their Alloys", *International Journal of Thermophysics*, **24**, (2003), No.4, pp.1155-1170.
- [24] J. Brillo, I. Egry, H.S. Giffard and A. Patti, "Density and Thermal Expansion of Liquid Au-Cu Alloys", *International Journal of Thermophysics*, **25**, (2004), No.6, pp.1881-1888.
- [25] Li, J. J.-Z. (2009). *Study of Liquid Metals by Electrostatic Levitation* (Doctoral Dissertation). California Institute of Technology, Pasadena, CA.
- [26] W.-K. Rhim and T. Ishikawa, "Thermophysical Properties of Molten Germanium Measured by a High-Temperature Electrostatic Levitator", *International Journal of Thermophysics*, **21**, (2000), No. 2, pp.429-443.
- [27] Y. Sato, T. Nishizuka, T. Tachikawa, M. Hoshi and T. Yamamura, "Viscosity and Density of Molten Germanium", *Institute of Advanced Materials Processing*, **32**, (2000), pp. 253-260.
- [28] K. Ohsaka, S.K. Chung and W.-K. Rhim, "Specific Volumes and Viscosities of the Ni-Zr Alloys and their Correlation with the Glass Formability of the Alloys", *Acta Metallurgica Inc.*, **46**, (1998), No. 13, pp. 4535-4542.
- [29] S. K. Chung, D. B. Thiessen and W.-K. Rhim, "A Noncontact Measurement Technique for the Density and Thermal Expansion Coefficient of Solid and Liquid Materials", *Review of Scientific Instruments*, **67**, (1996), No. 9, pp. 3175-3181.

- [30] R. E. Honig and D. A. Kramer, (1970). Appendix: Vapor Pressure Data for the Solid and Liquid Elements. In R. A. Rapp, & R. F. Bunshah, *Techniques of Metal Research, Volume IV: Physiochemical Measurements in Metal Research* (pp. 505-531). New York: Interscience Publishers.
- [31] E. Fromm, *Metall. Trans.* **9A**, (1978), pp. 1835.
- [32] Comments on Resource Data Package COL-MUSC-EML-RP-053.
- [33] D.M. Herlach, R.F. Cochrane, I. Egry, H.J. Fecht and A.L. Greer. “Containerless Processing in the study of metallic melts and their solidification”, *International Materials Reviews*, **38**, (1993), No. 6, pp. 273-347.
- [34] A. Powell, “Multicomponent Evaporation Kinetics”, (2005), pp. 1-4.
- [35] A. Powell, J. Van Den Avyle, B. Damkroger, J. Szekely and U. Pal, “Analysis of Multicomponent Evaporation in Electron Beam Melting and Refining of Titanium Alloys”, *Metallurgical and Materials Transactions B*, **28B**, (1997), pp. 1227-1239.
- [36] J. Brillo, I. Egry and T. Matsushita, “Density and Excess Volumes of Liquid Copper, Cobalt, Iron and their Binary and Ternary Alloys”, *International Journal of Materials Research*, **97**, (2006), No. 11, pp. 1526-1532.
- [37] R.-A. Eichel and I. Egry, “Surface Tension and Surface Segregation of Liquid Cobalt-Iron and Cobalt-Copper Alloys”, *Zeitschrift für Metallkunde*, **90**, (1999), No. 5, pp. 371-375.
- [38] N.M. Downie and R.W. Heath. (1974). Appendix C of *Basic Statistical Methods*. New York, USA: Harper & Row, Publishers.

## Appendices

A	Fe-Co Viscosity-Temperature Graphical Relations	101
B	Data Collection, Analysis and Reduction	105
	- Density Analysis	105
	- Viscosity and Surface Tension Analysis	109
C	Steps for Calculation of Viscosity Limits	122
D	Area-Time Plot Analysis	124
E	Temperature Profiles Showing Density & Viscosity Tests	127
	- Density Test	127
	- Isothermal Viscosity Test	128
	- Thermotransient Viscosity Test	129

## Fe-Co Viscosity-Temperature Graphical Relations

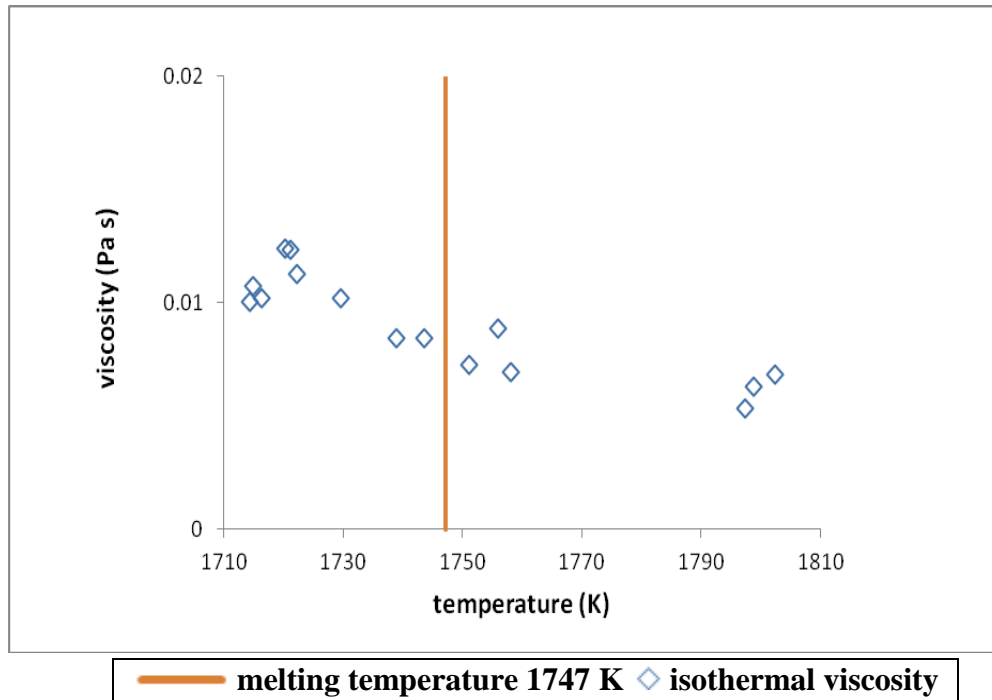


**Figure A.1:** Figure showing the graph of isothermal viscosity vs. temperature for the Fe(45%)-Co(55%) alloy.

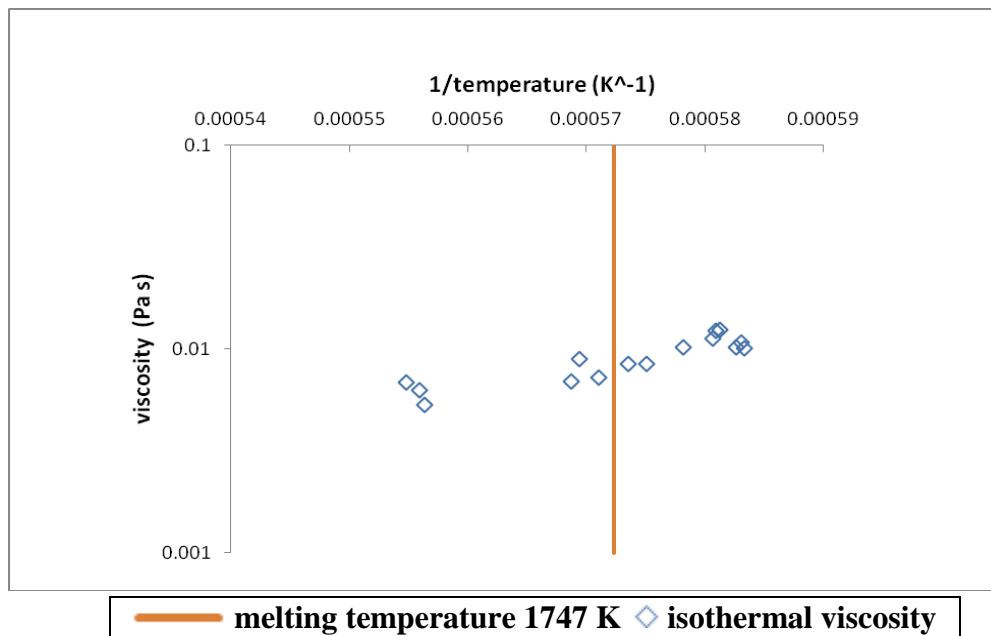


**Figure A.2:** Figure showing the graph of isothermal viscosity vs.  $1/\text{temperature}$  for the Fe(45%)-Co(55%) alloy.

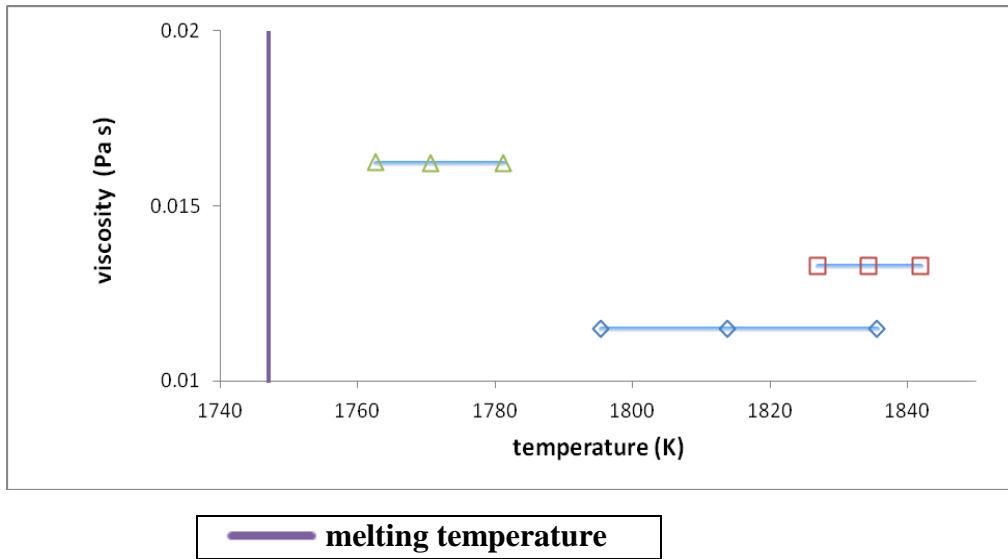


**Figure A.3: Figure showing the graph of thermotransient viscosity vs. temperature for the Fe(45%)-Co(55%) alloy.**

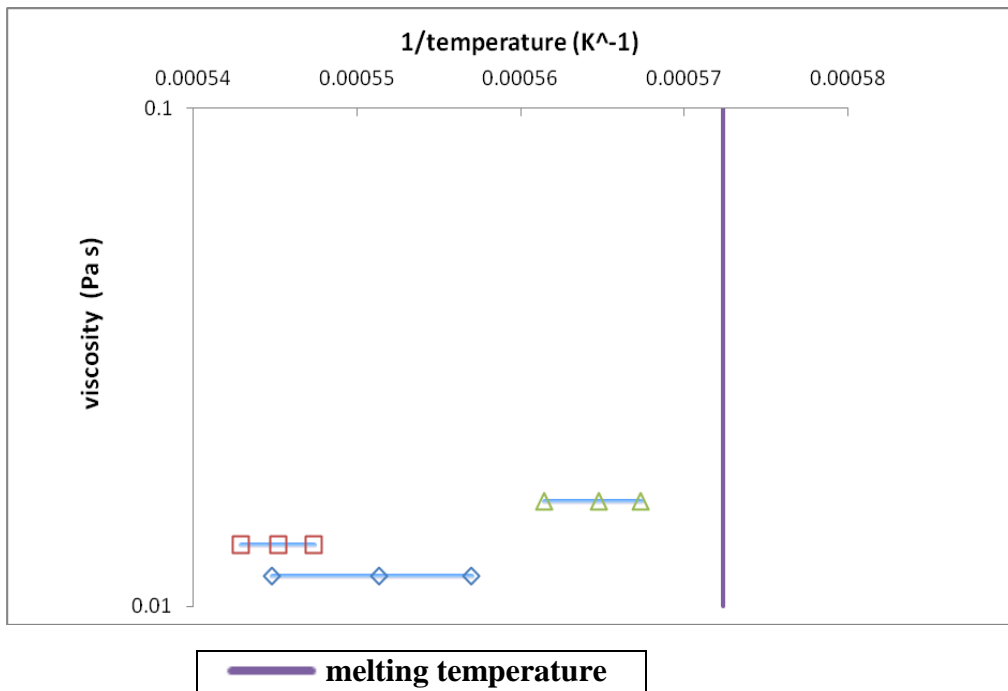


**Figure A.4: Figure showing the graph of thermotransient viscosity vs.  $1/\text{temperature}$  for the Fe(45%)-Co(55%) alloy.**

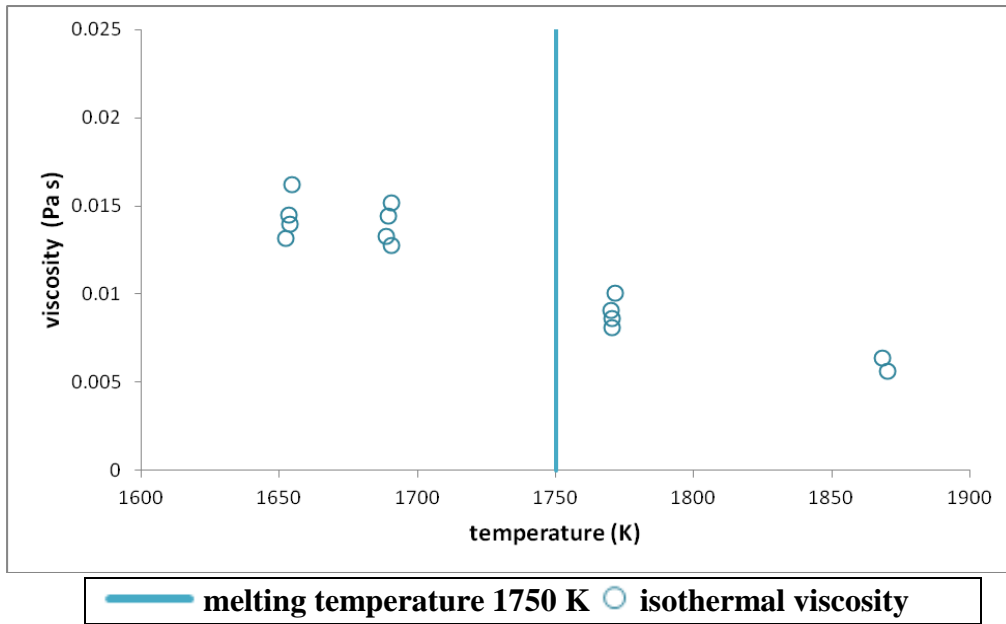


**Figure A.5:** Figure showing the graph of the isothermal viscosity vs. temperature for the Fe(50%)-Co(50%) alloy.

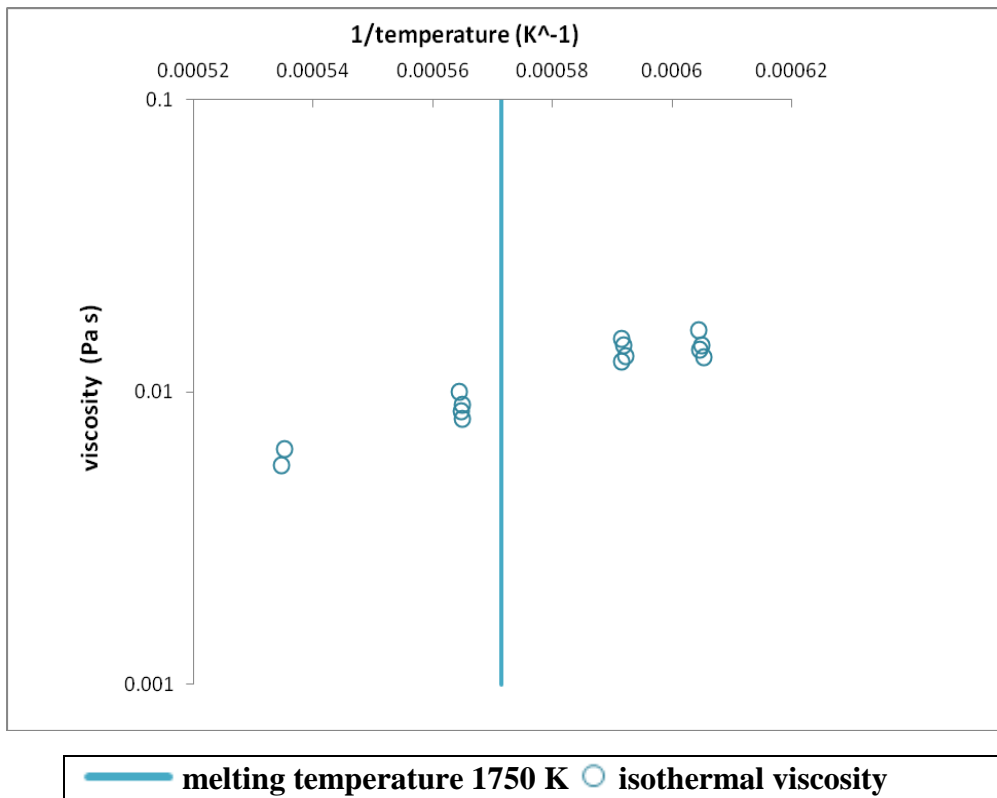
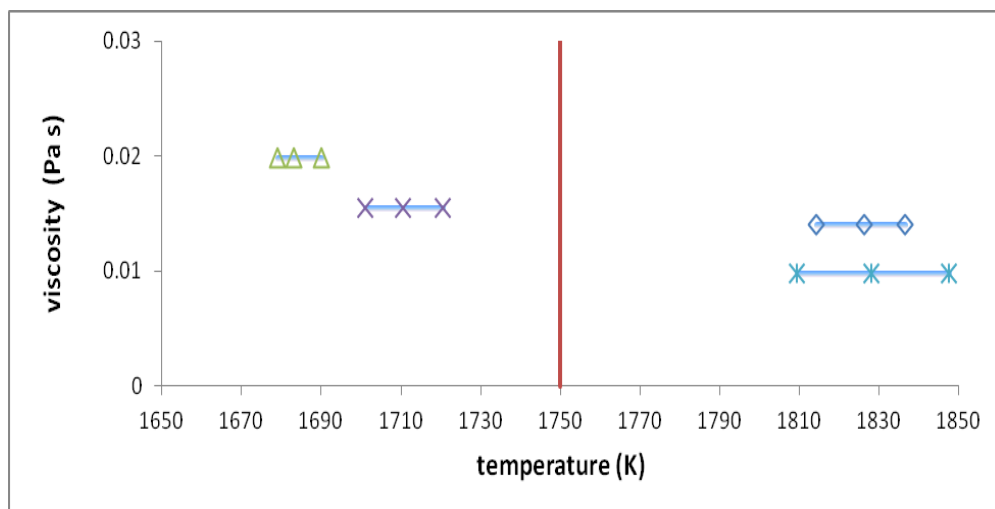
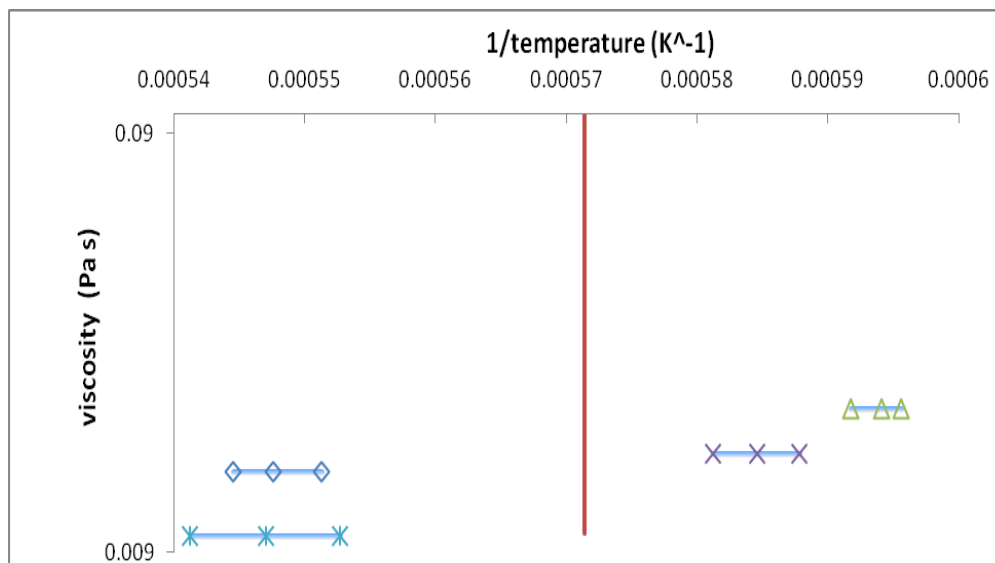


**Figure A.6:** Figure showing the graph of the isothermal viscosity vs. 1/temperature for the Fe(50%)-Co(50%) alloy.



— melting temperature 1750 K

**Figure A.7:** Figure showing the graph of the thermotransient viscosity vs. temperature for the Fe(50%)-Co(50%) alloy.



— melting temperature 1750 K

**Figure A.8:** Figure showing the graph of the thermotransient viscosity vs. 1/temperature for the Fe(50%)-Co(50%) alloy.

# Data Collection, Analysis and Reduction

## Density Analysis:

### Formatting .avi files to .vol files:

- 1 Move all the selected .avi video files to a new folder. The .avi files include density run files as well as calibration files.
- 2 Select all the files in the new folder. Right click inside the folder, select Properties and set to “Read Only”.
- 3 Include the application (.exe) file “2005-06-29\_DensityProcess\_AviToVol” in the new folder containing the .avi files.
- 4 Drag each of the .avi files to the application file and wait for the execution of the .avi file to take place by the application file. For every .avi video file, a .vol file and a .cmp file will be created and placed in the same folder as the original .avi file.

### Processing .vol files:

- 5 If there are no combined .vol files (i.e. .vol files representing several parts: part 1, part 2, part 3, etc...), then go to step 9. Otherwise, open all these ‘part’ .vol files.
- 6 Copy and Paste all the data in the .vol file parts consecutively into one single excel file. Copy the data from part 1 first, and then the data from part 2 and so on. You will end up with the “combined .vol file”.



- 7 For each part of the combined .vol file except the first, delete the first row (see below), so that the combined .vol file consists of a continuous stream of data starting from line 2.

6891	6890		275.56	2.09E+07	49	258.703	253.5	170.564	-1.32356	0.945559	1.79053	0.639472	0.250759	0.154246		
6892	6891		275.6	2.14E+07	110	248.732	256	173.019	0.410981	-2.62475	-1.2485	4.44133	0.774439	-2.85606		
6893	6892		275.64	2.19E+07	108	249.622	256.5	173.593	1.82654	-0.22785	-1.60029	-2.78302	-1.41798	0.254352		
6894	6893		275.68	2.14E+07	108	260.487	257	172.126	-1.00645	0.125109	2.24749	2.91497	-0.98009	-2.19021		
6895	6894		275.72	2.13E+07	109	273.391	256.5	171.365	-1.52391	1.41856	0.579344	0.241813	2.11475	1.73788		
6896	6895		275.76	2.13E+07	108	278.462	258	171.188	-0.97183	2.44915	-0.3156	-0.64621	2.24138	1.92234		
6897	6896		275.8	2.14E+07	110	270.896	258.5	171.484	-0.55806	1.84916	-0.79715	0.452943	2.05031	0.820822		
6898	6897		275.84	2.14E+07	109	255.985	262	171.995	-0.95201	0.825406	2.16333	2.60716	-0.93784	-1.82009		
6899	6898		275.88	2.17E+07	110	245.449	264	173.225	0.385913	-0.35234	-0.48368	-0.68194	-0.09939	0.126505		
6900	6899		275.92	2.16E+07	109	247.143	260.5	173.458	-0.94678	-2.3261	2.0124	1.56104	-0.71031	-0.32401		
6901	6900		275.96	2.16E+07	108	259.917	258	171.609	-0.51467	3.79759	-0.02014	-1.80663	0.989555	-0.27381		
6902	6901		276	2.12E+07	109	274.293	256	171.422	0.883627	1.21004	-2.65734	3.96274	1.68559	-2.26907		
6903	6902		276.04	2.13E+07	109	278.031	257	171.278	0.13461	2.3321	1.16486	-0.61029	-1.73123	1.84814		
6904	6903		276.08	2.13E+07	109	278.031	257	171.278	0.13461	2.3321	1.16486	-0.61029	-1.73123	1.84814		
6905	Frame #	Time	Delta t	Volume	I	Cx	Cy	a0	a1	a2	a3	a4	a5	a6		
6906	1		0	2.15E+07	102	251.7	256	171.902	-0.22582	1.98881	-0.81106	0.675938	1.48258	-1.34546		
6907	2		0.04	2.17E+07	109	242.741	258.5	173.314	-1.15888	-0.98964	2.14265	0.355843	-0.50657	-0.54277		
6908	3		0.08	2.16E+07	109	246.932	257	173.157	-0.92743	-0.98275	1.20317	0.099187	0.218811	-0.40238		
6909	4		0.12	2.14E+07	109	260.993	267	171.891	0.038466	1.26295	-1.00065	1.0773	1.24839	-1.54543		
6910	5		0.16	2.12E+07	110	274.383	259.5	171.45	0.027115	0.873779	1.3172	0.931071	-1.70763	0.504095		
6911	6		0.2	2.12E+07	109	275.784	258.5	171.359	0.374734	1.00098	0.668861	-0.22133	-1.54519	1.86212		
6912	7		0.24	2.11E+07	72	264.491	259	170.835	0.272392	2.14792	-0.10448	-2.45661	-0.36966	2.52932		
6913	8		0.28	2.13E+07	110	249.469	259.5	172.435	-0.75675	-1.27217	1.61789	3.38018	-0.59662	-2.14502		
6914	9		0.32	2.18E+07	110	242.25	261	174.054	-2.73523	-2.64531	3.80708	0.603163	0.429462	-1.48206		
6915	10		0.36	2.23E+07	110	248.545	255	171.947	-1.61758	7.60746	-7.02561	-7.77849	11.8573	-2.82301		
6916	11		0.4	2.05E+07	109	264.404	253.5	172.162	0.400496	-7.20534	-5.8588	17.5933	6.70681	-12.9948		
6917	12		0.44	2.12E+07	107	276.436	248.5	171.087	-1.8728	2.19174	4.04998	-8.60314	-1.69698	5.34576		

Eliminate this Row

**Figure B.1: Snapshot showing combined .vol file including data sets from all .vol file parts, from which the time and volume in pixels are accounted for.**

- 8 Find the place in Column A where the first part ends. This will be where the numbers in Column A reset back to 1. Highlight the last few cells in that part of Columns A, B and C (so that Microsoft Excel will recognize a pattern) and drag the pattern down to the end of the whole spreadsheet of the combined .vol file. Upon doing this, Column A will consist of a continuous stream of consecutive row numbers. Column C will consist of a continuous stream of consecutive time values, separated by 0.04-second time intervals.
- 9 Save the .vol file in .xls format.

Calculating and implementing the calibration factor:

- 10 Open the calibration .vol file which was generated. The original calibration .avi file was chosen based on the proximity in time of the calibration video file to that of the density video file.
- 11 Take the average value of the volume values (in pixels) in Column D and insert it in a cell on a separate excel sheet of the .vol file.
- 12 The calibration was performed using the alloy sphere W-C-Co, of diameter 2.2 mm. Its volume can be calculated as a sphere's volume:
$$\frac{\pi D^3}{6} = 5.575279763E - 3m^3$$
. Insert this value on the separate excel sheet with the average volume value in pixels.
- 13 Divide this sphere volume in  $m^3$  by the average value of the volume values in pixels to get the calibration factor in  $m^3 / pixels$  . Record the value in the spreadsheet.
- 14 Save the calibration .vol file in .xls format.
- 15 In the .vol file generated from the density video file, multiply the calibration factor obtained by the first value of the set of volume values (in pixels) in Row 2 and Column D of the .vol file. The product of multiplication should manifest in the second cell in Column O or P. Drag the multiplication pattern down to the last data row of the whole spreadsheet of the .vol file under study. The vertical stream of volume data (in  $m^3$ ) should appear in that column.
- 16 Resave the density .vol file in .xls format.

Next, we use a software program designed by engineering student John Work in order to filter the raw temperatures in the pyrofiles; the program performs the filtering through sections of the thermal profile represented by quadratic functions.

I used MATLAB to interpolate the temperature data into data on a 0.04-second basis, to be in harmony with that of the volume, which is also based on 0.04-second time intervals. The temperature data was originally based on 0.06-second intervals.

Next, a relation needs to be made between the filtered temperatures and the volumes. To do so, we observe the changes in trends in the different sections of the temperature and volume graphs, and match them. We account for any relevant information provided in the MSFC notes about the running of the cycle and what happened to the sample. For density tests which are triggered, we add the time at which the trigger was performed to the volume file times, before plotting the temperature and volume values on the same graph, versus time. We then attempt to determine a relation between the graphs. Naturally, there is a wide range of quality of testing results for samples; this is due to several reasons including oxides on the sample as well as contamination inside the levitator chamber.

Therefore, strong temperature-volume links can be derived from only a few tests.

We are mostly interested in the liquid section between the thermal peak and the recalescence, as well as the solid section which follows the second melt plateau. These sections represent the areas of study for the density-temperature relation.

Once the relation is established, we divide the proper masses at each time interval by their corresponding volumes in order to generate the densities, which in turn are plotted against absolute temperature. The masses are obtained using our flux evaporation method on the thermal cycle of the density-tested sample itself. I used MATLAB to interpolate the masses on a 0.06-second basis into data on a 0.04-second basis, to be in harmony with that of the volume, which is also based on 0.04-second time intervals. We use the masses which correspond to the temperatures pertaining to the aforementioned liquid and solid sections under examination in the thermal cycle. Hence, we obtain the density-temperature relation for the sample.

### Viscosity and Surface Tension Analysis

#### Steps:

##### **Converting .AVI file to .histofile**

- 1- Drag the .avi file to the tool 'analyzeAVI.exe' so that the video can be observed at a speed slower than the frame rate, which is 1000 frames/second. The .avi files can be observed and analyzed using this tool, as they cannot be viewed on a conventional video player because of its high frame rate. The screen shown in Figure B.2 will appear:

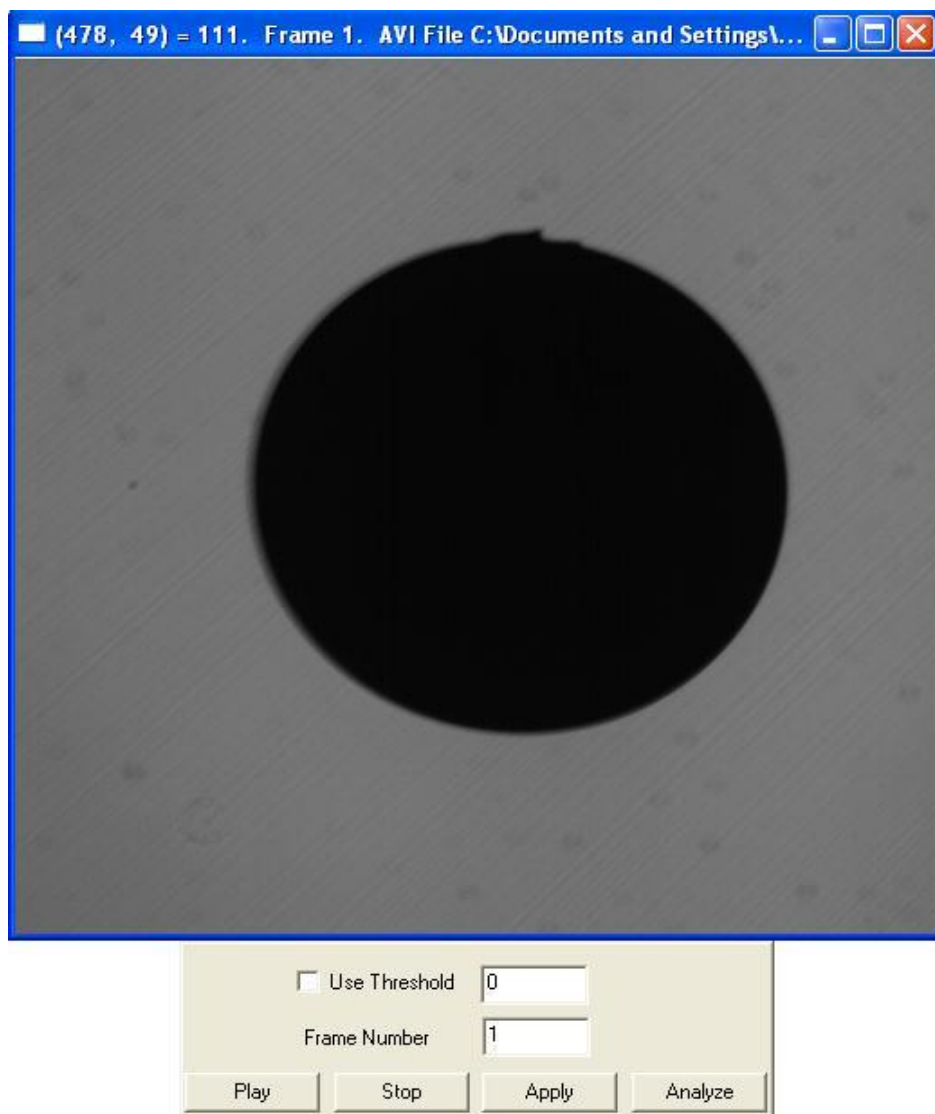


**Figure B.2: Snapshot of sample video file which appears when the sample .avi file is dragged to the tool ‘analyzeAVI.exe’; the video file can be seen at a speed slower than the frame rate.**

- 2- Click on ‘Play’ to watch the video. The deformations on the droplet can be observed due to the excitation triggered in it.
- 3- Click on ‘Analyze’ to save the file under the same name as the .avi file, only changing the .avi at the end of the file name to .histo (Figure B.3).

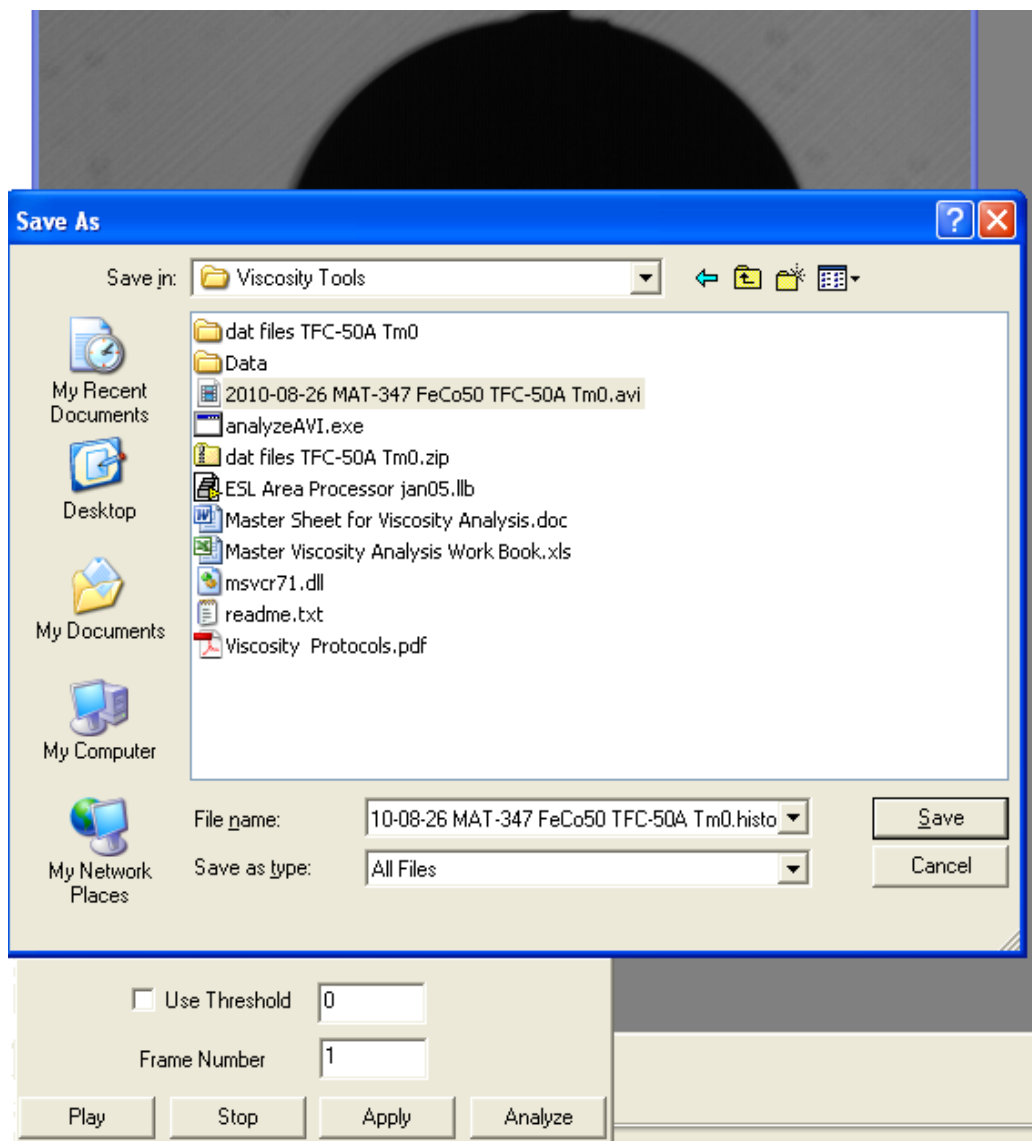


**Figure B.3: Snapshot of the sample video file which appears when ‘Analyze’ is clicked in order to save the .avi file as a .histo file.**

### **Running .histofile**

- 1- Open the file “ESL Area Processor”.
- 2- Click on ‘RUN’, the arrow on the top left-hand side of the file page.
- 3- Click on ‘Browse’ on the right-hand side of the file page. Find the .histofile saved earlier, click on it and click ‘Open’ (Figure B.4).

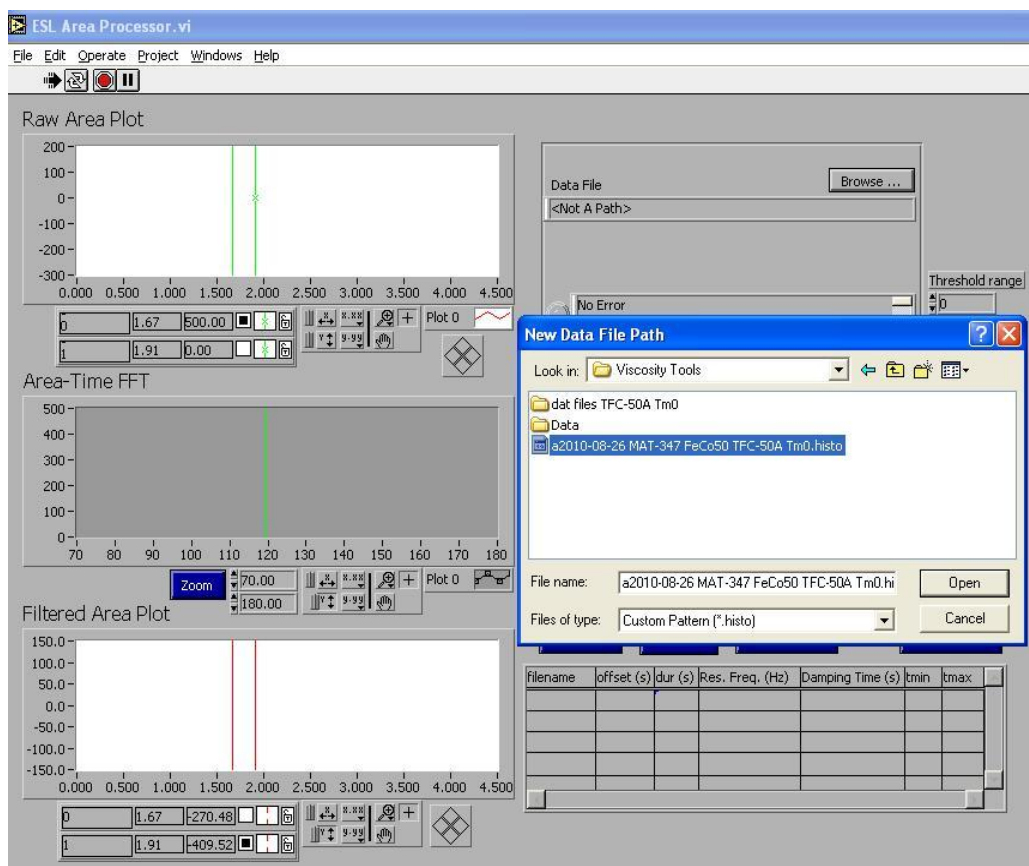


**Figure B.4: Snapshot of the ESL Area Processor when choosing the .histofile to process.**

- 4- Click on ‘Set Levels’ on the right-hand side of the file page. On the page which appears, click on ‘Read Data’. Sandwich the peak on the left so that it appears between the two yellow and green cursors, and click ‘Done’ (Figure B.5).

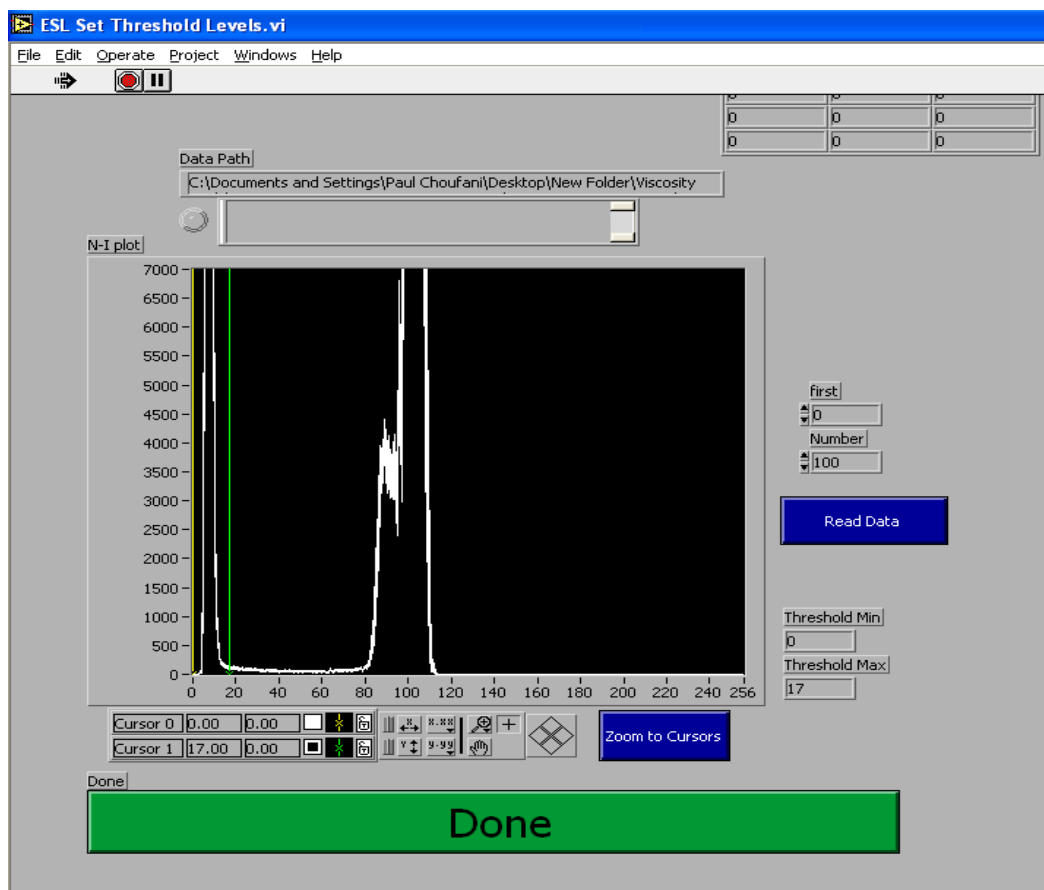


**Figure B.5:** Snapshot of the ESL Set Threshold Levels.vi plot of the number of pixels vs. pixel intensity, encapsulating the sample-representing peak on the left with the yellow and green cursors.

- 5- Back on the main processor page (ESL Area Processor.vi), click on ‘Read Data’. Click on the X-stretch and Y-stretch buttons to ensure that the subsequently-generated red damping shape of the curve stretches distinctly over the plot area of the Raw Area Plot. Place the first green cursor at the beginning of the damping process on the curve, namely where the graph starts to taper down to a horizontal line. Place the second green cursor at the end of that horizontal line. Record the ‘Time from damp to end’ as the time difference between the positions of the two cursors (Figure B.6).



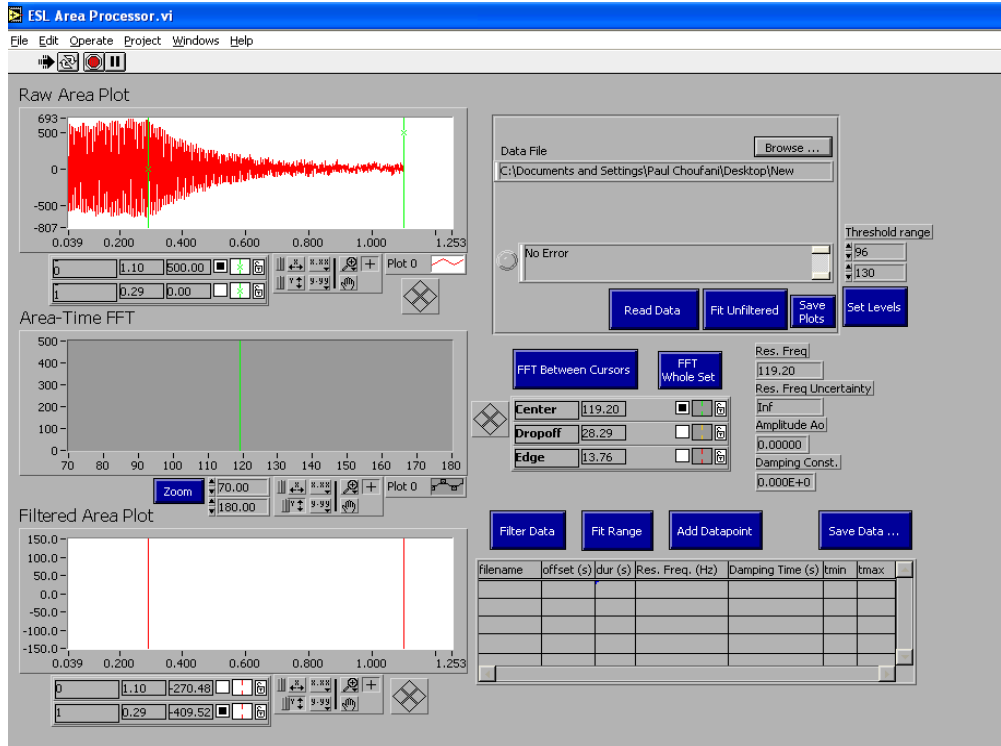


**Figure B.6: Snapshot of the ESL Area Processor.vi window showing the raw Area-Time plot and damped region encapsulated by two green cursors.**

- 6- Click twice on the ‘FFT between cursors’ button in order to generate the Area-Time FFT (Fast Fourier Transform). Place the green cursor at the peak of the curve (center), place the yellow cursors at a secondary level (dropoff) and place the red cursors where the curve becomes horizontal at the ordinate of zero (edge). Record the peak value on the Area-Time FFT curve (Figure B.7).

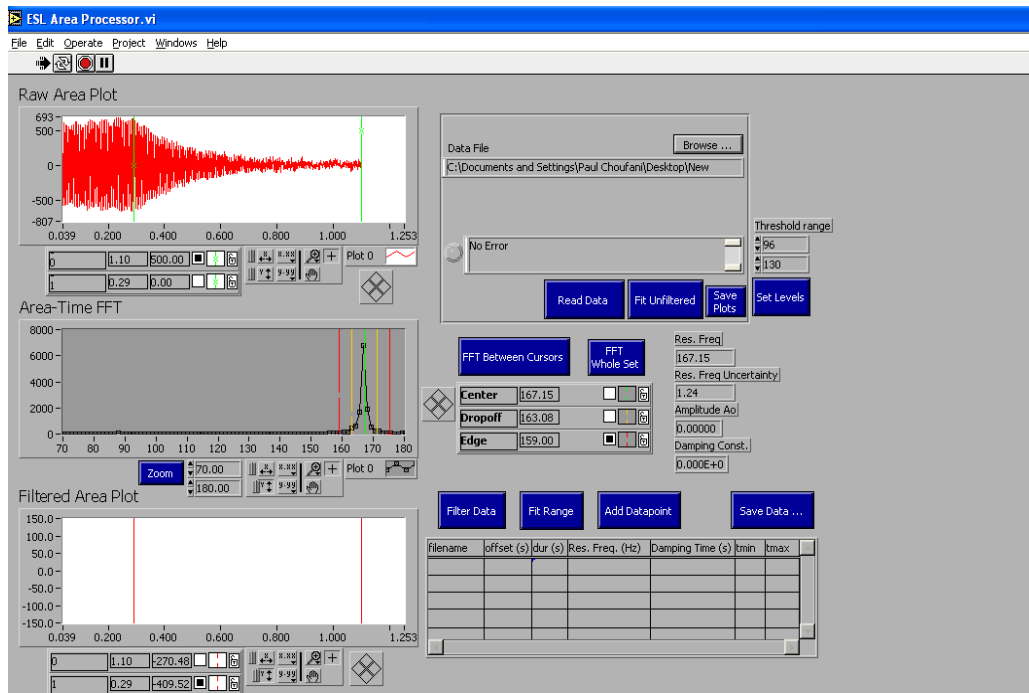


**Figure B.7: Snapshot of the ESL Area Processor.vi window displaying the generated Area-Time FFT plot (signal strength/amplitude vs. frequency), with the green cursor aligned at the curve peak, the yellow cursors at the dropoff, and the red cursors sandwiching the curve at the edge.**

- 7- Next, click on 'Filter Data' to generate the plot of the filtered area-time signal, in green. Measure the amplitude of the Filtered Area Plot (height of curve just before damping takes place) and record it (Figure B.8).

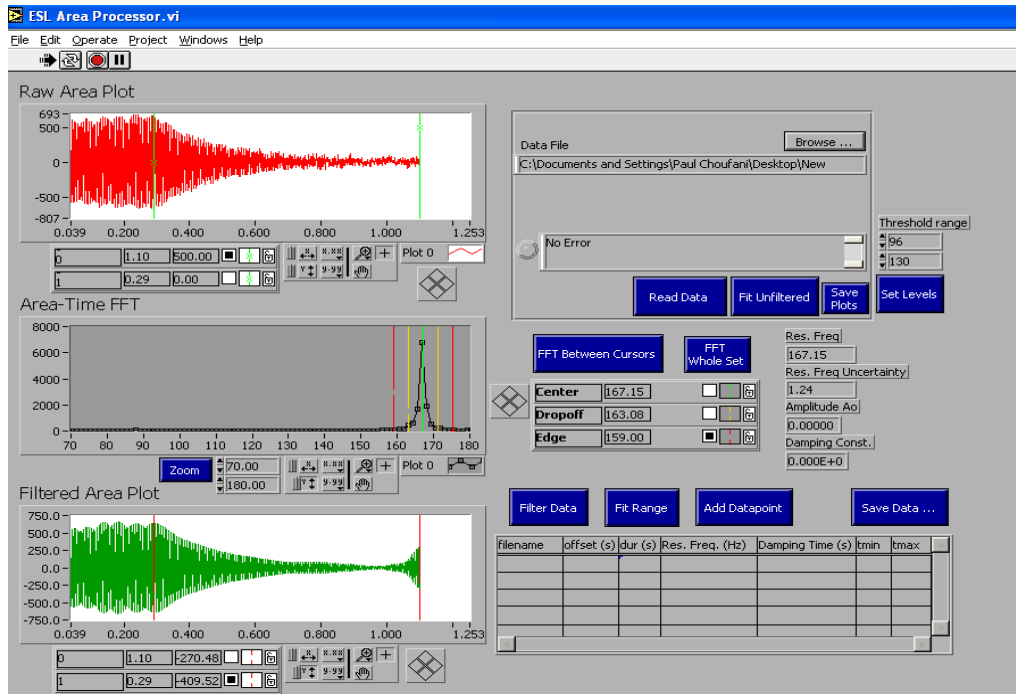


**Figure B.8: Snapshot of the ESL Area Processor.vi window displaying the filtered Area-Time plot and damped region encapsulated by two red cursors.**

## Fitting

- 1- Click on 'Fit Range' on the main processor page to generate the fitting page (Figure B.9).
  - 2- Initially, verify to make sure that the fitting curve (in white) is aligned with the damping signal which was filtered earlier (in blue), specifically in the decisive region where the damping shape ends, namely reaching a horizontal orientation. If not, click on 'reset cursors' to ensure the signal region under study is the one subjected to the fitting parameters.
- For the fitting process, the signal region is subjected to the fitting oscillation curve (white curvy line). The fitting parameters are the frequency of oscillation (controlled by blue cursor), the shape of the curve

(altered by the two green perpendicular cursors), the curve's amplitude represented by the two boundaries of the fitted cycle (purple boundaries) and the current cycle location where the fitting procedure starts (shown by yellow cursor which can be moved) (Figures B.9, B.11).

- 3- Click on Auto damping and Amplitude on the fitting page, and then click on Levenburg-Marquardt Fit (Figure B.10). Make sure the fit is good in quality, as shown in the next two Area-Time plots below.
- 4- Record the damping time constant, click on Auto  $t_0$  and then click on Leven-Marquardt Fit. Record the damping time constant again and repeat the process for a total of six or seven damping time constants, recording each of them.

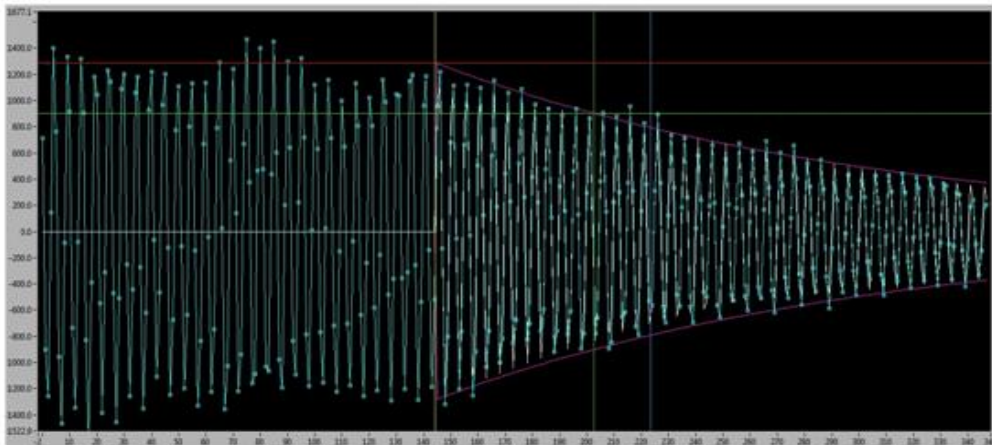


**Figure B.9: Snapshot of the entire filtered Area-Time plot in the window which appears upon clicking 'Fit Range' in the ESL Area Processor.vi window, displaying the damped region undergoing the fitting process.**

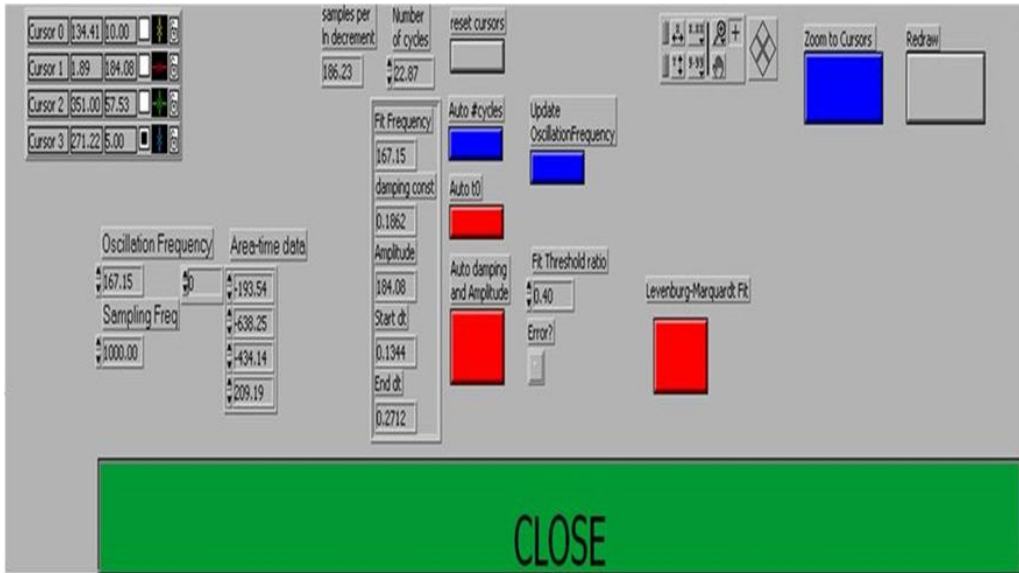


**Figure B.10:** Snapshot of the section containing the controls and operations in the window which appears upon clicking ‘Fit Range’ in the ESL Area Processor.vi window; these controls are the tools used for fitting the damped region of the filtered Area-Time plot.

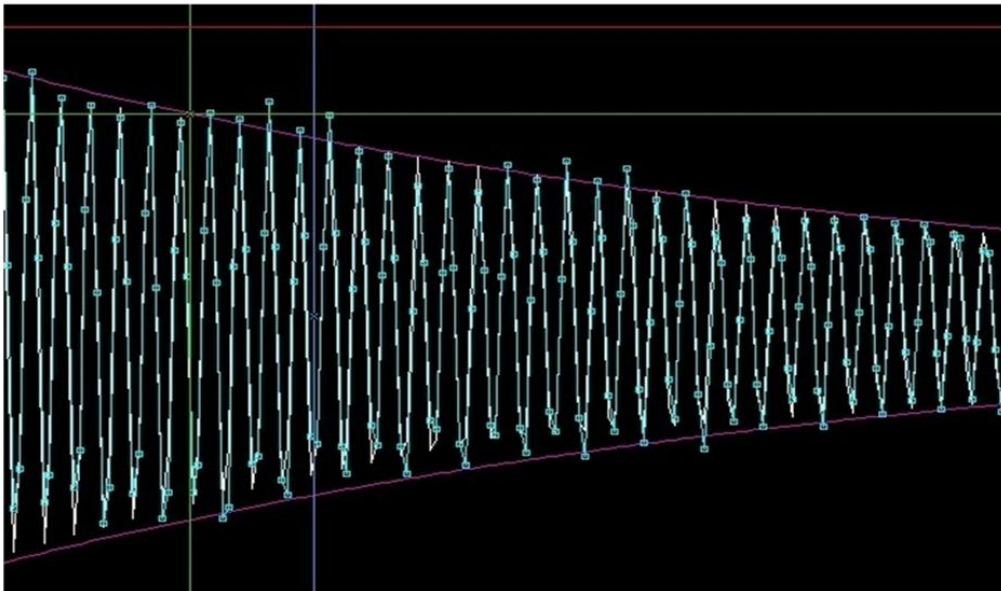


**Figure B.11:** Snapshot of a zoomed-in view of the filtered Area-Time plot in the window which appears upon clicking ‘Fit Range’ in the ESL Area Processor.vi window, displaying the damped region undergoing the fitting process.

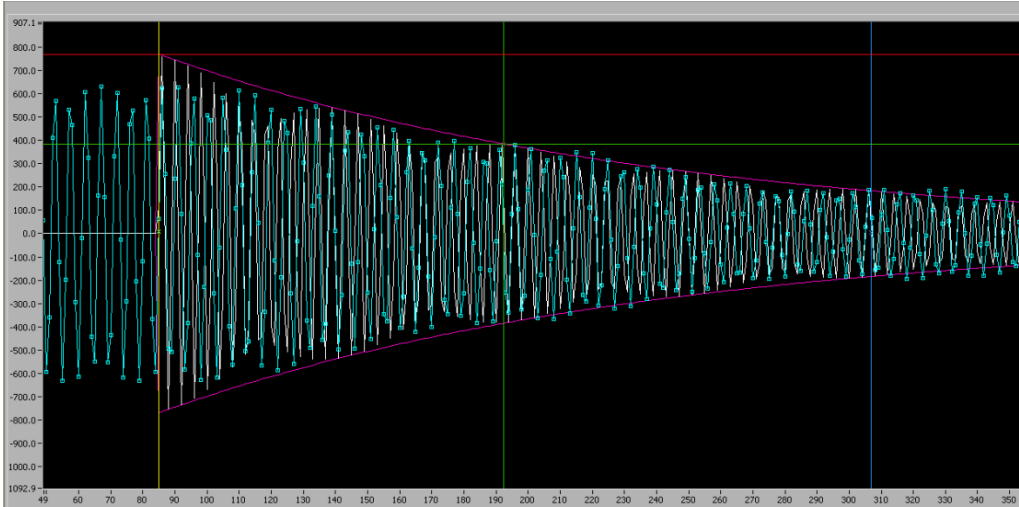


**Figure B.12: Snapshot of a poor attempt at a fit of the damped region of the filtered Area-Time plot, which is to be unaccounted for while choosing the datapoint.**

Choosing the datapoint:

- 1- Choose the damping time constant from the constants recorded earlier.  
The value chosen should represent the optimal damping value which a good representative of the critical damping region studied.
- 2- Click on ‘reset cursors’ to go to the critical signal region where the damping occurs (same region studied before). Click again on ‘Auto Damping and Amplitude’ on the fitting page, and then click on ‘Levenburg-Marquardt Fit’.
- 3- If the green ‘Close’ bar turns red after undergoing the L-M fit, then increase the value of the Fit Threshold ratio and try again until the ‘Close’ bar turns green.
- 4- If the damping time constant value shown does not match the optimal damping time constant chosen (or at least if it is not close to it in

- value), then click on 'Auto t0' and then 'Levenburg-Marquardt Fit' until the optimal damping time constant is displayed in its corresponding box in the controls and operations section.
- 5- When the optimal damping time constant is reached, Click on 'Update Oscillation Frequency' and record the oscillation frequency, as well as the damping time constant.
  - 6- Record the Fit Threshold Ratio.
  - 7- Comment on the quality of the filtered curve and the fitting process for the curve, based on how smooth the damping curve looks as well as your confidence in performing the fitting, generating the damping constants, and choosing the optimal damping time constant for the critical signal region of the curve.
  - 8- Click on 'Close'.
  - 9- Back on the main processor page, click on 'Add Datapoint', and then click on 'Save Data'.
  - 10- Save the data using the same file name as the .avi and .histo files, instead using .dat instead of .avi or .histo at the end of the file name.  
  
The file saved is of .dat format, and can be opened as a text document.
  - 11- Right-click on the table under 'Filter Data', 'Fit Range', 'Add Datapoint', and 'Save Data'; click on 'Empty Table'.
  - 12- Process another .histofile as explained above, or click on the red circle at the top of the main processor page to stop the running of the ESL Area Processor LabView program.

13- In the .dat file saved for each sample cycle, we account for the frequency (Hz) and damping time constant (s) in determining the surface tension (N/m) and the viscosity (Pa s), respectively.

- We end up with the viscosities and surface tensions for all cycles of all tested samples (for each Fe-Co composition ratio); we then plot the viscosities and surface tensions against the absolute temperature, on separate graphs.
- The mass used to calculate the isothermal viscosity is the average mass over the time period of the pulse (deformation) triggered in the sample during the viscosity test.
- With respect to the thermotransient viscosity calculation, we have a temperature range matching the time period for the damping as a result of the pulse triggered in the sample. Therefore, we use the average mass over the damping time period for the average temperature of the range. Additionally, as we have a mass range over the temperature range in question, we use the mass corresponding to the minimum temperature and the mass corresponding to the maximum temperature to calculate the corresponding thermotransient viscosities – the viscosities at both ends of the temperature range in the time period of the damping following the triggered pulse.



## Steps for Calculation of Viscosity Limits

For each concentration, we plot the upper and lower limits of the isothermal viscosities (shown in Figures 45 and 46), in order to determine whether the thermotransient viscosities are in the numerical vicinity of the isothermal viscosities, with the purpose of determining whether isothermal viscosity tests need to be executed at the ISS through the application of a thermal hold on the given sample. The upper and lower limits, which account for the range of error for the isothermal viscosities, were calculated as follows, with 95% confidence:

- 1- Perform an exponential fit on the isothermal viscosity values.
- 2- Calculate the exponential fit values at the given isothermal viscosity temperatures.
- 3- Subtract the exponential fit values from the isothermal viscosity values.
- 4- Divide the differences by the corresponding exponential fit values.
- 5- Add 1 to each of those differences.
- 6- Find the average and standard deviation of the generated values from step 5.

- 7- Add twice the standard deviation to the average to generate the upper coefficient; subtract twice the standard deviation from the average to generate the lower coefficient.
- 8- To generate the upper limit values, multiply the exponential fit values by the upper coefficient; to generate the lower limit values, multiply the exponential fit values by the lower coefficient.
- 9- Perform an exponential fit on each of the upper limit values and lower limit values; therefore, the upper limit and lower limit curves can be generated.

## Area-Time Plot Analysis

The 'Area-Time' plots shown above (Figures B. 9 and B.11) are actually representations of the deviation of the sample area itself (due to the sample's oscillations over time) from the sample's original area at equilibrium. The oscillations consist of vertical and horizontal deviations of the sample.

If we zoom into the filtered 'Area-Time' plot, we see that it is a series of peaks and troughs:

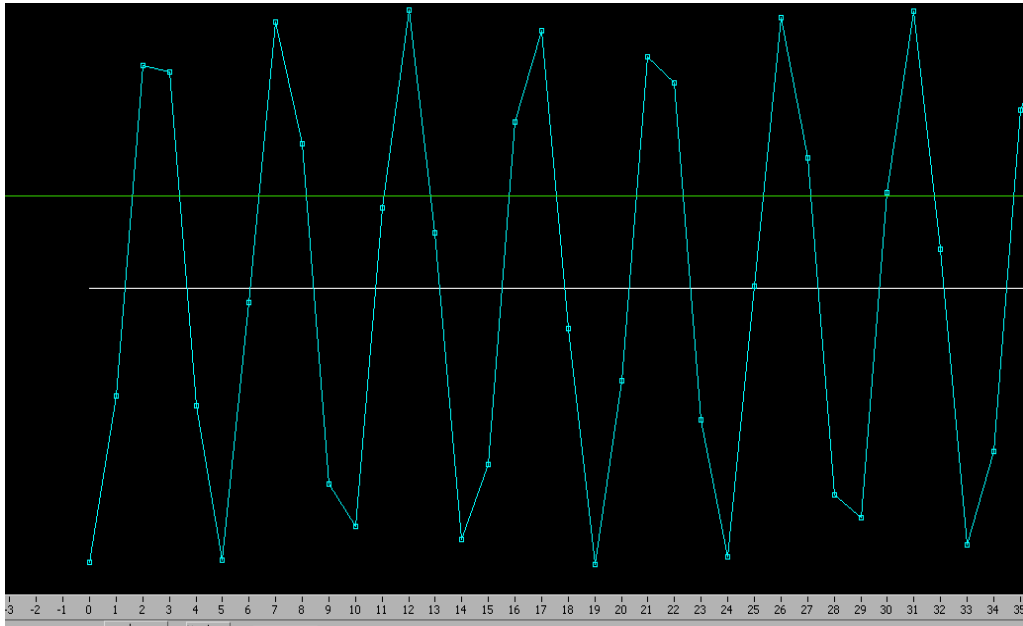


**Figure D.1: Snapshot of a highly zoomed-in view of the filtered Area-Time plot, showing a series of peaks and troughs.**

As we see in the above plot, Frame Number 5 represents a trough and Frame Number 31 represents a peak.

The trough occurs when the sample deviates in a vertical direction, as exemplified by Frame Number 5, shown in Figure D.2:

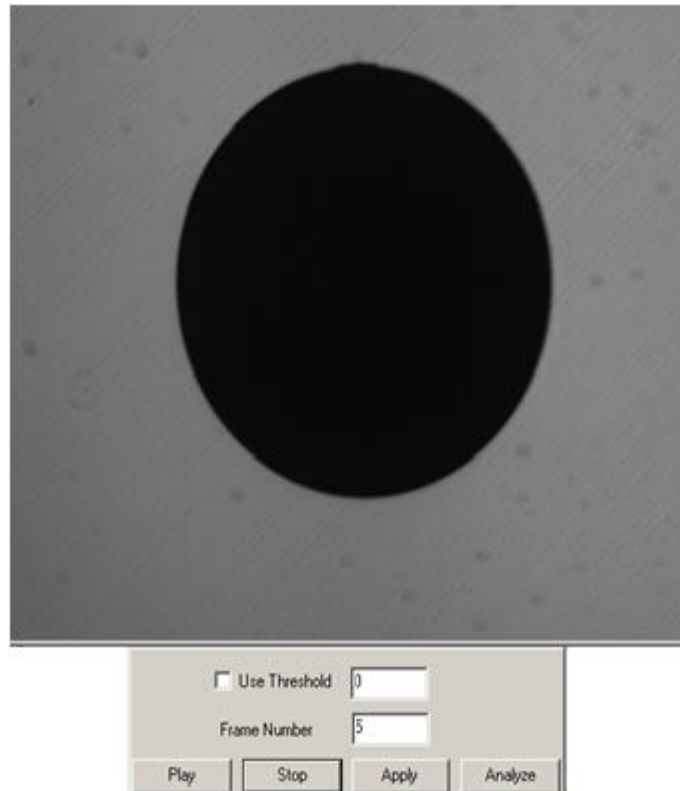


**Figure D.2: Snapshot of the sample deviating vertically, at Frame Number 5.**

The peak occurs when the sample deviates in a horizontal direction, as exemplified by Frame Number 31, shown in Figure D.3:

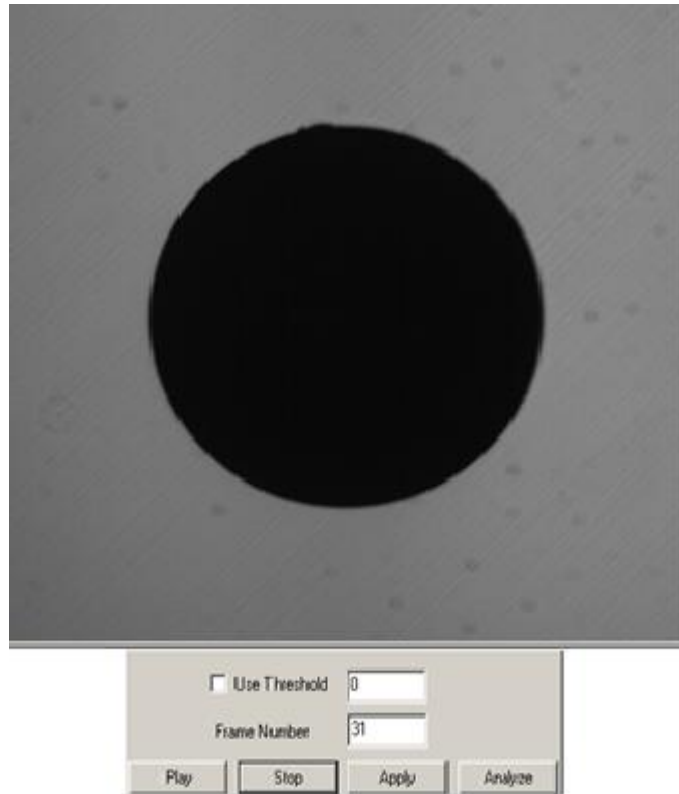


**Figure D.3: Snapshot of the sample deviating horizontally, at Frame Number 31.**

Therefore, the area deviation vs. time plot consisting of the peaks and troughs in succession reflects the horizontal and vertical deviations of the sample as it oscillates.

## Thermal Profiles Showing Density & Viscosity Tests

### Density Test:

Figure E.1 displays the thermal profile showing the density tests being performed on the sample while it cools in its liquid state (from the superheated peak to the minimum undercooled temperature) and in its solid state.

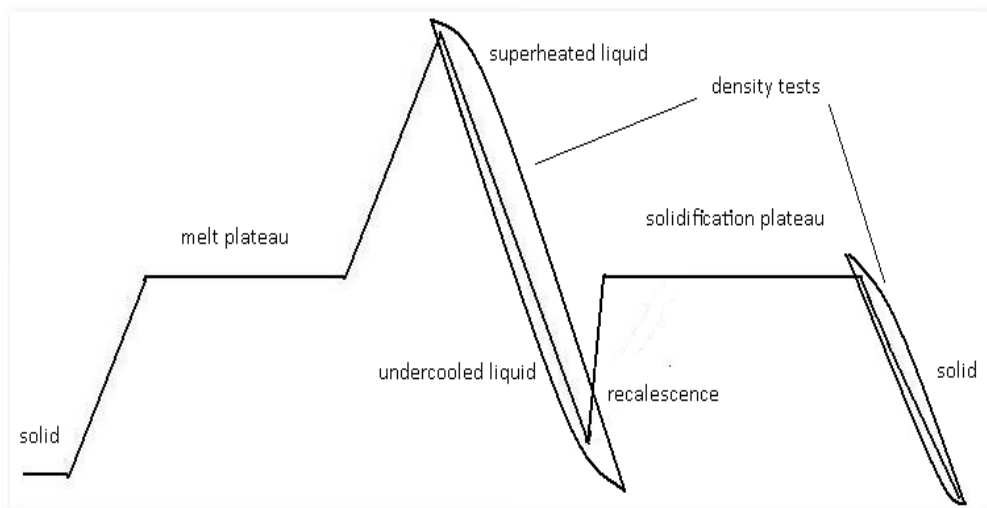


**Figure E.1: Diagram showing the positions on the thermal profile of the density tests on the cooling sample in the liquid and solid states.**

### Isothermal Viscosity Test:

Figure E.2 displays the thermal profile showing the isothermal viscosity tests being performed on the liquid sample at the melting temperature, after it cools from the superheated peak. The tests are represented by the deformations shown on the thermal profile. The laser power setting is selected to define the experiment (sample) temperature, which is constant when the laser power is turned on at that laser setting.

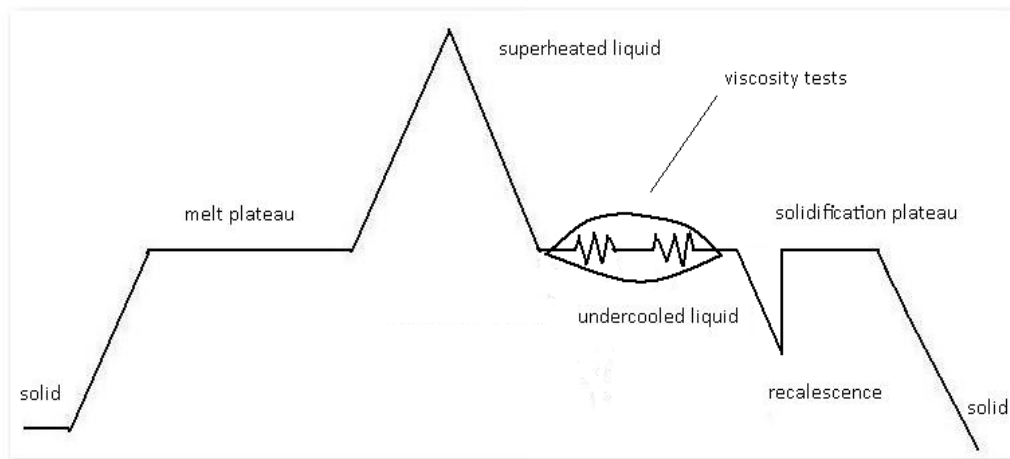


**Figure E.2: Diagram showing the positions on the thermal profile of the isothermal viscosity tests on the liquid sample at the melting temperature.**

### Thermotransient Viscosity Test:

Figure E.3 displays the thermal profile showing the thermotransient viscosity test being performed on the liquid sample as it cools continuously from the superheated peak to the minimum undercooled temperature. The test is represented by the deformation shown on the thermal profile. There is no laser power during the testing. The time period of activation of the triggered pulse in the sample determines the temperature range when the viscosity test occurs.

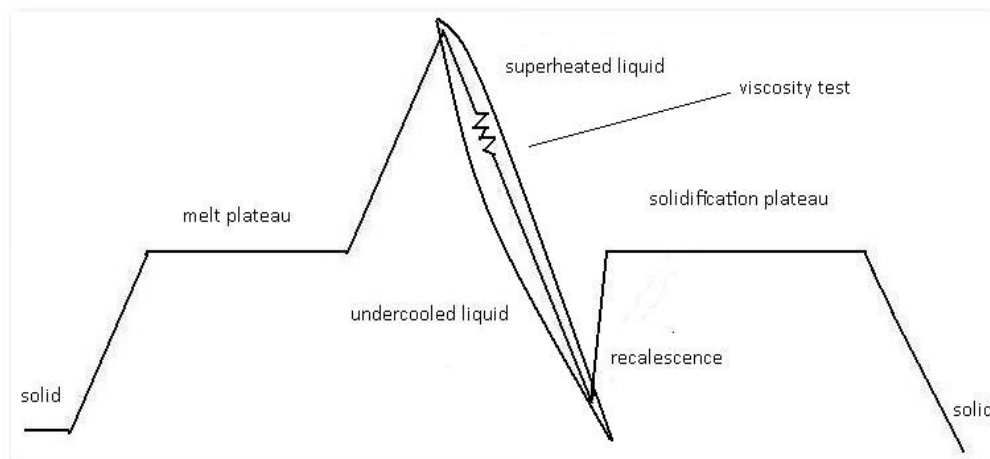


**Figure E.3: Diagram showing the position on the thermal profile of the thermotransient viscosity test on the cooling sample in the liquid state.**